Kinetic Model Development for the Combustion of Particulate Matter from Conventional and Soy Methyl Ester Diesel Fuels

by

Andrea Strzelec

A dissertation submitted in partial fulfillment of

the requirements for the degree of

Doctor of Philosophy

(Combustion Engineering)

At the

University of Wisconsin – Madison

2009

Acknowledgements

First and foremost, I would like to express my sincere and deep gratitude to my dissertation advisors, Professor David Foster, Dr. Stuart Daw, Professor Christopher Rutland and Dr. Todd Toops for their guidance and support for this work. I am very grateful to have been given this opportunity and look forward to continuing to work with them throughout my career. I also want to express my appreciation to Professors James Dumesic, Fleming Crim, James Schauer and Randy Vander Wal for their time in serving on my committee.

I am grateful to the Department of Energy Office of Vehicle Technology for supporting this work, and I want to explicitly thank my sponsors Gurpreet Singh and Kevin Stork. I am indebted to Dr. Johney Green and Dr. Stuart Daw for giving me the opportunity to do my dissertation research at Oak Ridge National Laboratory; it has been a wonderful experience.

They say that it “takes a village” and for my development as a researcher that has certainly been true. Many, many thanks to my ORNL village: Dr. Robert Wagner and Scott Sluder for their assistance with the engine work, Dr. John Storey and Sam Lewis for the help with the GCMS analysis, Dr. Hassina Bilheux for facilitating the neutron imaging work and especially Dr. Todd Toops for letting me dirty his lab with diesel particulate and assisting me with the kinetic analysis as well as teaching me how to properly tell my story in a presentation. I probably owe Dr. Charles Finney an entire page of his own for his selfless willingness to work evenings, weekends and holidays to help me collect the data presented in this dissertation. I would also like to thank the many staff members and postgraduate fellows of the Fuels, Engines and Emissions

Research Center who have made this a pleasant and productive place to work, specifically my fellow Wisconsinite friends Josh Pihl and Dr. Tom Briggs and his wonderful wife Anita, who kindly edited my roughest writing. I would be remiss if I did not also thank Jan Draine, Norberto Domingo and Donna Doolittle for their assistance in my time at ORNL.

Most importantly, I want to express my appreciation to my family. I am indebted to my sister Susan, who started me on this path by introducing me to the UW-ERC, and who has supported me throughout the duration – thanks for the care packages, they helped more than you know. It is extremely important to note that none of this would have been possible without the love, support and encouragement of my parents, Mike and Rosemary. Mom and Dad, thank you for teaching me the importance of hard work and dedication - I would not have been successful without you.

Abstract

The primary objective of this research has been to investigate how the oxidation characteristics of diesel particulate matter (PM) are affected by blending soy-based biodiesel fuel with conventional ultra low sulfur diesel (ULSD) fuel. PM produced in a light duty engine from different biodiesel-conventional fuel blends was subjected to a range of physical and chemical measurements in order to better understand the mechanisms by which fuel-related changes to oxidation reactivity are brought about. These observations were then incorporated into a kinetic model to predict PM oxidation.

Nanostructure of the fixed carbon was investigated by HR-TEM and showed that particulates from biodiesel had a more open structure than particulates generated from conventional diesel fuel, which was confirmed by BET surface area measurements. Surface area evolution with extent of oxidation reaction was measured for PM from ULSD and biodiesel. Biodiesel particulate has a significantly larger surface area for the first 40% of conversion, at which point the samples become quite similar.

Oxidation characteristics of nascent PM and the fixed carbon portion were measured by temperature programmed oxidation (TPO) and it was noted that increased biodiesel blending lowered the light-off temperature as well as the temperature where the peak rate of oxidation occurred. A shift in the oxidation profiles of all fuels was seen when the mobile carbon fraction was removed, leaving only the fixed carbon, however the trend in temperature advantage of the biofuel blending remained. The mobile carbon fraction was measured by temperature programmed desorption found to generally increase with increasing biodiesel blend level. The relative change in the light-off

temperatures for the nascent and fixed carbon samples was found to be related to the fraction of mobile carbon. Effective Arrhenius parameters for fixed carbon oxidation were directly measured with isothermal, differential oxidation experiments.

Normalizing the reaction rate to the total carbon surface area available for reaction allowed for the definition of a single reaction rate with constant activation energy (112.5 ± 5.8 kJ/mol) for the oxidation of PM, independent of its fuel source.

A kinetic model incorporating the surface area dependence of fixed carbon oxidation rate and the impact of the mobile carbon fraction was constructed and validated against experimental data.

Table of Contents

1 Introduction 1

1.1 Motivation 1

1.2 Research Objective and Approach 5

2 Literature Review 7

2.1 Diesel Particulate Filters 7

2.2 Diesel Particulate Formation and Structure 8

2.3 Particulates from Biodiesel Fuels 11

2.4 Detailed Diesel Particulate Characterization 14

2.4.1 Nanostructure 14

2.4.2 Organic Speciation 16

2.5 Carbon Oxidation Kinetics 17

2.6 Summary 26

3 Experimental Setup 27

3.1 Engine and Exhaust System Setup 27

3.2 Fuels 32

3.3 Nanostructure Characterization Methods 33

3.4 Chemical Speciation Methods 35

3.5 Microreactor Experiments 37

3.5.1 Microreactor Sample Preparation 38

3.5.2 BET Surface Area Measurements 39

3.5.3 Oxygen Chemisorption & Active Surface Area Measurement 40

3.5.4 Temperature Programmed Desorption 41

3.5.5 Temperature Programmed Oxidation 42
3.5.6 Isothermal Determination of Kinetic Parameters 42
3.6 Summary 44
4 Results and Observations 45
4.1 Particulate Formation Experiments 46
4.2 Evaluation of Particulate Reactivity Differences 51
4.2.1 Temperature Programmed Oxidation 51
4.2.2 Temperature Programmed Desorption 55
4.2.3 Determination of Elemental Carbon Reaction Kinetics 62
4.2.4 BET Surface Area 68
4.2.5 Surface Area Normalizes Reaction Rates 72
4.2.6 Investigation of the EC Nanostructure 76
4.3 Chemical Speciation 83
4.3.1 Parent Fuels 83
4.4 Discussion 88
5 Model Development & Validation 89
5.1 Previously Existing Kinetic Models for Particulate Oxidation 89
5.2 Modeling of Oxidation Experiments 90
5.2.1 Oxidation Reaction Rate 90
5.2.2 Fixed Carbon Oxidation 91
5.2.3 Volatile Carbon Pyrolysis Reaction Rate 93
5.2.4 Mass Balance and Energy Balances 93
5.2.5 Validation 95
5.2.6 Sensitivity Analysis 102

5.3 Summary 105

6 Summary and Recommendations 107

6.1 Summary 107

6.2 Recommendations for Future Work 109

7 References 110

8 Appendices 119

8.1 Appendix 1: Acronyms & Glossary 119

8.2 Appendix 2: Additional Experiments 121

8.2.1 A2.1 Stepped Temperature Programmed Desorption 121

8.2.2 A2.2 X-ray Photoacoustic Spectroscopy (XPS) 122

8.2.3 A2.3 Nanostructure of biodiesel blends 123

8.2.4 A2.4 Speciation of SOF with Particulate Collection Location 125

8.2.5 The Effect of Inorganics 131

8.2.6 DPF Degradation 134

8.3 Appendix 3: Neutron Imaging of Diesel Particulate Filters 138

8.3.1 3.1 Introduction 138

8.3.2 Basic Principles of Neutron Imaging 139

8.3.3 Experimental Setup & Facility 142

8.3.4 Neutron Computed Tomography 143

8.3.5 Experimental Results 145

8.3.6 Image Processing and Quantification of Soot Deposits 149

8.3.7 Conclusions 155

8.4 Appendix 4: Sample Model Calculations and Parameter Values 156

1 Introduction

1.1 Motivation

The internal combustion engine, quite literally, drives the economy of the developed world. Ever-increasing global energy demands and limited petroleum supplies have focused international attention on improving engine efficiency and developing alternative fuel sources. This has naturally brought the diesel engine to the forefront of propulsion research.

Compression ignition (CI), diesel engines have traditionally been used in the transportation industry and for off road applications due to their superior thermal efficiency and durability as compared to their gasoline counterparts. Recently, diesels are experiencing growth in the passenger vehicle market due to their 20-30% energy efficiency advantage [1] over gasoline spark ignition (SI) engines. Higher efficiency correlates directly with reduced CO_2 and hydrocarbon (HC) emissions, as compared to gasoline engines. However, due to the nature of the heterogeneous diesel combustion and presence of excess O_2, the exhaust contains higher levels of nitrogen oxides (NO_x) and particulate matter (PM), or soot. The term soot has been used colloquially in the literature for diesel particulates; however, soot, as defined by Webster's Dictionary, is "a black substance formed by combustion, rising in fine particles and adhering to the sides of a chimney." Therefore the more accurate terminology for diesel particulates will be used here.

Environmental concerns are resulting in increasingly strict regulation of engine particulate emissions in the United States, Japan and Europe. At least currently, control of particulates from diesel engines is generally more challenging than for gasoline engines because diesels tend to emit larger quantities of particulates in the regulated size range. Diesel particulate filters (DPFs) are currently the dominant diesel particulate emissions control technology, and they function by mechanically removing particulates from engine exhaust. As DPF technology has advanced, it has become increasingly clear that a better understanding of the nature of diesel particulates in diesel exhaust is critical for optimizing the performance of DPFs, especially in the context of a rapidly changing fuel supply.

Diesel particulates are produced as micron and submicron scale aerosols during the combustion process from unburned fuel and lubricating oil residues. They are typically comprised of an elemental carbon (EC) substrate onto which partially combusted hydrocarbons are adsorbed. The amount of adsorbed hydrocarbons relative to elemental carbon is typically indicated in terms of soluble organic fraction (SOF), organic carbon fraction (OC) or volatile organic carbon (VOC), depending on how it is measured. The relative amounts of elemental C and hydrocarbons as well as the composition of the hydrocarbons are functions of the fuel, oil, the engine type, and the engine operation [2].

The most prevalent DPF design is the wall-flow monolith depicted in Figure 1. This design is derived from the traditional Three Way Catalyst (TWC) flow-through monolith. By plugging alternate channels, the filter is transformed from flow-through to

wall-flow, and the exhaust flow that enters through open channels, encounters the plugs on the back end and is forced to exit through the porous walls of the ceramic substrate. This strategy leads to high filtration efficiency and a high surface area to volume ratio, making it well suited to regulating diesel particle emissions. Collection efficiencies greater than 90% have been reported in the literature [3, 4].

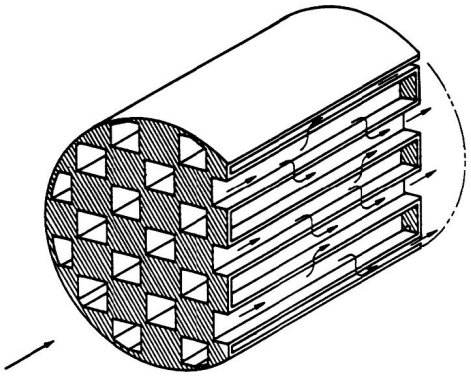

Figure 1 Illustration [5] of a wall flow ceramic diesel particulate filter.

While particulate capture is typically very efficient in current DPFs; periodic removal of the collected particulate material is required in order to prevent serious efficiency losses due to pressure drop. The continuous collection of particulate causes increasing backpressure, which adversely effects engine operation and fuel efficiency. This condition can be resolved by operating the DPF at conditions where the trapped particulates can be oxidized to carbon dioxide by oxygen in the exhaust. The process of initiating combustion of trapped exhaust particulates is referred to as regeneration. Regeneration can be accomplished either passively (where particulate

oxidation occurs spontaneously under normal operating conditions) or actively (where exhaust conditions such as temperature or oxygen level are deliberately adjusted away from their normal state). Whichever regeneration approach is used, the inclusion of catalysts in the filter substrate can enhance particulate oxidation rate.

Because DPF pressure drop and regeneration both result in fuel penalties, DPF management becomes an integral part of managing vehicle fuel economy. Thus this study is motivated by the need to better understand DPF particulate oxidation in order to achieve maximum fuel utilization in diesel vehicles.

Political and environmental pressures have increased the urgency for the development of petroleum alternative fuels. Renewable biofuels are of particular interest, as their level of CO_2 impact on the environment is less than that of petroleum diesel. Neat biodiesel (B100) can be produced from vegetable oils, including corn, coconut, palm and soybean oils. Soy based biodiesel is currently the most common. One method for converting these oils to fuel type molecules is base catalyzed transesterification with an alcohol, typically methanol. This process can occur at low temperature and has a greater than 98% conversion efficiency. Soy biodiesel is composed of three methyl-esters, a C16 and two C18 isomers when produced in this fashion. Another method for the conversion of vegetable oils to fuel type molecule is by hydrotreating, a process more similar to petroleum cracking, that creates a more diesel-like hydrocarbon envelope.

Although it is well known that biodiesel combustion results in a reduction in particulate and increase in NO_x emissions and the soluble organic fraction [6], its effect

on particulate properties and aftertreatment devices is only lately being studied. The impact of particulates derived from biodiesel and biodiesel blends and the oxygenated fuel components on particulate structure and reactivity is of particular interest.

1.2 Research Objective and Approach

The primary objective of this research has been to investigate how the oxidation characteristics of diesel particulates are affected by blending soy-based biodiesel fuel with conventional diesel fuel. In addition to directly measuring oxidation characteristics, the DPF particulate produced by different biodiesel-conventional fuel blends was subjected to a range of physical and chemical measurements in order to better understand the mechanisms by which fuel-related changes to oxidation reactivity are brought about. These additional characterizations included: the relative fixed and mobile carbon (FC and MC) fractions; the chemical composition of the mobile fraction; the particulate surface area; and major structural and chemical features revealed by electron microscopy. In order to be sure that the results were relevant to realistic diesel particulate emissions, the experimental particulate in this study was generated with a modern light duty diesel engine using well-characterized fuels. The integrated nature of the particulate generation, sampling, and characterization processes are summarized in Figure 2.

The following chapters provide a more detailed explanation of the rationale behind the approach employed here, a summary of the experimental observations, and an in-depth analysis of how this study's results can lead to improved models for diesel particulate oxidation. A review of previous literature on diesel particulates and previous

work on carbon particle oxidation is provided in Chapter 2. More detailed descriptions of the experimental methods used are provided in Chapter 3. Chapter 4 focuses on a detailed discussion of the experimental results and their implications. The kinetic model development and validation of the model are detailed in Chapter 5. Chapter 6 summarizes the conclusions and outlines recommendations for future work. There are also several appendices included which detail the results of additional experiments that, while interesting, are not directly relevant to the understanding of the oxidation characteristics, which is the focus of this work.

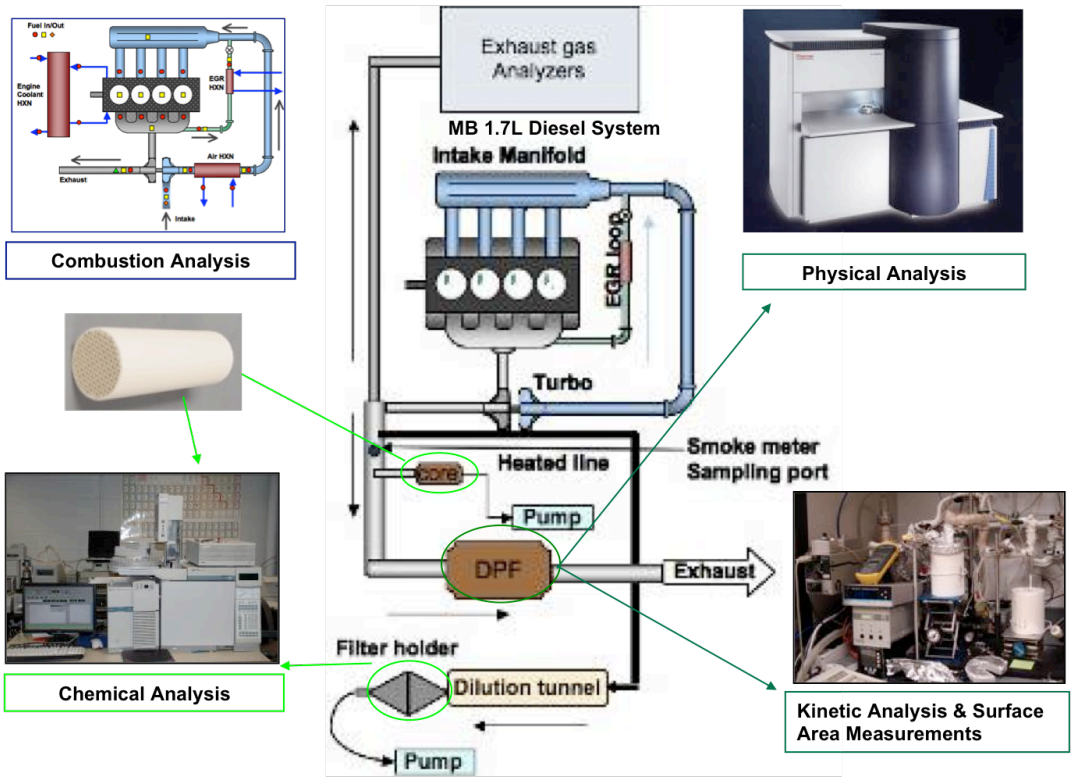

Figure 2 Overview of samples and analyses.

2 Literature Review

2.1 Diesel Particulate Filters

As discussed in the Introduction, diesel particulate filters (DPFs) reduce tailpipe particulate emissions by mechanically filtering the diesel exhaust. The most prevalent DPF design is the wall-flow monolith, which is derived from the flow-through ceramic monoliths used for other types of catalytic exhaust aftertreatment. DPF monoliths are unique in that alternate channels are plugged at opposite ends so that exhaust gases enter in one channel, pass through a porous wall, and then exit through a parallel channel. As a result particulates are trapped in and on the wall, creating partially clogged wall pores and a surface a particulate cake. This strategy leads to high filtration efficiency and a high surface area to volume ratio, making it well suited to regulating diesel particle emissions.

Managing the trap particulate inventory is the greatest DPF control issue. As the inventory increases, backpressure on the engine also increases, which can adversely affect engine operation and fuel efficiency. In order to maintain acceptable engine operating conditions, the trap must be 'regenerated' by oxidizing the stored particulate.

Regeneration can be accomplished by low temperature passive oxidation or active, catalyst-augmented oxidation and/or high temperatures (>600K). Ideally, under lean conditions, particulates are passively oxidized by NO_2 and excess oxygen in the exhaust gas [7] at typical exhaust temperatures, reducing the frequency of active regeneration events. When active regeneration is required, it is extremely important to

be able to predict the rate of particulate oxidation in order to prevent excessive temperatures that can physically damage the DPF ceramic. It is also important to be able to accurately predict the level of preheating required to minimize excess fuel consumption. Both regeneration methods require implementation of some sort of model to guide the DPF control strategy.

DPF modeling efforts [8, 9] have focused on describing the filtration, gas flow, temperature distribution, and pressure drop during particulate accumulation and regeneration. Sub-models for particulate oxidation often assume simple, first-order heterogeneous reactions, with empirical parameters [9]. The high degree of variability in particulate oxidation behavior from one engine to the next and between different drive cycles makes it clear that an improved understanding of the fundamental processes involved in particulate oxidation is needed to meet the current needs for DPF modeling and controls. This is especially challenging now with the increasing market presence of biofuels. Thus research into the impact of biofuels on particulate filtration and oxidation properties is essential in optimizing DPF technology.

2.2 Diesel Particulate Formation and Structure

To understand oxidation of diesel particulates, it is important to understand their initial formation and physical structure. The backbone of diesel particulates is elemental carbon, which is initially released from the fuel by a complex series of reactions during combustion. After their initial release, individual carbon atoms link together in large numbers to form large aggregates and agglomerates that make up the basic particulate

superstructure [10]. In diesel engines, this process occurs at the locally rich regions of the fuel spray [11], as shown in Figure 3.

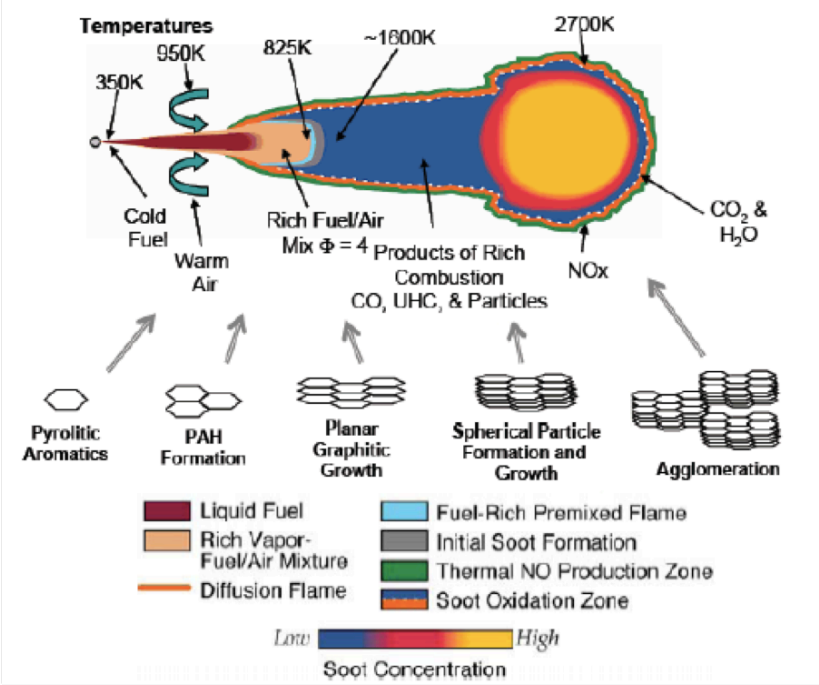

Figure 3 Dec conceptual model of particulate formation [11].

Work by Harris [10, 12] suggests that particulate formation occurs via three distinct stages: particle inception or nucleation, particle growth, and chain formation. Particle nucleation occurs by the homogeneous reaction of the gas phase hydrocarbons into spherical, condensed nanoparticles [13]. The rate of particle nucleation is very fast, though it occurs over only a few milliseconds. The fraction of the total exhaust particulate concentration that is contributed by this process is very low, but these nuclei have large surface area. After the nuclei are formed, the transition from inception to

growth is gradual; the nuclei particles continue to develop by surface growth as a result of chemisorption and coalescence. First, the small particles coalesce into larger spheres, thus reducing the number of individual particles. Then hydrocarbon gas phase species chemically bond to the surface of the particle and become integrated into the solid phase. This process, also referred to as surface growth, is responsible for the mass increase in the primary particulates.

The final stage of growth, chain formation, occurs when nuclei agglomerate to form three-dimensional structures [14]. Agglomerates are held together by polyaromatic hydrocarbons (PAHs) that condense from exhaust and act as coagulating agents. Many studies have examined the impact of fuel type on particulate formation [14-16], but these have specifically not included practical alternative diesel fuels such as bio, oil shale or oil sands derived fuels. Structural changes are closely related to burning mode, and particle growth is heavily reliant on the hydrocarbon species in the gas phase. These structural changes may be important in modeling particulate oxidation [17].

Particle collisions and coagulation (aggregation) are responsible for the distribution of particle sizes seen [18]. Additionally, from the moment the particulates leave the combustion chamber, the exhaust gas temperature is decreasing. As the exhaust cools, the saturation pressures of exhaust hydrocarbons, particularly residual fuel hydrocarbons, products of partial oxidation, and lube oil components, are reduced and these compounds begin to condense on the surface of the particles. These components make up the soluble organic fraction (SOF) of the particulate.

2.3 Particulates from Biodiesel Fuels

Neat biodiesel (B100) can be produced from vegetable oils, including corn, coconut, palm and soybean oils. Soy-based biodiesel is currently the most common. One method for converting these oils to fuel type molecules is base catalyzed transesterification with an alcohol, typically methanol. This process can occur at low temperature and has a greater than 98% conversion efficiency. Soy methyl ester (SME) biodiesel is composed of three methyl esters, a C16 and two C18 isomers, skeletal structures of which are shown in Figure 4, when produced in this fashion. This makes for a very different fuel profile than conventional diesel fuel, as shown in Figure 5.

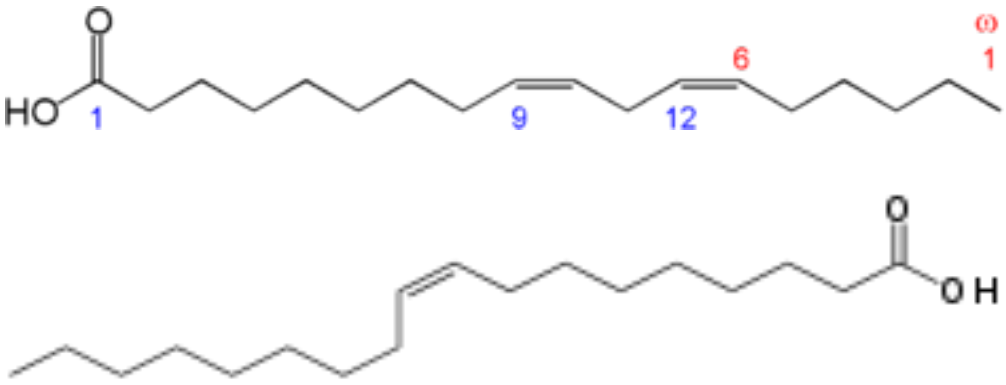

Figure 4 SME Biodiesel is typically comprised of an oleic acid (C16, top) methyl ester and two isomers of the linoleic acid (C18, bottom) methylester.

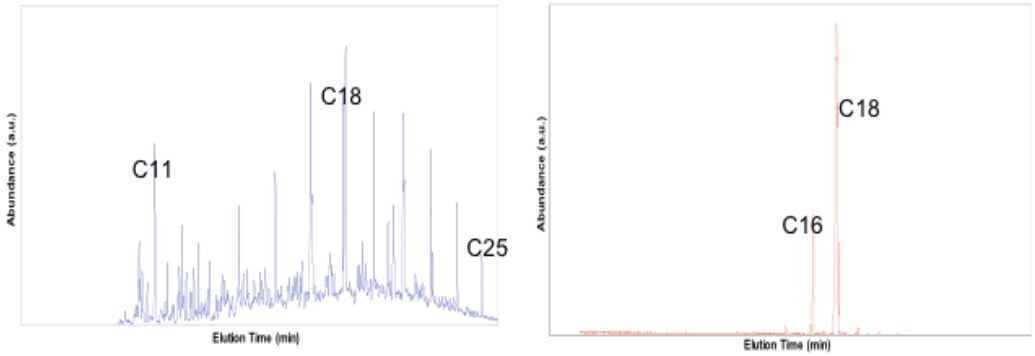

Figure 5 GCMS Profiles of ULSD (left) and SME B100 (right) Fuels.

Another method for the conversion of vegetable oils to fuel type molecule is by hydrotreating, a process similar to petroleum cracking, that creates a more diesel-like hydrocarbon envelope. Fuel produced by this method is referred to as 'renewable' diesel rather than biodiesel.

Although it is well known that biodiesel combustion results in a reduction in particulate concentration and increase in NO_x emissions and the soluble organic fraction [19], its effect on particulate properties and aftertreatment devices is only lately being studied. The impact of particulate derived from biodiesel and biodiesel blends and their oxygenated fuel components on particulate structure and reactivity is of particular interest.

A recent comparison of the impact of oxygen-enriched fuels on diesel emissions [20] confirmed the reduction in the concentration of particles in the exhaust stream when the fuel was supplemented with biodiesel with only a modest increase in NO_x. Investigation of the effect of biodiesel blends on the regeneration of particulate filters

showed that biodiesel blending increased the SOF content of the particulates, which made available additional reactive hydrocarbons to be oxidized in the DPF. Biodiesel fuel was also shown to impact the carbon structure of the particulate, producing more amorphous carbon. Inclusion of biodiesel in the fuel reduced the temperature necessary to induce regeneration in the DPF, hypothesized as being due to the increased amount of SOF, increased production of NO and the changes in the observed nanostructure.

Another in-depth study of the effect of biofuels blends on particulate properties and DPF regeneration [19] showed additional evidence that fuel oxygen content has an influence on particle reactivity on a global scale in a DPF. It was noted that the oxidation rate was enhanced and a unique oxidation ‘process’ was hypothesized specifically for biodiesel particulate, where the particulate particles were thought to follow a center-out burning mode. Observing such a hollowed out structure, the authors proposed that nanostructure alone does not dictate the reactivity of the particulate. In fact, the capsule-type oxidation of particulates that was observed suggests that the initial surface species have greater influence than the structure or pore size distribution of the particles due to greater oxygen functionality from the biodiesel. The authors recommend further study of particle pore size and the role of porosity in oxidation to better understand the fundamental behavior and support for more rigorous models. They also advocated study of the effect of oxygenated fuel on aromatic content and, in turn, its impact on particle reactivity.

2.4 Detailed Diesel Particulate Characterization

2.4.1 Nanostructure

Diesel particulates have a large range of structures associated with them, from the nanostructure associated with the graphene layers forming the primary particles, seen in Figure 6, to the fractal aggregate, composed of agglomerated primary particles [21, 22] as seen in Figure 7. The nanostructure has long been understood to impact particulate's physical properties and chemical reactivity, including the reactive surface area and oxidation characteristics [21-24]. Thermal pyrolysis work by Vander Wal and Tomasek [25] has shown by High Resolution Transmission Electron Microscopy (HR-TEM) that the temperature, pressure, and the rate of temperature rise during formation greatly impact the nanostructure of particulate. At lower temperatures, the particulate structure is more amorphous in nature, consisting of short, randomly oriented, disconnected segments. With increasing temperature, the graphene segments grow in length and are more ordered, or graphitic, in nature.

Vander Wal and collaborators from Cummins Engine Company have also seen significant differences in the structure, size, and behavior of particles from different engine load-speed points [26]. Braun [27, 28] examined particulate properties for diesel engine-derived particulate and observed that changes in the nanostructure between idle and load conditions were much greater for oxygenates than conventional diesel.

The oxidative reactivity of a particulate has been shown to be dependent on the initial nanostructure; specifically, the more ordered graphitic structure exhibits higher threshold temperatures and is more resistant to oxidation than amorphous carbon [29].

Diesel particulates are typically made up of multiple carbon types, as seen in Figure 6. This may be the result of several factors, including different effective densities, as well as different particle size distributions.

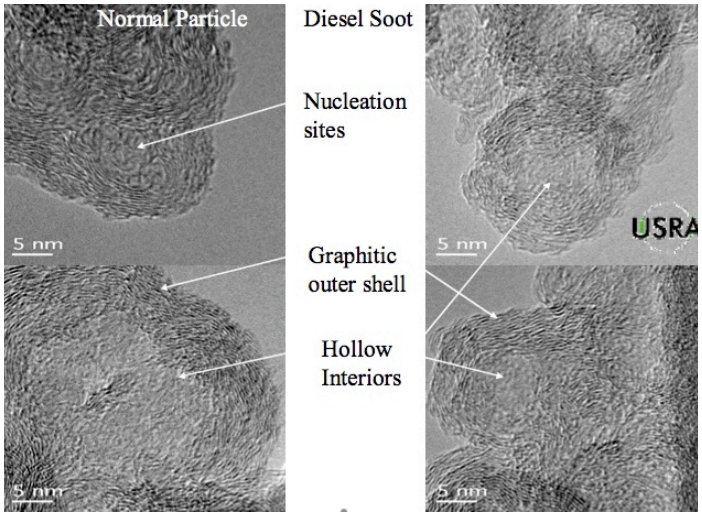

Figure 6 Diesel particulate primary particle structural images [26].

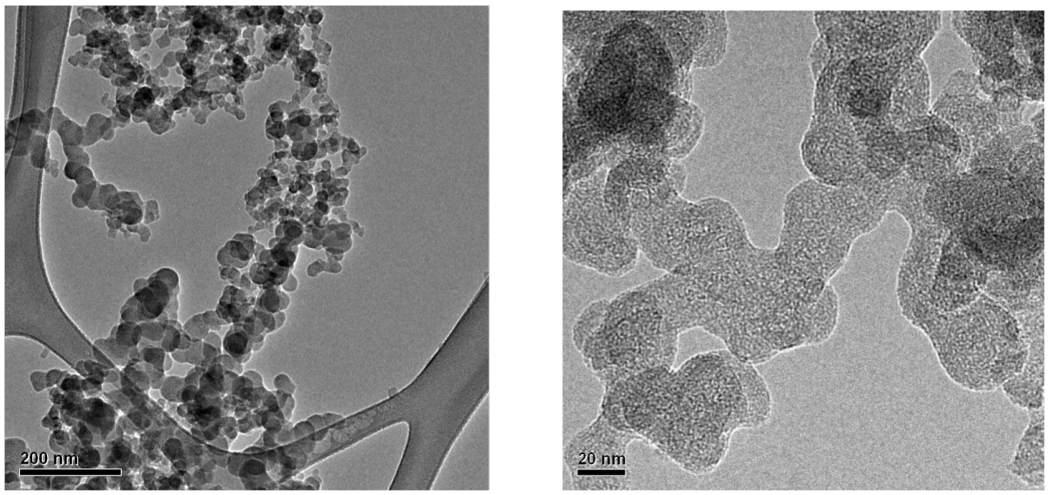

Figure 7 Diesel particulate aggregates.

In the Active Site Mechanism theory [30], particulate oxidation is said to proceed through dissociation of edge site carbons, and therefore samples with more edge sites, physical defects in the structure, and less tangential arrangement are known to be more reactive, as there are geometrical and electrical availability advantages [31-33].

The ability to alter particulate nanostructure properties by changing fuel or operating conditions has been clearly demonstrated by previous work; however, many of the studies employed synthesis conditions that were not equivalent to diesel combustion or did not isolate the impact of the fuel from the combustion conditions.

2.4.2 Organic Speciation

Attached to the fixed carbon (FC) backbone of diesel particulates are mobile carbons (MC), adsorbed hydrocarbon products of incomplete combustion, widely referred to as the soluble organic fraction (SOF), shown schematically in Figure 8.

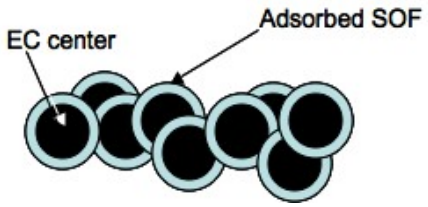

Figure 8 Diesel Particulate Schematic

The chemical characteristics of MC have been studied for conventional and advanced combustion diesel engines [2, 34-37]. Low temperature combustion (MK, HCCI, HECC) regimes typically have higher organic (MC) content than conventional

diesel combustion [35]. For conventional combustion, it was shown that higher load points have less mobile content than at lower loads, likely due to the exhaust gas temperature [38]. These studies have been conducted primarily with conventional diesel. However, an ORNL study [37] found that adding 5 vol% biodiesel increased the level of hydrocarbons in the exhaust.

So far, there is little information in the literature related to the impact of biodiesel fuel and biodiesel blends on the speciation and partitioning (gas phase versus solid phase) of the unburned hydrocarbons in exhaust particulate. Since the presence of volatiles is known to influence the reactivity of carbon in other contexts, such as coal [39], it is plausible to expect that the mobile species adsorbed to the particulate may impact the particulate surface structure and perhaps the oxidative reactivity of the particulate. If this is the case, correlations of specific exhaust species and their oxidative impact are likely to be useful for modeling DPF particulate oxidation kinetics.

2.5 Carbon Oxidation Kinetics

The carbon-oxygen reaction has important roles in many industrial processes, most notably in coal and biomass power plants and gasification reactions. Thus there already exists a tremendous body of previous work on solid carbon oxidation, of which examples such as [30, 40-45] represent only a tiny fraction. Despite several decades of research however, solid carbon oxidation is still not fully understood and remains a very active area of continuing research.

Stoichiometrically, the global reactions between solid carbon and gaseous oxygen to form carbon monoxide and carbon dioxide are quite simple:

$$C(s) + \tfrac{1}{2} O_2 \rightarrow CO \qquad \text{Equation 2-1}$$

$$C(s) + O_2 \rightarrow CO_2 \qquad \text{Equation 2-2}$$

In addition, the direct oxidation of carbon monoxide is a key contributor to the global carbon conversion:

$$CO + \tfrac{1}{2} O_2 \rightarrow CO_2 \qquad \text{Equation 2-3}$$

One of the chief barriers in establishing any kind of general kinetic mechanism is the huge variation in the microscopic properties of solid carbon, which depend heavily on the carbon source. These microscopic properties in turn have a large impact on the many elementary steps involved in the overall reaction including bulk gas and solid pore transport, adsorption, surface migration, surface reaction, and desorption [46]. Despite the lack of a general mechanism, several semi-global intrinsic kinetic mechanisms have been proposed in the literature, two of which are especially relevant here and are discussed below.

One important generalization about global oxidation rate that has arisen from previous studies is the three-zone model for carbon particle burnout [47-49], which takes into account the concurrent processes of boundary layer oxygen diffusion, intra-particle oxygen diffusion, and surface adsorption and chemical reaction. Work by investigators such as Essenhigh, Walker, and Smith [44, 47, 50-52] has firmly established the existence of three distinct regimes in which chemical reaction or one of the diffusion processes limits the overall reaction rate. This theory has been widely accepted and used to interpret data in the coal and char literature for over 30 years. The Three Zone Theory is represented schematically in Figure 9.

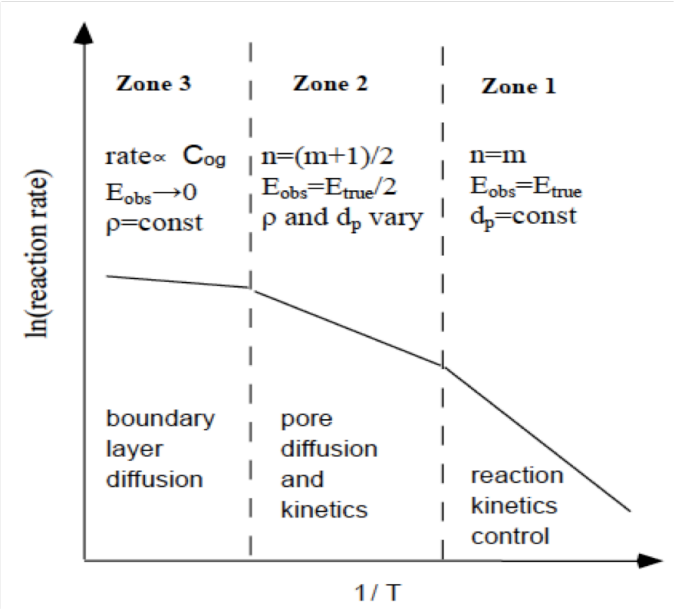

Figure 9 Three Zone Theory rate controlling zones for heterogeneous oxidation reactions [40, 41, 45].

Zone I burning occurs when chemical reactions at the carbon surface (including adsorption/desorption of reactants and/or products) limit the overall oxidation rate. Using reaction rates measured under these conditions it is possible to determine the intrinsic activation energy (which still includes adsorption, desorption, and multiple elementary steps). In Zone II burning, solid phase diffusion of oxygen (e.g., via pores) contributes significantly to slowing the overall oxidation rate. The effective global activation energy under these conditions is roughly half that of the intrinsic activation energy. Zone III burning occurs when external diffusion of oxygen from the bulk gas to the particle becomes rate limiting. Here the apparent activation energy is very small. Typically, particle burnout transitions from Zones I to III as the reaction (particle)

temperature increases. Thus it is possible to explore each type of behavior by selecting the temperature of experimental observation. In general, it is always prudent to consider the impact of all three types of processes when evaluating kinetic parameters.

The global n^{th} order rate equation is often used to describe char oxidation at conditions typical of industrial boilers [53-55]. The most common form is

$$q_{rxn} = k_s P_{O,s}^n = A \cdot \exp\left(\frac{-E_{A,obs}}{RT_p}\right) \cdot P_{O,s}^n \qquad \text{Equation 2-4}$$

This simple equation has proved useful for modeling char oxidation at atmospheric pressure over small temperature ranges [50]. Due to its simplicity, this model is commonly used in comprehensive boiler combustion models. While this rate equation does not explicitly account for pore diffusion, these effects can be implicitly included in the pre-exponential factor. This model has also been criticized for inadequately dealing with a wide range of experimental temperatures or high pressure data [56, 57]. However it is acknowledged to be effective over smaller ranges in those critical parameters. An additional weakness is that this model cannot be extrapolated between Zones I and II, so the reaction order is often observed to vary with experimental conditions, between the limits of 0 and 1. Recently, Hurt [53] suggested that fits of experimental data with Equation 2-4 can yield high fractional order due to surface heterogeneity. Simple surface reaction models that account for surface heterogeneity using power law functions have been proposed, but their use requires detailed surface characterization for the each fuel [58].

More detailed approaches for modeling carbon oxidation kinetics attempt to account for both the intrinsic reaction factors and pore diffusion effects. Intrinsic reaction models typically include explicit terms for Langmuir-Hinshelwood adsorption of oxygen and/or desorption of carbon dioxide [43]. Laurendaeau [59] suggested a way for including Langmuir-Hinshelwood effects in the intrinsic reaction rate, r, by:

$$r_{in}'''(C) = \frac{k_1 C}{1 + KC} \qquad \text{Equation 2-5}$$

where C is the molar concentration of carbon and k_1 and K are kinetic parameters representing the rate velocity and the equilibrium constant respectively.

A practical consequence of rate equations with a form like the above is that as oxygen concentration increases, the oxidation rate asymptotically approaches a maximum value due to the complete filling of all available adsorption sites on the carbon surface. Depending on the degree of surface site occupancy, it also means that the apparent reaction order in oxygen can vary between 0 and 1.

The speed at which the carbon particle oxidizes is dependent on both the reactivity and the rate at which the oxygen transfers from the bulk gas to the particle. This reactivity depends on the accessibility to oxygen within the pores of the particle and the velocity of the reaction between oxygen and the surface, also known as the intrinsic reactivity [41]. Intrinsic reactivity is defined as the reaction rate in the absence of mass transfer limitation. Pore diffusion effects in carbon oxidation are typically addressed with an effectiveness factor, η [60-62]. The effectiveness factor is the quantity by which the molar flux is multiplied by to account for diffusion resistance in the

conversion process, it is the ratio of the actual reaction rate to the intrinsic rate [41]. The effectiveness factor is a function of the Thiele modulus, Φ. [62], the dimensionless factor that relates the intrinsic rate of the chemical reaction in the absence of mass transfer resistance to the rate of diffusion for the particle. The Thiele modulus is defined as

$$\Phi = R_p \cdot \sqrt{D_{eff}} \qquad \text{Equation 2-6}$$

where R_p is the radius of the particle and D_{eff} is the effective diffusivity, which depends on the diffusing gas and the nature of the pore structure. The effective diffusivity is the combination of the diffusive resistance through the bulk and the Knudsen diffusion, D_K, which dominates in narrow pores.

Diesel Particulate oxidation by O_2 (as opposed to NO_x) has typically been considered as a first order process (in carbon) with a temperature dependence that obeys the Arrhenius equation:

$$r = k \cdot [C]^{\alpha}[O_2]^{\beta} \qquad \text{Equation 2-7}$$

$$k = A \cdot \exp\left(\frac{-E_A}{RT}\right) \qquad \text{Equation 2-8}$$

where r is the reaction rate in mol/min, k is the reaction rate velocity, A is the frequency factor, E_A is the activation energy in J/mol, R is the universal gas constant 8.314J/mol-K, T is the absolute temperature in K, [C] is the molar concentration of carbon, $[O_2]$ is the molar concentration of oxygen and α and β are the reaction orders in carbon and oxygen respectively.

Reported kinetic parameter values for diesel particulate oxidation by O_2 vary widely [63]. Activation energies for non-catalyzed oxidation range from 36 kJ/mol [64] all the way up to 170 kJ/mol [65, 66], close to the activation energy of graphite at 188 kJ/mol [67]. Reaction orders in carbon are reported to be ⅔, in the range representative of the shrinking core model, but this has yet to be proven accurate for diesel particulate [68]. To further complicate matters, reaction orders in oxygen have been reported in orders ranging from ½ [64] to 1 [68]. Thus without direct experimental information, it would be impossible to reliably use the currently available kinetic data for estimating the oxidation rates of previously untested diesel particulates.

Early studies of the uncatalyzed oxidation of diesel particulate compared to flame particulate indicated that diesel particulate oxidation was more complex [68]. This study also proposed Printex (a commercially available carbon black) as a reference standard for oxidation reactivity [13, 69]. In these studies, the particulates (diesel and Printex) were milled to uniform size, but the SOF of the diesel particulate was not measured nor removed. Scattering in the data prevented determination of the kinetic parameters, and it was proposed that the volatile hydrocarbons present on the particulate were complicating factors.

More recent innovative work by Yezerets, et al [69-72] has begun to clarify the diesel particulate reactivity to oxygen. In 2002, they established a flow reactor methodology for measuring particulate kinetic parameters, and this methodology is the basis for the kinetic measurements set out in this research proposal. Their work focused on the oxidation of devolatilized, heavy duty (HD) diesel particulate and a carbon black

model particulate with 10% O_2. Two types of experiments were conducted: temperature programmed oxidation (TPO) and a step-response technique. Experiments were carried out on samples that were first pretreated with temperature programmed desorption (TPD) under inert gas to remove adsorbed hydrocarbons. The devolatilization was done in order to normalize the particulate samples, thereby eliminating the impact of the SOF. These methods are described in Chapter 3.

Using the above experimental techniques, Yezerets et al determined that there was a significant difference in the behavior of the diesel particulate and the carbon black, including very different burnout profiles. The differences observed between the samples lead the researchers to believe that the behavior of the sample depends significantly on its properties, indicating that carbon black may not be an appropriate 'reference particulate'. Of particular interest here, Yezerets et al observed an apparent increase in the activation energy as burnout progressed. This correlation between activation energy and burnout was again confirmed by Yezerets et al in 2003, leading the authors to conjecture that the presence of some type of highly reactive surface species in the devolatilized particulate produced an initial boost in reactivity that diminished with time [71].

Additional work by this same group in 2005 with the oxidation pulse technique to minimize local temperature variations confirmed the reactivity changes in the early stages of burnout and quantified the amount of highly reactive particulate to be approximately 10-25% of the initial sample [71]. The remainder of the particulate appeared to have relatively unchanging properties. Overall, the observations of this

group indicated that the oxidation rate for their devolatilized HD particulate could be approximated by:

$$r = k \cdot [C]^{\alpha}[O_2]^{\beta} \qquad \text{Equation } \mathbf{2\text{-}7}$$

the reaction velocity constant at each was calculated by

$$k = \frac{r}{[C]^{\alpha}[O_2]^{\beta}} \qquad \text{Equation 2-9}$$

and the activation energy was found from the Arrhenius relationship. The reaction was found to be first order in carbon, with $\alpha = 1$, $\beta = 0.61 \pm 0.03$ and the activation energy, E_A, was found to be 137 ± 8.1 kJ/mol. However, it should be noted that the concentration of carbon is changing over the reaction, even at a steady temperature.

Stamelos [39, 73] and researchers studied the impact of the volatile hydrocarbons on the oxidation of diesel particulate in a DPF, but they did not attempt to estimate Arrhenius kinetic parameters. The relative percentage of SOF was measured by TGA for particulate generated by a range of engine conditions and a speed-load vs. volatiles map was created. Chemical analysis and identification of the compounds of the volatile fraction was not attempted. Unpredictable regeneration behavior in DPFs was correlated to low exhaust temperature conditions, which resulted in a relatively high volatile content. The investigators noted that further research to better understand the complex relationship between SOF and particulate oxidation was needed, stating “The successful introduction of an effective, but simple kinetic scheme that addresses both dry soot oxidation and adsorbed VOF oxidation must be based on a detailed experimental study...”

2.6 Summary

Previous studies have demonstrated that diesel particulate matter is composed primarily of a complex aggregated framework of graphitic and amorphous carbon nanoparticles. Attached to this framework is a complex mixture of volatile hydrocarbons that can influence the overall oxidation reactivity of the carbon and the way its oxidation rate varies with particle burnout. While some very useful techniques have been developed for measuring diesel particulate oxidation behavior, the relationship among volatile hydrocarbons (MC), Arrhenius kinetic parameters, and burnout trajectory are poorly understood. This is especially true for diesel particulates produced by biodiesel and biodiesel blend fuels. It appears likely that some of the previously developed techniques for modeling coal and char oxidation may also be useful for describing and understanding diesel particulate oxidation. This is the operating hypothesis behind the experimental approach described in the next chapter.

3 Experimental Setup

3.1 Engine and Exhaust System Setup

Particulate samples were generated in a 1999 1.7L Mercedes Benz direct-injection common rail diesel engine as shown in Figure 10. This engine has been well-characterized previously [2, 74]. The engine specifications are listed in Table 3-1. The engine was operated with a dSpace flexible engine control system. This system is set up to emulate the factory calibration for conventional diesel combustion and is capable of actuating the EGR valve, the intake throttle, fuel rail pressure, start of injection (SOI) timing, injection duration and the number of injection events.

The intake air supplied to the engine is conditioned for constant temperature and humidity. In-cylinder pressure measurements for combustion analysis were recorded using Kistler piezoelectric pressure transducers and an AVL Indimodul. Fuel consumption was measured by a Max Machinery 710-213 positive displacement volumetric flow measurement system. Air consumption was measured with a laminar flow element and intake mass-airflow sensors.

The engine was run at a single steady-state point, 1500rpm, 2.6bar brake mean effective pressure (BMEP) with 30% exhaust gas recirculation (EGR) for 12 hours (one 8 hour day + one 4 hour day) for each fuel. This low load point was chosen because it is the heaviest-weighted point of the multimode steady-state approximation of the US FTP-75. For each fuel blend, the engine performance parameters (speed, load, %EGR) were set, and fueling rate, rail pressure, and SOI were allowed to float to meet the

demand; the engine was not optimized for each fuel. Between experiments, the fuel system was flushed and the engine was run at a higher load-speed point to burn out any residual fuel.

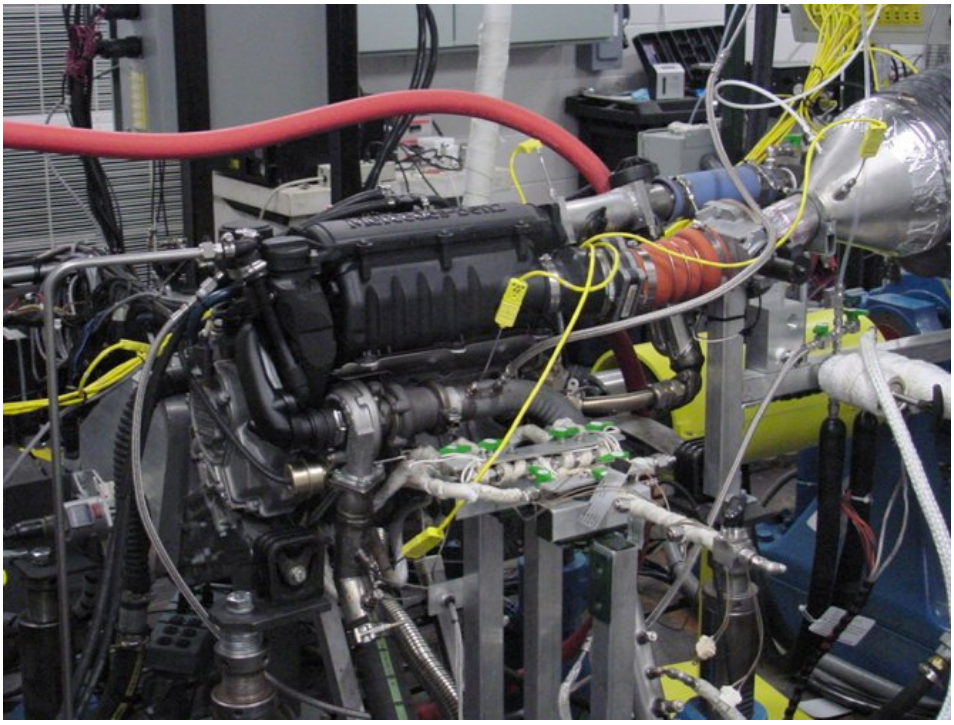

Figure 10 Direct-injection 1.7L Mercedes Engine

Bore (mm)	80
Stroke (mm)	84
Displacement (L)	1.7
Number of Cylinders	4
Compression Ratio	19.5
Valves per Cylinder	4
Piston Bowl	Re-entrant
Fuel Injection	Common Rail
Injector diameter (mm)	0.169
Number of injector holes	6
Rated Power (kW)	66
Rated Torque (Nm)	180

Table 3-1 Engine Specifications

A slipstream of raw engine-out gas was maintained at 190°C with a stainless steel heated line and sampled downstream of a heated filter to remove particulates. Standard automotive exhaust gas instrumentation was used to measure basic exhaust chemistry. The exhaust gas was chilled to remove water before nondispersive infrared (NDIR) instruments were used to measure CO and CO_2 and a paramagnetic detector (PMD) was used to measure the intake and exhaust O_2 concentrations. Total hydrocarbons (THCs) were measured by heated flame ionization detectors (HFIDs) and nitrogen oxides (NO_x) were measured with heated chemiluminescence detectors

(HCLDs). An AVL 415S optical reflectometer was used to measure PM emissions in the raw exhaust. The filter smoke number (FSN) is determined by linear measurement of the blackening of the filter paper. While reflectometry is not a direct measurement of particulate, it is an accepted estimate of the PM emissions at steady state conditions.

A microdilution tunnel, shown in Figure 11, was used to provide a noncondensing dilute exhaust stream for analyzing exhaust chemistry based on the design by Kittelson [75]. The raw exhaust sample was maintained at 190°C in a heated stainless steel sample line to the dilution tunnel. The diluter was heated and insulated to maintain a sample temperature of 50°C. Dilution ratio was measured by observing gas concentrations in the raw exhaust and dilute sample and confirmed by volume flow measurements. The microdilution tunnel was run at a 10:1 dilution ratio for all fuels.

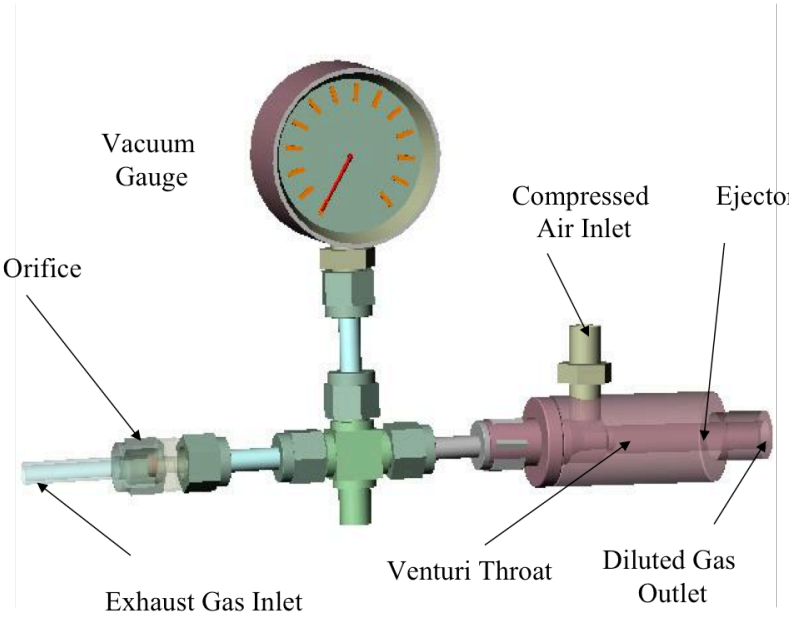

Figure 11 Schematic of microdilution tunnel [75].

A variety of exhaust samples were taken from both the raw and dilute exhaust. Sampling locations are shown in Figure 12. An uncatalyzed DPF was installed approximately 1 meter downstream of the turbine exit to collect particulate powder. No diesel oxidation catalyst (DOC) was used before the DPF. Tailpipe-type particulate emissions were collected from the dilution tunnel using 47mm Teflon™ coated quartz fiber filters (Pall TX40HI120) that were equilibrated and weighed before and after exposure to determine particulate mass deposited. Gas phase tailpipe emissions were collected via Empore™ (3M), a C18 coated membrane, loaded behind the Teflon filter. DPF-type particulate for chemical analysis was collected from the raw exhaust, just before the in-line DPF using 1” x 3” NGK558 HoneyCeram miniDPFs.

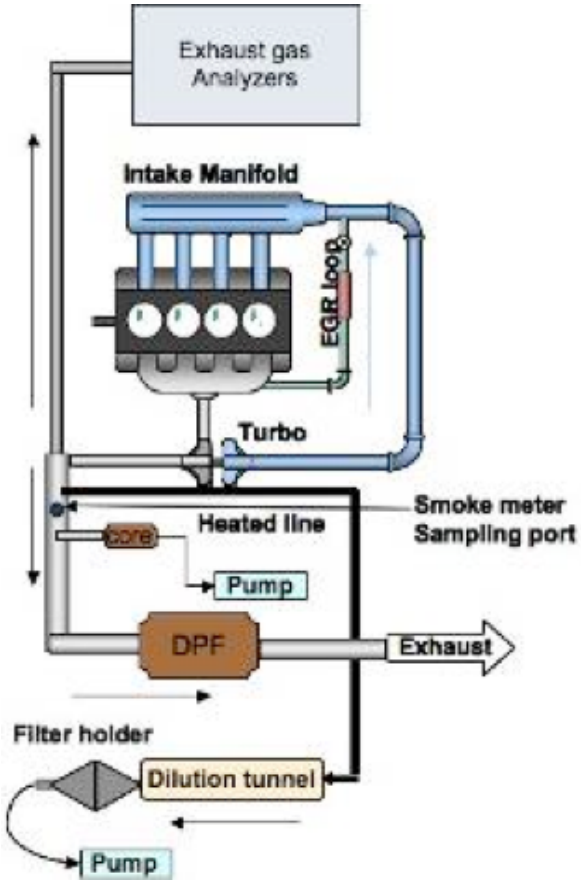

Figure 12 Diagram of engine and sampling locations.

3.2 Fuels

Soy Gold ™ soy methyl ester biodiesel (B100) was purchased from Ag Processing Inc. (Omaha, NB) and conventional 2007 certification ULSD was purchased from Chevron Phillips Specialty Chemical Company (The Woodlands, TX). Volumetric blends of 5%, 10%, 15%, 20% biodiesel in ULSD were splash blended. The blends are designated by “B#”, where the number is the percentage of biodiesel in ULSD. Four of the fuels (ULSD, B5, B20, B100) were monitored for combustion and all six of the fuels

were used to generate particulate samples. The parent fuel properties are given in Table 3-2.

Property	ULSD	B100
Calculated % Oxygen (by mass)	0	11.1
Cetane Number	43	52
Specific Gravity	.845	.886
Viscosity (cSt)	2.3	4.0
Calculated Lower Heating Value (MJ/kg)	42.9	40.5
Sulfur (ppm)	6.8	1.1
Sodium, ppm	0	2.8

Table 3-2 Fuel Properties

3.3 Nanostructure Characterization Methods

Powdered particulate removed from the uncatalyzed DPF was used for physical characterization experiments. Dr. Randy Vander Wal at Universities Space Research Association (USRA) performed high-resolution transmission electron microscope (HRTEM) imaging. A brief description of the equipment and methodology follows. Detailed descriptions of the experimental method can be found in [76].

TEM images were taken using a Phillips CM200 with a Gatan image filter for digital imaging with live Fourier transforms with a of 0.14 nm nominal resolution using a LaB_6 filament. The instrument was operated at 200 keV. Samples for imaging were created by dispersing a small amount of the DPF-collected particulate samples onto a

TEM grid. Images were obtained from at least three locations on the grid. At minimum, five aggregates were surveyed to establish the consistency of the observations.

Quantification of the HRTEM images was conducted by two separate analysis algorithms. When describing HRTEM images, lamella denotes the physical carbon layer plane segments. Due to the appearance of the individual atomic layer planes, which appear as fringes within the image, the processed skeletal structures are referred to as fringes. The parameters extracted from the quantification analysis are the fringe length, the linear distance of the atomic layer planes, the fringe separation, the mean distance between adjacent planes, and the tortuosity or fringe curvature. Fringe length and separation are calculated by the first routine, while tortuosity is calculated by the second. In order to avoid artifacts, skeletal images, as shown in Figure 13 are redrawn for calculations as represented in Figure 14.

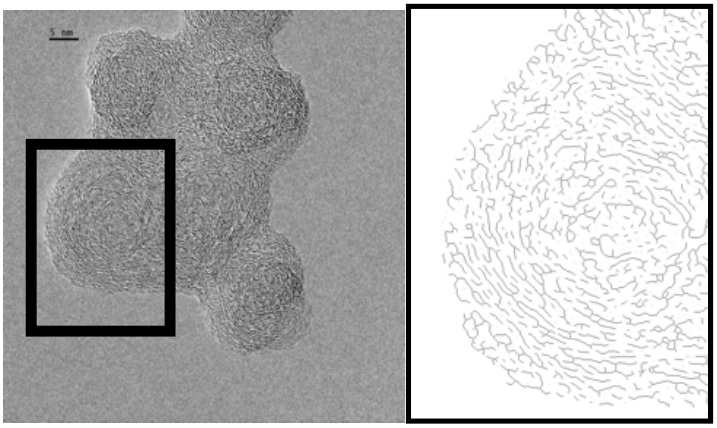

Figure 13 TEM image and fringe analysis skeletal structure of particulate.

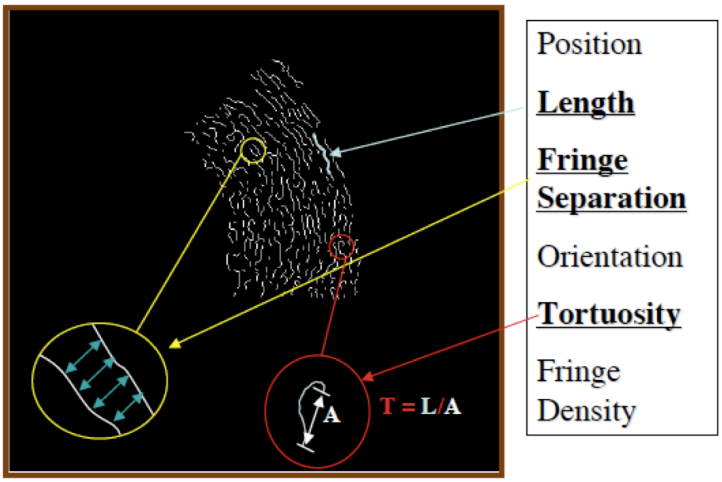

Figure 14 Schematic of Fringe Quantification [77].

3.4 Chemical Speciation Methods

Three distinct samples were collected for chemical speciation: DPF particulate, tailpipe particulate and gas phase tailpipe emissions. The DPF particulate was collected off the take down pipe, approximately 0.5m before the full size DPF, on 1" x 3" miniature NGK 558 cordierite DPFs (NGK, Novi, MI) shown in Figure 15. Raw exhaust was pulled through the miniDPFs for 30 to 45 minutes using a pump. MiniDPFs were weighed before and after filling to determine the particulate mass collected. Tailpipe-type particulate emissions were collected from the dilution tunnel using 47mm Teflon coated quartz filters (Pall TX40HI120) that were equilibrated (for humidity) and weighed before and after exposure to determine particulate mass deposited. Gas phase tailpipe emissions were collected by Empore™ (3M), a C18 coated membrane filter, loaded behind the Teflon filter and sampled via the dilution tunnel.

The soluble fraction of the mobile carbon portion (SOF) of the particulates from both the Teflon coated quartz filters and miniDPFs were extracted in 50/50 Hexane/Acetone (Fisher Scientific) via microwave-assisted extraction according to EPA Method 3546 [78], a procedure developed for extracting water insoluble organic compounds from solid waste and used with great success previously [2, 36, 79]. The MARS microwave extraction unit was purchased from CEM. The Empores were extracted at atmospheric temperature and pressure with Ethyl Acetate and Methylene Chloride (Fisher Scientific). The extracts from all samples were concentrated to 100 μL, and analyzed by GC/MS to speciate the SOF. A 60m DB-5 column was used in a Hewlett-Packard GC, with on-column sample injection. SOF species were individually identified, then grouped into heavy and light paraffin, olefin, polynuclear aromatic (PAH) and methyl-ester categories for comparison.

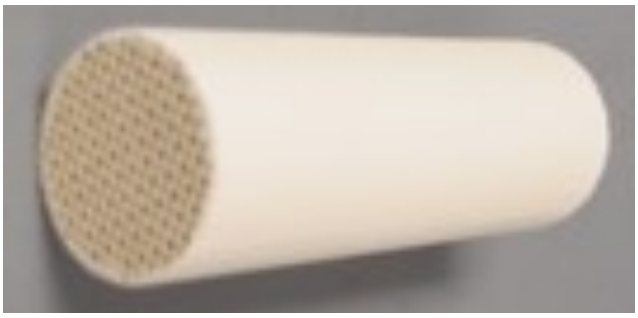

Figure 15 Miniature DPF (1"x 3") for solvent extraction.

3.5 Microreactor Experiments

The microreactor system (Figure 16) can be used to measure a variety of fundamental properties of a particulate sample including surface area (by BET), volatile content, O_2 storage capacity, and kinetic (Arrhenius) parameters for oxidation by O_2.

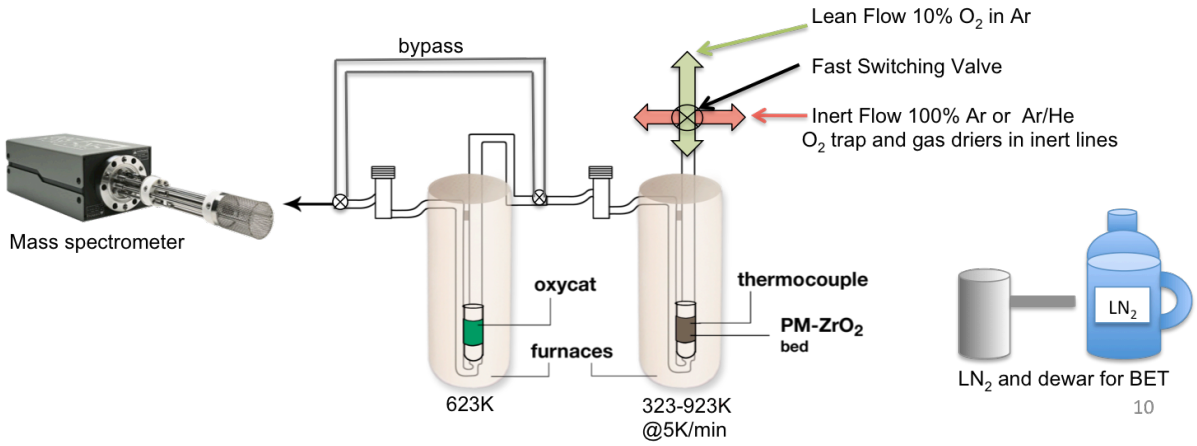

Figure 16 Microreactor system

The system consists of a two-stage quartz U-tube, plug flow reactor (Figure 17), with reaction products analyzed by a quadrupole mass spectrometer. It is equipped with a fast switching valve and two independent gas manifolds supplied by digital mass flow controllers flowing bottled gases. Gas driers and O_2 traps are installed in the inert gas lines to assure dry, oxygen-free inert flow to minimize the background. Each stage of the reactor is outfitted with a thermocouple, in order to monitor the bed temperature, and a digitally controlled furnace capable of 950°C. The sample, mixed with Yttrium stabilized Zirconium oxide beads (YZrO2) for thermal stability, is contained in the first reactor. A second reactor containing an oxidation catalyst (held at 350°C) can be

bypassed or used in series to completely convert oxidation products or oxidize volatiles evolving from the sample. The system was regularly calibrated with 5%, 1% and 0.5% CO_2.

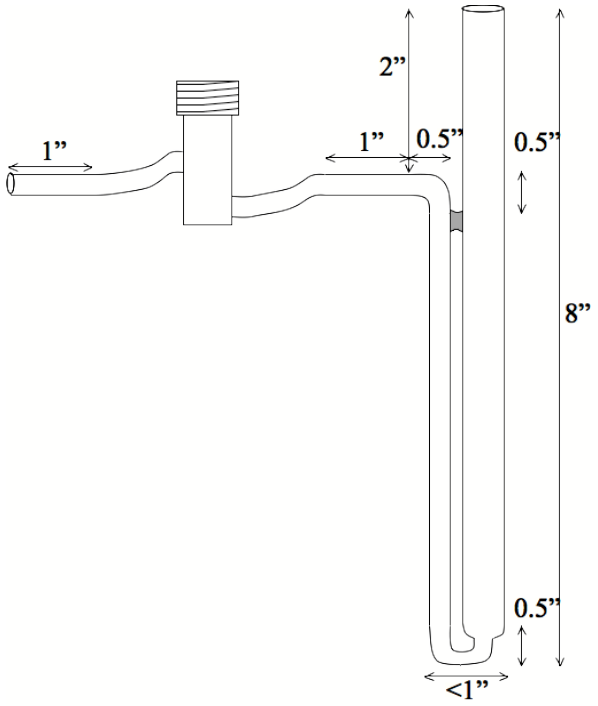

Figure 17 Quartz U-tube reactor schematic.

3.5.1 Microreactor Sample Preparation

Samples were prepared in a clean, dry U-tube for each experiment. Tubes were first cleaned with soap (Alconox, Fisher Scientific) and water, then rinsed with acetone and dried in a 150^{o}C furnace. An end plug was formed with ~0.15g quartz wool rolled into a cylinder and pushed down into the end of the U-tube. Particulate samples in the range of 15-20mg were measured in weighing funnels and transferred to the U-tube on

top of the quartz plug, forming the particulate bed. For thermal stability of the bed, approximately 1g of 800mm Y-ZrO_2 was added to the particulate bed. Another quartz plug was placed on top of the particulate/ZrO_2 bed and the total bed height of particulate plus ZrO_2 beads was ~12mm.

3.5.2 BET Surface Area Measurements

Specific surface area was measured for nascent particulate and devolatilized particulate and serially for particulate samples in various stages of burnout. BET theory [80] extends the monolayer Langmuir theory to use the physical adsorption of gas on a solid surface as a basis for the measurement of specific surface area of a material. The BET equation for the adsorption isotherm is

$$\frac{1}{v[(P_o/P)-1]} = \frac{c-1}{v_m c}\left(\frac{P}{P_o}\right) + \frac{1}{v_m c} \qquad \text{Equation 3-1}$$

where P and P_o are the equilibrium and saturation pressure, v is the adsorbed gas volume, v_m is the volume of a monolayer of gas and c is the BET constant, shown in

$$c = \exp\left(\frac{E_1 - E_L}{RT}\right) \qquad \text{Equation 3-2}$$

where E_1 and E_L are the heat of adsorption for the first layer and the heat of liquefaction. To calculate the specific surface area, the left hand side of (1) is plotted against P/P_o in the range of $0.05 < P/P_o < 0.35$ and the slope and intercept of the line are then used to calculate v_m and c according to equations

$$v_m = \frac{1}{slope + intercept} \qquad \text{Equation 3-3}$$

$$c = 1 + \frac{slope}{intercept} \qquad \text{Equation 3-4}$$

Finally, the specific BET surface area can be calculated

$$S_{BET} = \frac{v_m N_A s}{aV} \qquad \text{Equation 3-5}$$

where N_A is Avogadro's number, s is the adsorption cross-section, V is the molar volume of the adsorbent, and *a* is the molar weight of the adsorbed species.

Specific surface area was measured by flowing seven concentrations (1.5 to 7.5%) of Argon adsorbent in Helium through a particulate sample prepared as described in section 3.5.1. Flow was directed only through the first reactor; reactor 2 was bypassed. The effluent gas was monitored by mass spectrometer, and the seven data points were compiled into a BET plot. At least three samples of each type were measured for statistical precision.

3.5.3 Oxygen Chemisorption & Active Surface Area Measurement

Oxygen chemisorption was measured for nascent particulate and devolatilized particulate and serially for particulate in various stages of burnout. The method was adapted to a flowing system from Boehman et al. [81]. Particulate samples, prepared as described in section 3.5.1 were heated to 200^{o}C under 100% Argon. The inlet gas was then switched to 20% O_2 in Ar and the samples were isothermally exposed for 10 hours.

The inlet gas was then switched back to 100% Argon and the sample was held at 200°C for 1 hour to remove loosely bound oxygen. To measure the amount of oxygen chemisorbed to the particulate, the oxygen was then removed by running a temperature ramp from 200°C to 650°C at 10°C/min and recording the concentration of CO_2 evolved. Both reactors were used in this experiment. The mass of O_2 adsorbed per gram of particulate can be converted to an active surface area by

$$ASA = \frac{N_{O,ads} * A_O * N_A}{M_s} \quad \text{Equation 3-6}$$

where $N_{o,ads}$ is the number of moles O adsorbed, A_O is the area of an O atom, N_A is Avogadro's number and M_s is the mass of the particulate sample.

3.5.4 Temperature Programmed Desorption

Temperature programmed desorption, or TPD, is a method by which the volatile organic fraction (VOF) of the mobile carbon evolved from the particulate samples can be quantified. A particulate sample was prepared as described in section 3.5.1 and was heated under 100% Argon from 50°C to 650°C at 5°C per minute, then held at 650°C for 30 minutes. A side stream of 10% O_2 bypassed the particulate sample and was fed to the secondary reactor, containing an oxidation catalyst, and CO_2 evolution was recorded. Volatile mass was calculated assuming a 1:1 CO_2 to volatile C ratio.

3.5.5 Temperature Programmed Oxidation

Temperature programmed oxidation, or TPO, is a powerful tool used to examine the oxidation behavior of a combustible sample or catalyst [69-71]. Shifts in TPO profiles are attributed to differences in the oxidative reactivity between samples.

Nascent particulate and fixed carbon samples for TPO were prepared as described in section 3.5.1. Samples were flushed with 100% Argon at room temperature to establish a baseline, then the gas flow was switched to 10% O_2 in Ar before the temperature ramp from 50^{o}C to 650^{o}C at 5^{o}C/min was started. Both reactors were used in this experiment and CO_2 evolved was measured by the mass spectrometer.

3.5.6 Isothermal Determination of Kinetic Parameters

Isothermal, differential experiments decouple several of the effects that contribute to the complexity of measuring kinetic parameters [72]. Differential, isothermal measurement of the rate of reaction over the full range of sample burnout and over a range of temperatures, is necessary to determine the activation energy of the sample without artifact.

Devolatilized particulate samples were prepared as described in section 3.5.1. The samples were heated to the temperature of interest under 100% Argon, then the fast switching valve was used to cycle between lean (10% O_2 in Ar) and inert (Ar) flows. To keep conversion differential and isothermal in any one pulse, the lean pulse durations were kept to between 2s and 30s depending on the temperature. The inert period between lean pulses was set at 5 minutes. CO_2 evolution was measured by the

mass spectrometer and the reaction rate was directly measured from the rate of CO_2 production in each lean pulse.

The isothermal, differential experiments allowed us to isolate the kinetics from the reactor system, therefore is not necessary to model the flow reactor in order to model the data. The reactions are assumed to be first order in carbon and the O_2 concentration was held constant, therefore the rate equation

$$R = k[C]^1[O_2]^\beta \qquad \text{Equation 3-7}$$

becomes

$$R = k'[C] \qquad \text{Equation 3-8}$$

where k' is the effective rate constant.

$$k' = k[O_2] \qquad \text{Equation 3-9}$$

Integrating the rate expression,

$$d[C]/dt = k'[C] \qquad \text{Equation 3-10}$$

gives

$$ln[C/C_o] = k'*t \qquad \text{Equation 3-11}$$

where $[C_o]$ is the initial concentration of carbon. Therefore, a linear plot of $ln[C/C_o]$ against time for each isothermal experiment would confirm the first order assumption and allow for the computation of the Arrhenius parameters.

3.6 Summary

In this chapter, the experiments performed in order to measure oxidation characteristics of DPF particulate produced by different biodiesel-conventional fuel blends are detailed. The particulate samples were also subjected to a range of physical and chemical measurements in order to better understand the mechanisms by which fuel-related changes to oxidation reactivity are brought about. These additional characterizations included: the relative fixed and mobile carbon (FC and MC) fractions; the chemical composition of the organic fraction; the particulate surface area and major structural and chemical features revealed by electron microscopy. The results of the experiments described in this chapter are presented in Chapter 4 with additional details provided in the Appendices.

4 Results and Observations

In order to isolate the differences in oxidation behavior to fuel effects, it was important to create particulate samples under conditions as similar as possible. A single speed-load point of 1500rpm, 2.6 bar BMEP, the most heavily weighted point of the US FTP, was chosen for these experiments. Particulate samples were generated in a 1999 1.7L Mercedes Benz direct-injection common rail diesel engine for four fuels, ULSD, soy methyl ester B100 and volumetric blends of 5%, and 20% biodiesel in ULSD. The blends are designated by “B#”, where the number is the percentage of biodiesel in ULSD.

Particulate samples were collected from the full exhaust stream in an uncatalyzed DPF, a separate filter for each fuel, mounted in under-body style. No diesel oxidation catalyst (DOC) was used in the exhaust system. Combustion experiments were run for 12 hours to load particulates into the filter, then the filters back-flushed with pressurized air to collect the powder samples, which were stored under inert.

Nascent particulate samples were first evaluated for differences in reactivity by TPO then the EC and OC components were studied separately. The focus of this work is on the differences between ULSD and B100 particulates, though blends were evaluated in some experiments. The fixed carbon samples were created by devolatilizing nascent particulate matter under inert in TPD. Since FC is the major component of PM, ULSD fixed carbon and B100 fixed carbon are investigated in depth. Fixed carbon samples were evaluated over a range of temperatures to measure Arrhenius parameters.

Once the kinetics of the FC were determined, the focus shifted to investigating the physical and chemical nature of the particulate in order to understand the differences seen in the samples.

4.1 Particulate Formation Experiments

Particulate samples for kinetic and physical analysis were collected in an uncatalyzed DPF installed in the exhaust system. Samples for chemical analysis were collected on miniature DPFs in the exhaust line and Teflon filters and membranes from the dilution tunnel. Combustion characteristics of the engine during particulate sample collection were consistent with previous published reports [82-85] and kept relatively constant between fuels, as seen in Figure 18 and Figure 19. B20 showed slightly lower rate of peak heat release as compared to the other fuels, but had the same in-cylinder pressure. Additional combustion parameters are shown in Table 4-1. We have good confidence that the particulate samples were created under similar temperature and pressure conditions – the most important variables in particulate formation, with the fuel being the only variable.

Fuel	Speed	Torque	Pilot Injection	Main Injection	Rail P	Exhaust T	Fuel	Intake Air
	rpm	lbft	(SOI), CAD	(SOI), CAD	Bar	°C	g/s	SCFM
ULSD	1500	26.4	285 (-18.2)	533 (-2)	316	210	0.410	30.3
B5	1500	26.4	288 (-18.2)	543 (-2)	317	207	0.411	31.6
B20	1500	26.4	290 (-18.2)	536 (-2)	316	207	0.417	31.8
B100	1500	26.4	277 (-18.2)	585 (-2)	322	213	0.464	30.5

Table 4-1 Additional Combustion Data.

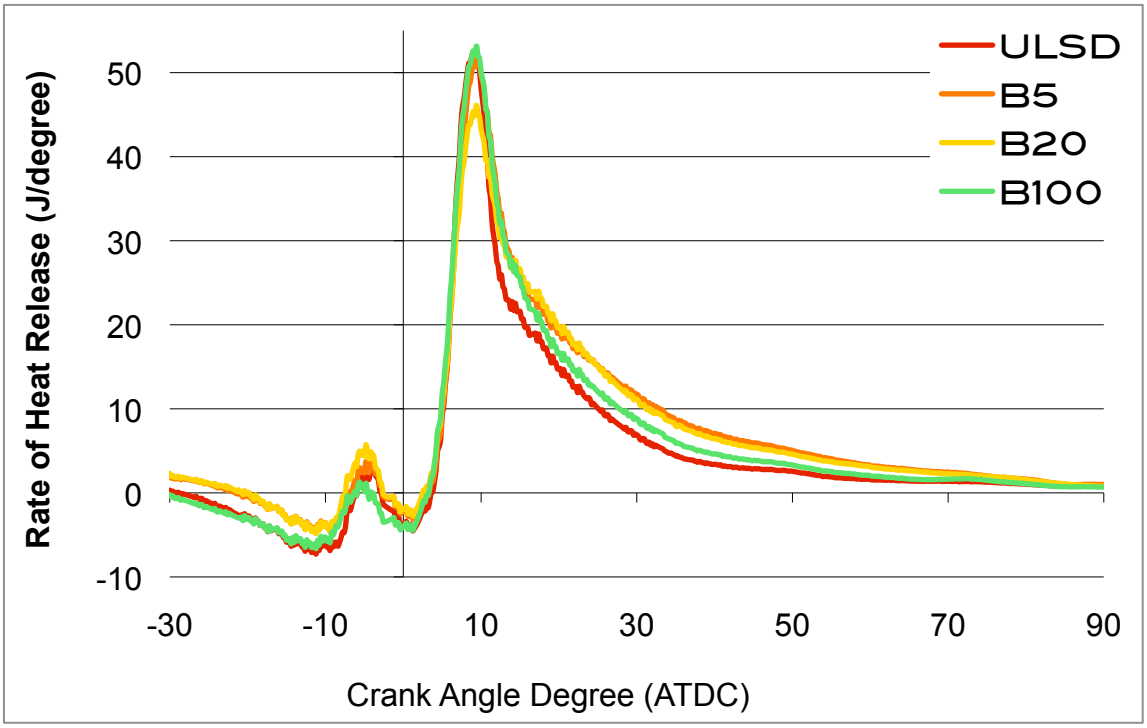

Figure 18 Cylinder-averaged Heat Release Rate vs. Crank Angle Degree

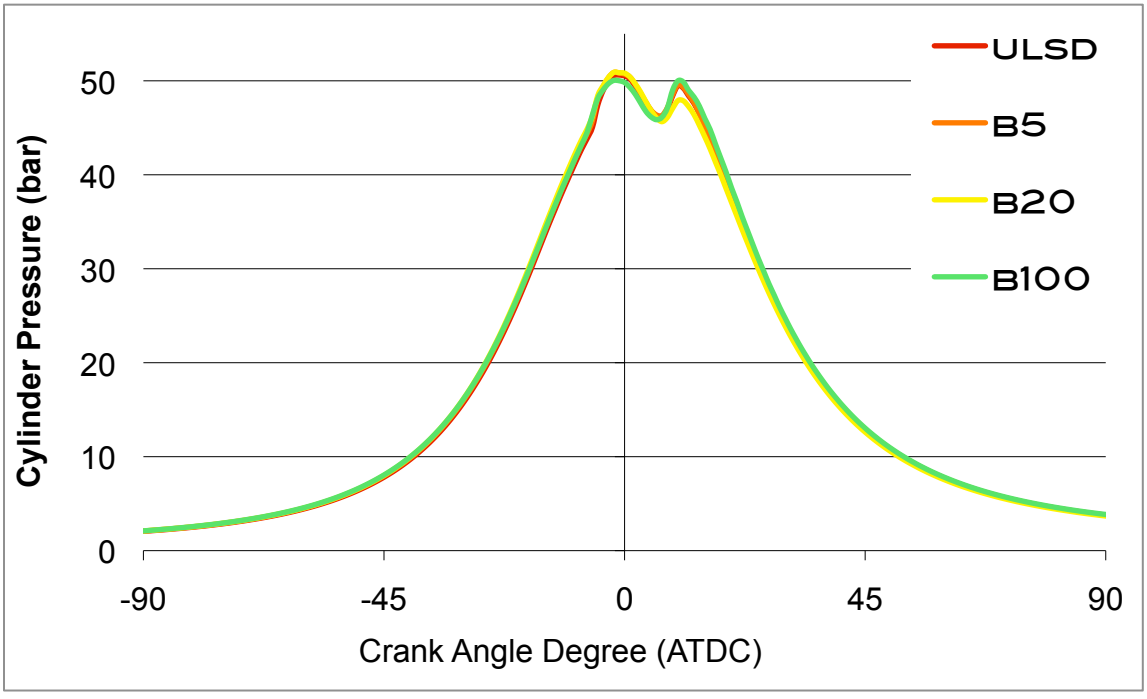

Figure 19 Cylinder-averaged Pressure Trace vs. Crank Angle Degree.

Generally, fueling rate increased with increasing biodiesel blend, though the total hydrocarbons (THCs) and combustion efficiency decreased slightly. NO_x emissions, decreased for the B5 and B20 intermediate blends, but were higher, as expected for B100 [83, 86]. Particulates, measured by absorbance, were expected to decrease with biodiesel blending [83]; however, they were measured to increase slightly for B5 particulates, returned to ULSD particulate levels for B20 particulate and decreased dramatically for particulates from B100. It is worth noting that the concentration measured by opacity can be deceiving, since the absorbance measurement is based on carbon (FC) blackening the paper. B100 particulates tend to have a higher SOF/FC ratio than ULSD particulate and therefore have less 'blackening' EC for the same mass. Fuel Consumption and emissions trends are shown in the following figures.

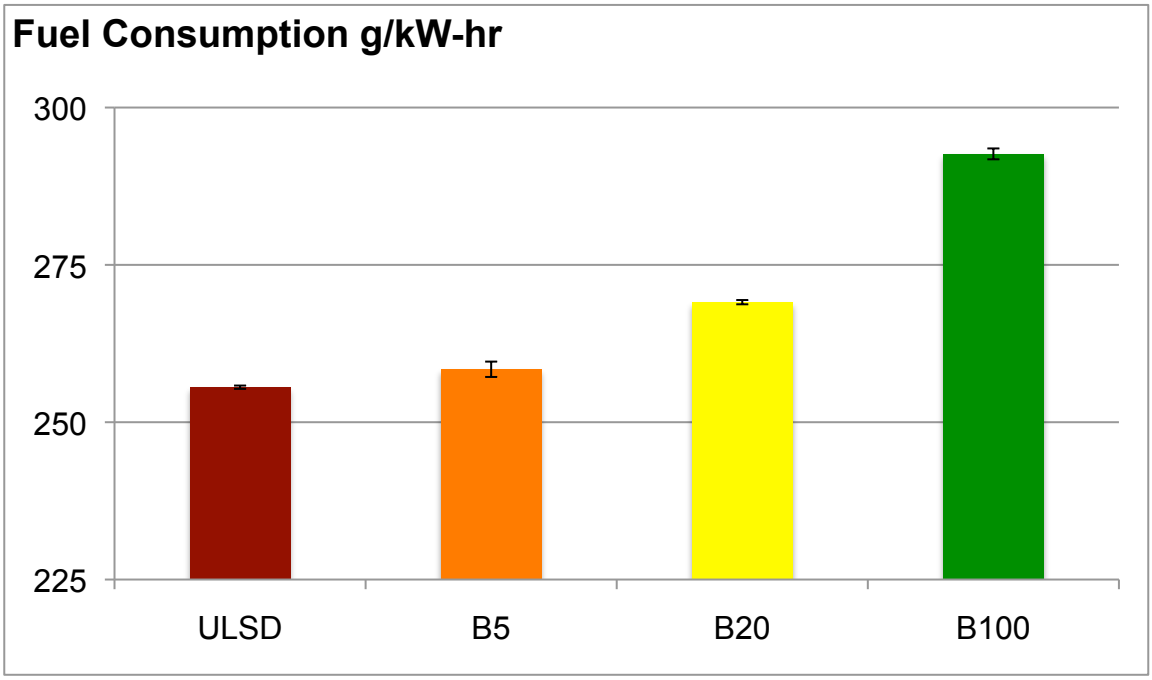

Figure 20 Fuel consumption with biodiesel blend level.

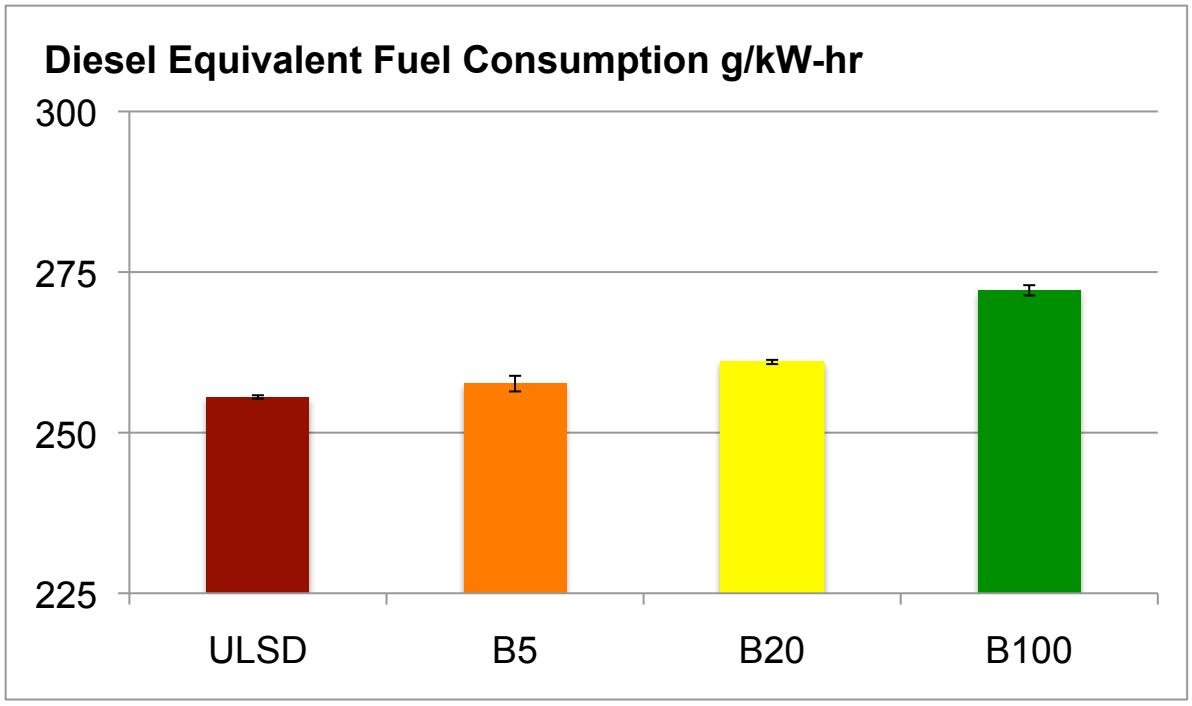

Figure 21 Fuel consumption normalized to energy content of the fuel.

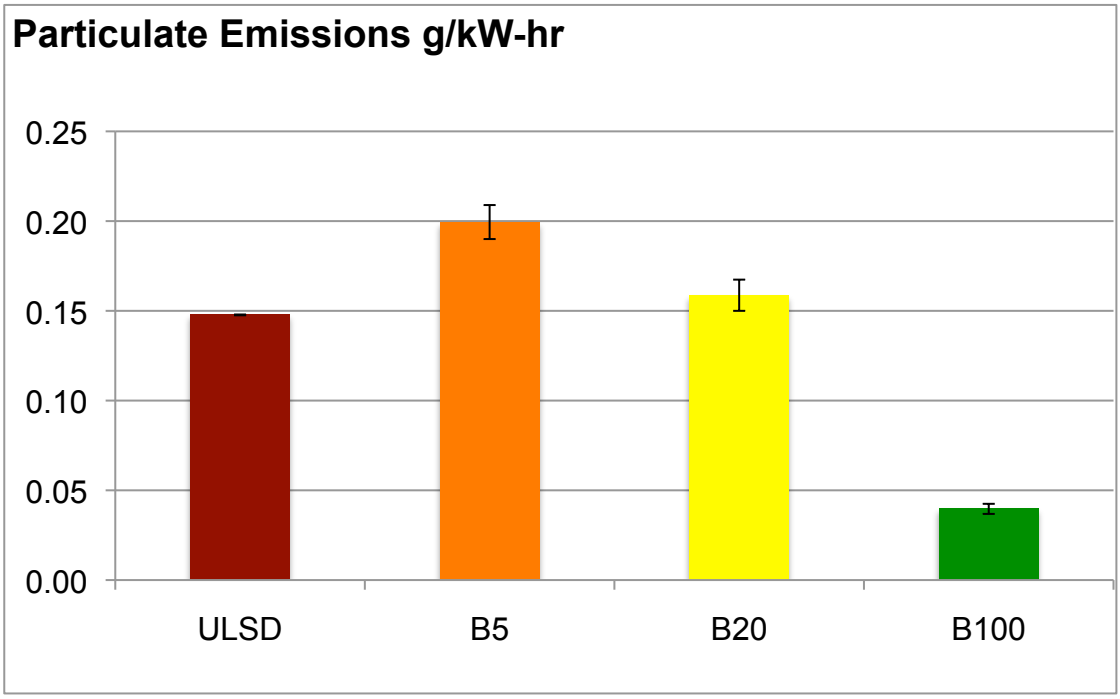

Figure 22 Particulate emissions with biodiesel blend level.

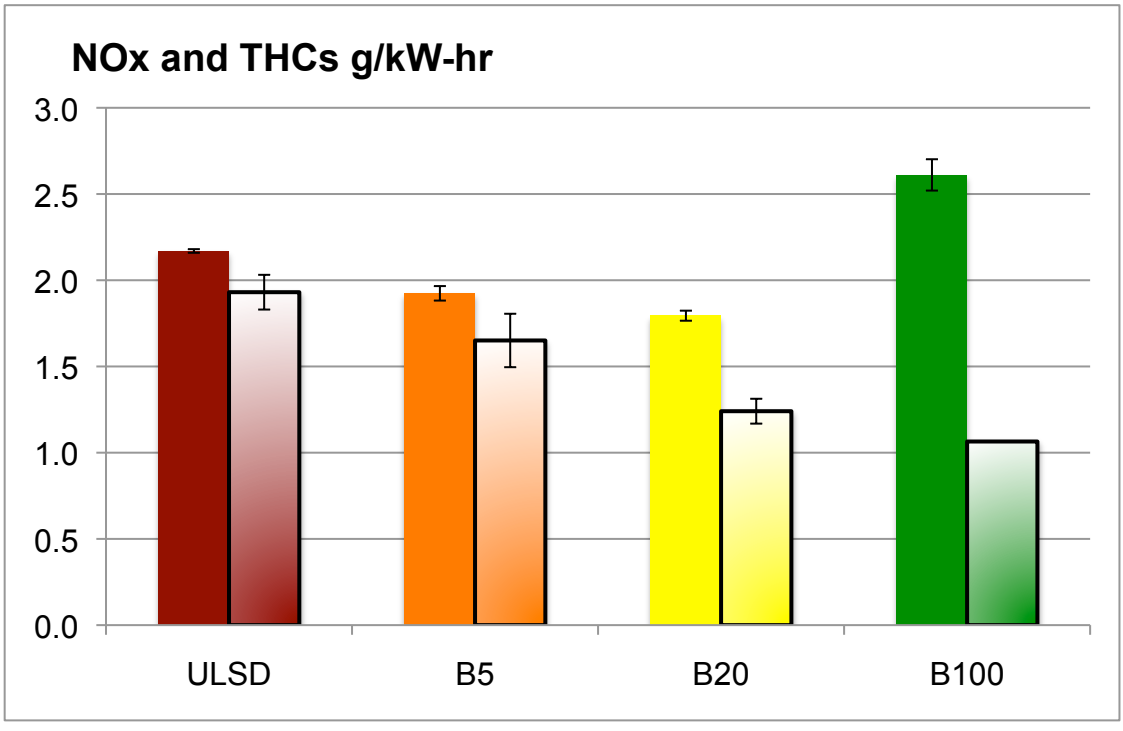

Figure 23 NO_x (solid) and THC (outlined) emissions with biodiesel blend level.

In the above experiments, we found that fuel consumption and total exhaust hydrocarbons trended consistently higher and lower, respectively, with increasing biodiesel content. Increased fuel consumption is expected since the energy content of biodiesel is lower. Particulate and NO_x emissions had more complicated trends with increasing biodiesel blending. Initial oxygenated fuel addition increases the soot production, once the level of oxygenate reaches approximately 20%, the soot production diminishes, similar to what is seen in laboratory diffusion flames. NO_x decreased initially with biodiesel blending, then increased significantly for neat biofuel, as previously reported in the literature [83, 87].

The combustion experiments, carried out to generate the particulate samples for this study, were shown to be consistent with published reports for biofuel and biofuel blends [83, 86, 87]. The uniformity of the in-cylinder pressure and exhaust temperature, the most important parameters for particulate formation, during combustion give us confidence that any differences in the particulate samples generated for this study is purely related to the fuel.

4.2 Evaluation of Particulate Reactivity Differences

4.2.1 Temperature Programmed Oxidation

In order to determine the relative reactivity of the samples, Temperature Programmed Oxidation (TPO) experiments were carried out in the microreactor described in the previous chapter. Briefly, TPO experiments are done by running a temperature ramp from 323 to 923 K, with the sample exposed to 10% O_2 in Ar. A

second stage reactor containing a Pt/AlO_3 oxidation catalyst was used to assure complete conversion of the combustion products to CO_2 for analysis by mass spectrometry.

Comparison of the nascent TPOs is done by plotting μmoles CO_2 evolved normalized to mass of carbon recovered versus temperature in Kelvin in Figure 24. It is clear from this plot that B100 particulates are much more reactive than those from ULSD, with the peak rate of oxidation occurring approximately 60K earlier. B20 particulates are the next most reactive, surprisingly ULSD particulate was the next most reactive and particulates from B5 were the least reactive, requiring the highest temperature fully oxidize.

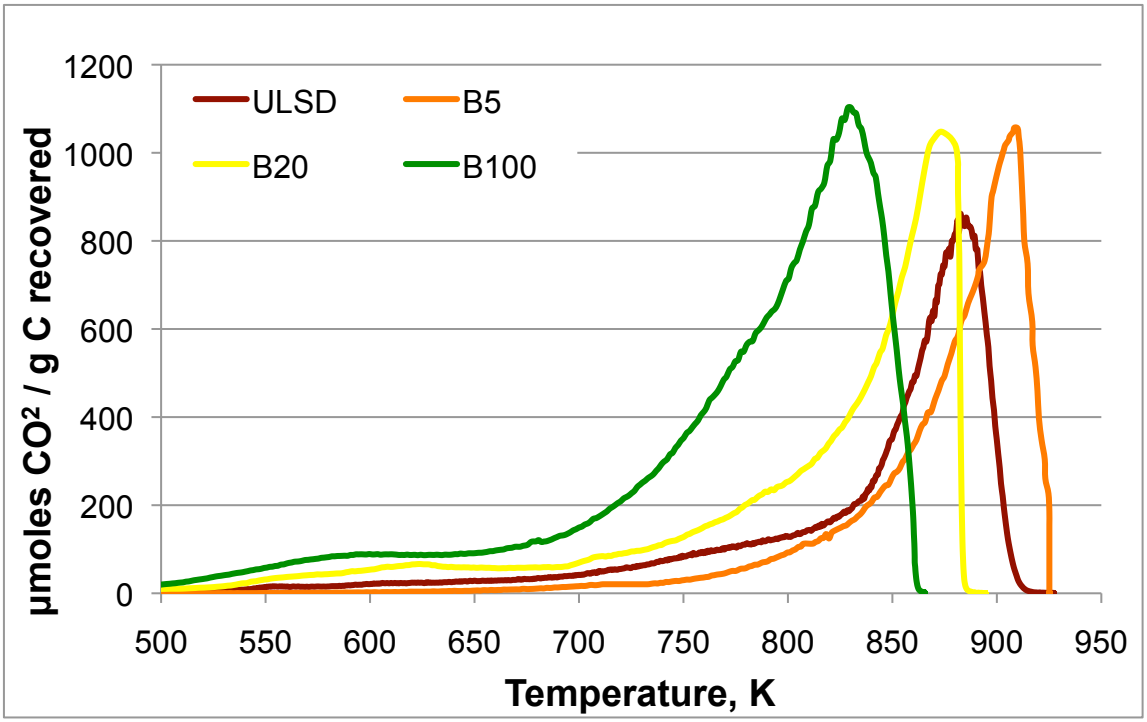

Figure 24 Comparison of nascent TPOs normalized to sample mass recovered. B100 particulate (green) are most reactive, followed by particulates from B20 (yellow), ULSD (red) and finally B5 (orange).

Another way to evaluate the relative reactivity of the samples is to compare the fraction carbon converted as a function of temperature, as seen in Figure 25. As before, the B100 particulates are the most reactive with oxidation reaching completion at the lowest temperature, 865K. B20 particulates are completely oxidized by 880K, ULSD particulates are fully oxidized by 905K and B5 particulate finally reach complete burnout during the hold at 923K, the highest temperature of the ramp, which is held for 30 minutes once reached.

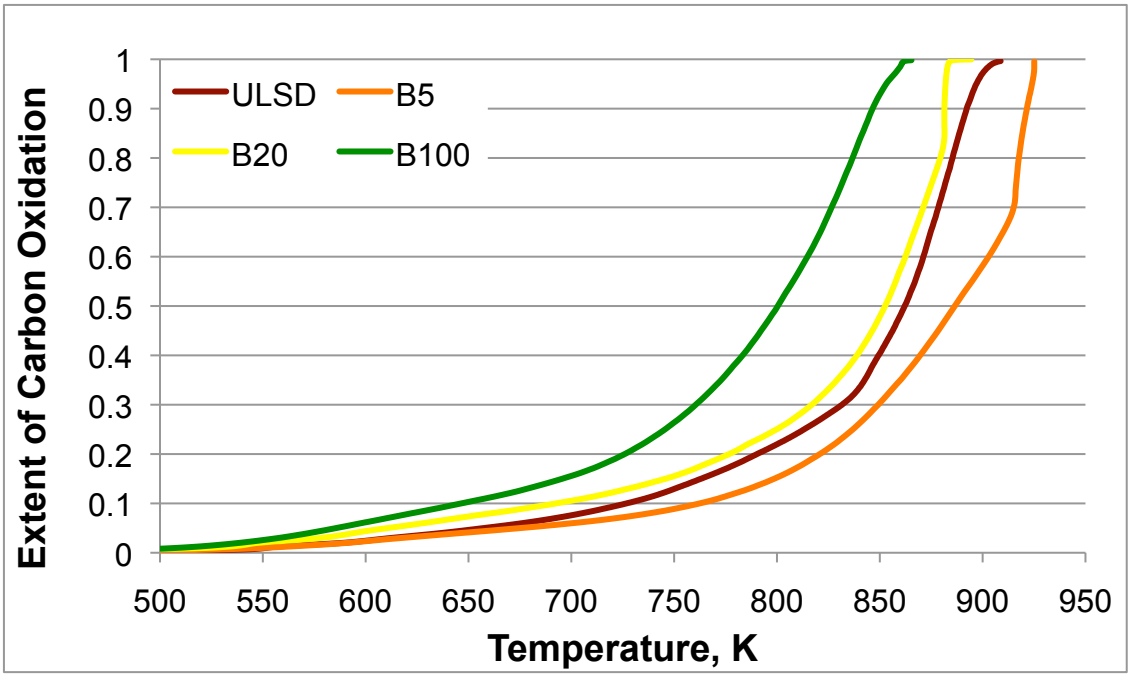

Figure 25 Extent of Reaction, or fraction carbon converted to CO_2, with Temperature (K). B100 particulate (green) reaches complete conversion at the lowest temperature, followed by particulates from B20 (yellow), ULSD (red) and finally B5 (orange).

There are clearly differences in the oxidative reactivity of the particulate samples, however, the cause of those differences has been a topic of debate in the literature. Diesel particulates are comprised of a fixed carbon structure with adsorbed mobile carbon, in the form of unburnt or partially burnt hydrocarbons from the fuel and lubricating oil. The differences in the reactivity of particulates from biodiesel and its blends has been suggested to be related to the adsorbed mobile fraction, or fuel oxygenates incorporated into the skeletal structure, or differences in arrangement of the

fixed carbon skeletal structure, known as the nanostructure [88]. To determine the source of the reactivity differences, the fixed and mobile fractions were investigated separately.

4.2.2 Temperature Programmed Desorption

To create devolatilized samples, Temperature Programmed Desorption (TPD) experiments were carried out in the microreactor. Briefly, TPD is done by running a temperature ramp from 323 to 923 K, flowing inert gas over the sample so as not to oxidize the sample, but just evaporate the volatiles. A second stage reactor containing a Pt/AlO_3 oxidation catalyst was used in conjunction with a makeup stream of O_2 to oxidize the volatiles removed to CO_2 for analysis by mass spectrometry.

The normalized TPD volatile evolution comparison is plotted in Figure 26 and volatile conversion (evaporation) with temperature is plotted in Figure 27. It is interesting to note that the normalized volatile evolution plot at maximum reaches just one tenth of the nascent, indicating that the volatile fraction is not the major component of the nascent particulate.

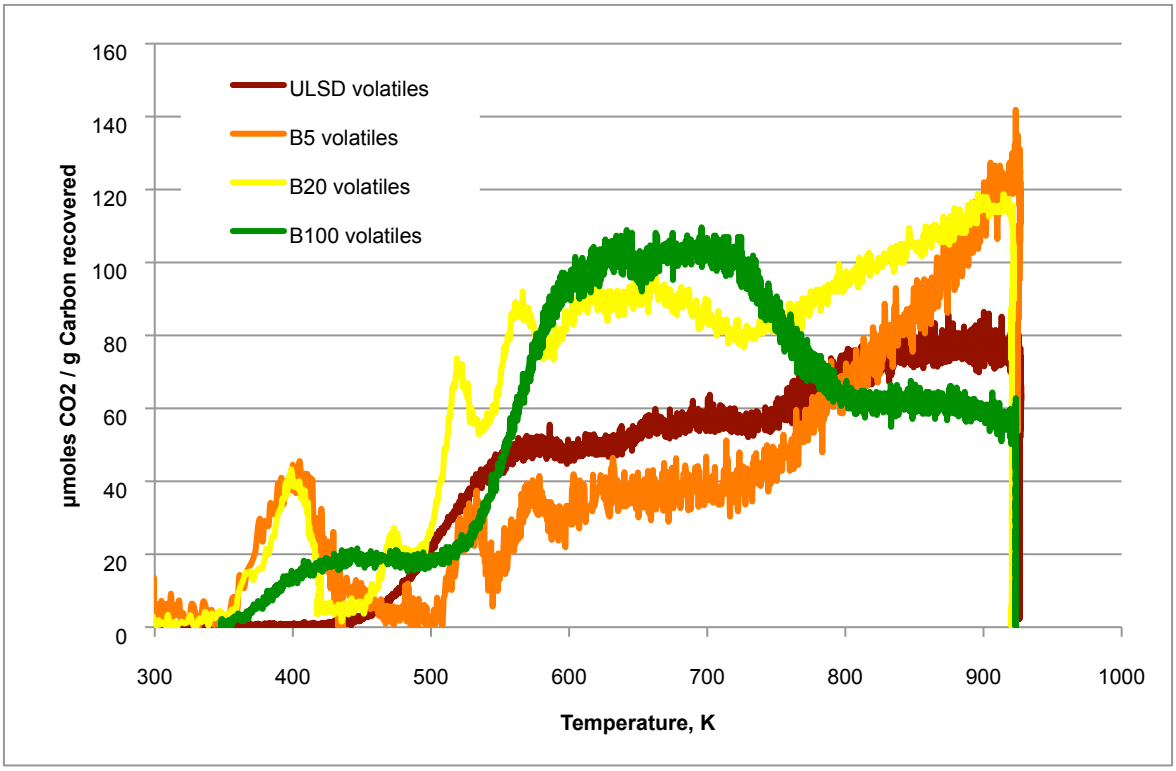

Figure 26 Comparison of normalized TPD plots for ULSD (red), B5 (orange), B20 (yellow) and B100 (green). Compared to the nascent carbon plot (Figure 24), the volatile profiles are rather similar and only one tenth the value of the nascent samples.

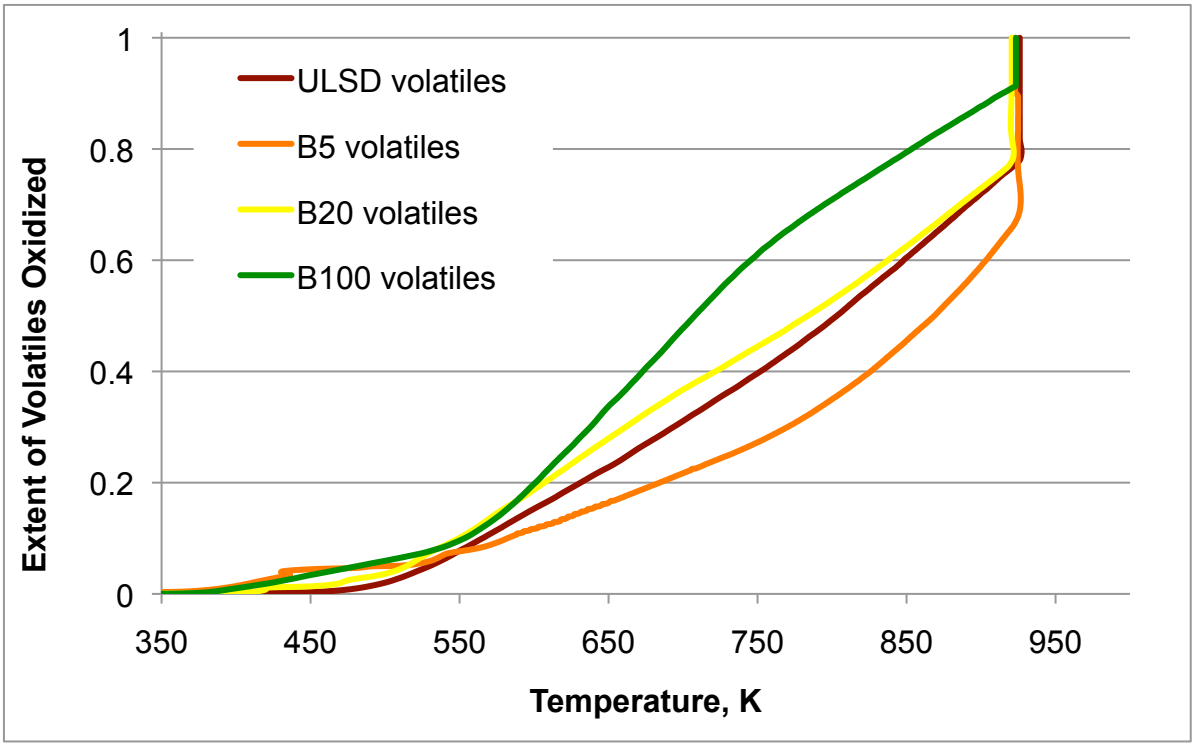

Figure 27 Extent of volatile oxidation (fraction volatile carbon oxidized) as a function of temperature for ULSD (red), B5 (orange), B20 (yellow) and B100 (green) particulate matter.

From these experiments, it was possible to determine the mobile carbon (MC) or volatile (VOF) fraction of the PM samples as shown in Figure 28. Increasing volatile content correlates with increasing biodiesel blend level, with the exception of the B5 blend level.

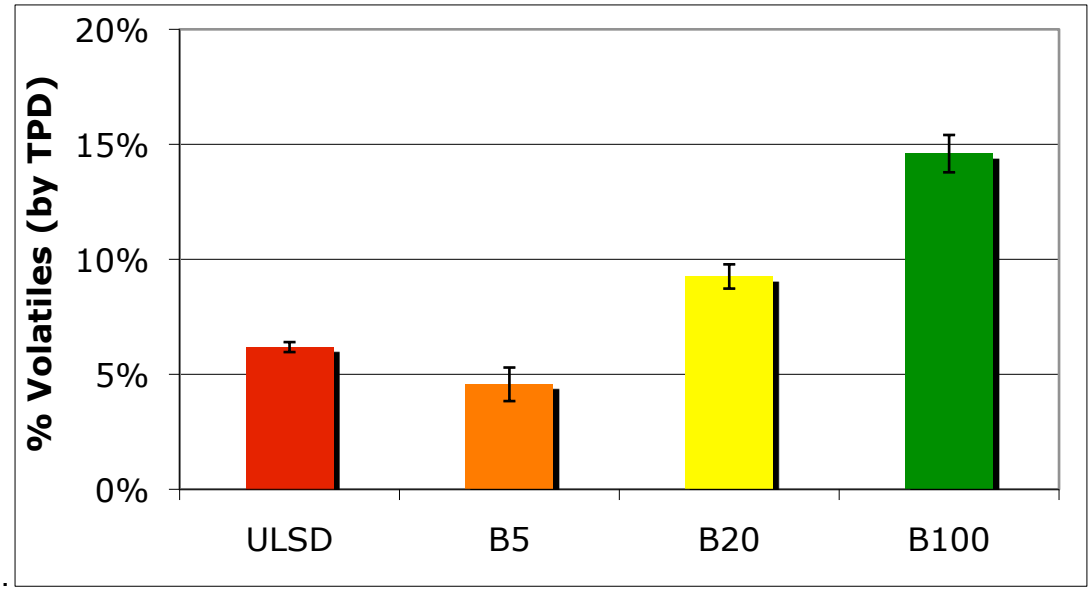

Figure 28 VOF percentage of PM with biodiesel blend level.

Figure 29 is the comparison of devolatilized fixed carbon TPOs, plotted in the same manner as the nascent samples in Figure 24. This plot shows that the difference between the samples is not merely an effect of the volatiles; however, the impact of the volatiles is seen in the temperature shift of the curves compared to the nascent samples plotted in Figure 24.

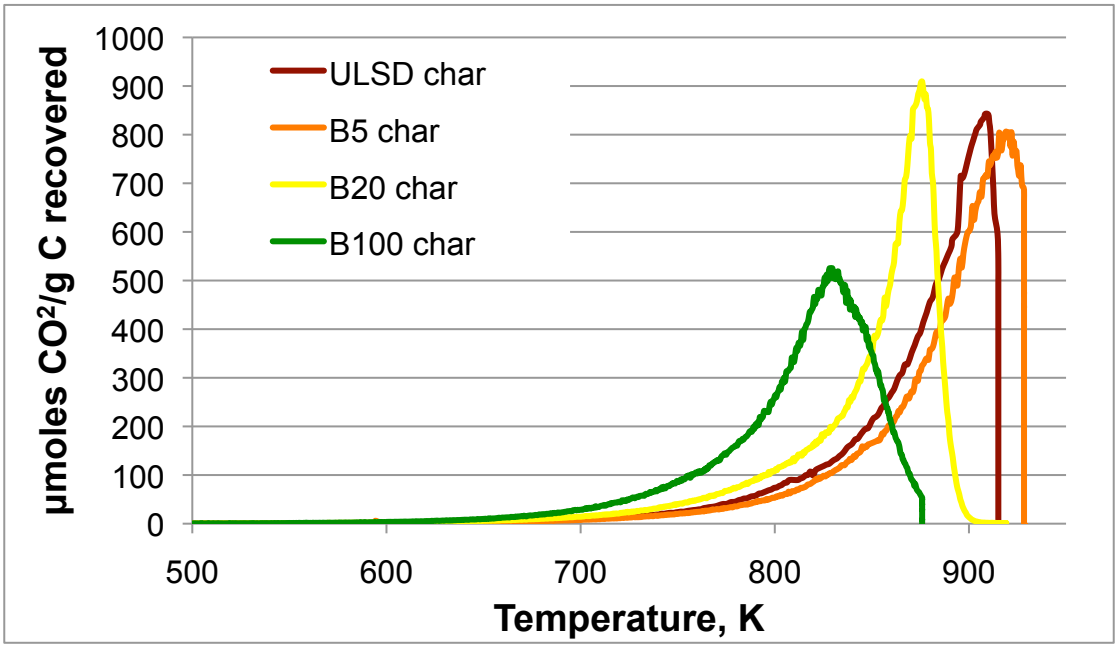

Figure 29 TPO profiles of devolatilized (fixed carbon) particulate samples.

In parallel to Figure 25, Figure 30 shows the fraction carbon converted with temperature for the devolatilized particulate samples. There is a 10K shift in the final burnout temperature for all of the samples, except for B5, which once again burns out once the temperature ramp has reached the 923K hold. The fixed carbon plots show that despite the removal of volatiles, the difference between samples persists, therefore, the reactivity differences from the biodiesel blends are not merely related to the mobile volatile content. Any oxygenates in the fixed carbon structure would also have been removed during the TPD, therefore the reactivity difference is also not due to oxygenates entrained in the carbon structure.

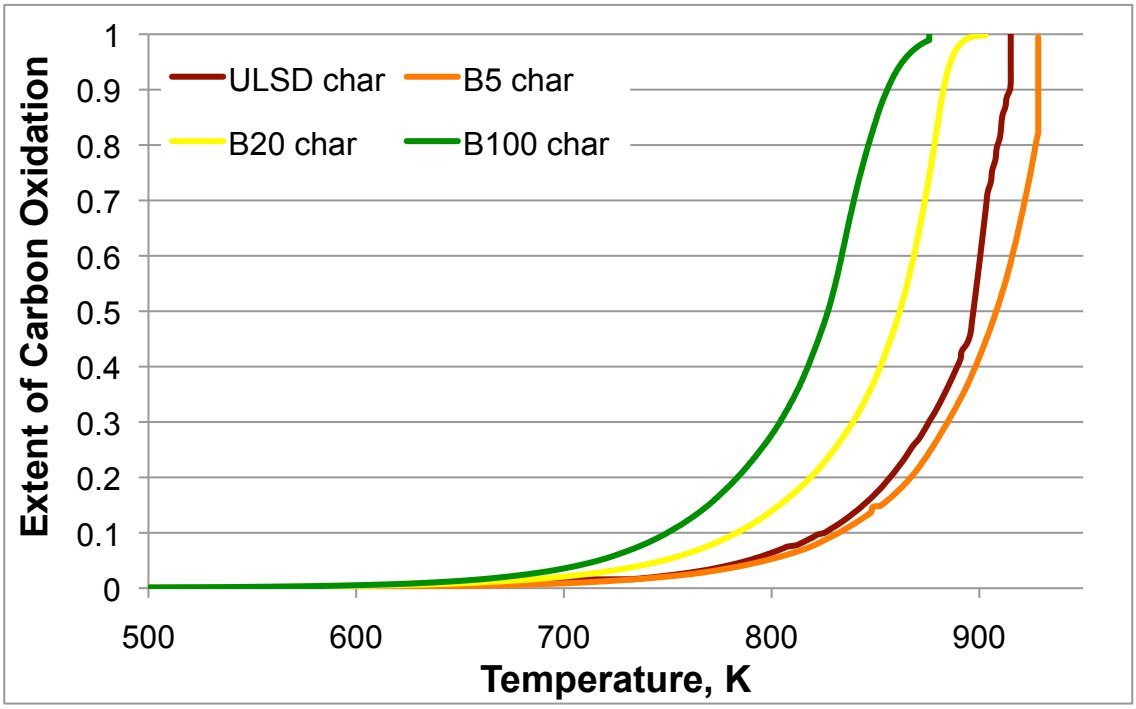

Figure 30 Extent of Reaction, or fraction fixed carbon converted to CO_2, with Temperature (K). B100 particulate (green) reaches complete conversion at the lowest temperature, followed by particulates from B20 (yellow), ULSD (red) and finally B5 (orange).

A more comprehensive way to demonstrate the impact of the volatiles is by considering a TPD, nascent TPO and fixed carbon TPO, corrected to carbon recovered on a single plot. This is done for ULSD in Figure 31 and B100 in Figure 32. For both fuels, the removal of the volatiles shifts the peak of the curve on the order of 10-15 degrees. These plots also show that the volatiles impact is predominantly at low temperature, and that the fixed carbon effect (as shown by the fixed carbon TPO plots, the black lines) is the dominant effect for the oxidation process. Therefore, in order to

describe the oxidation reaction rate for particulate, it is important to determine the fundamental oxidation kinetics of the fixed carbon portion; measuring the rate at multiple temperatures in order to calculate the activation energy does this.

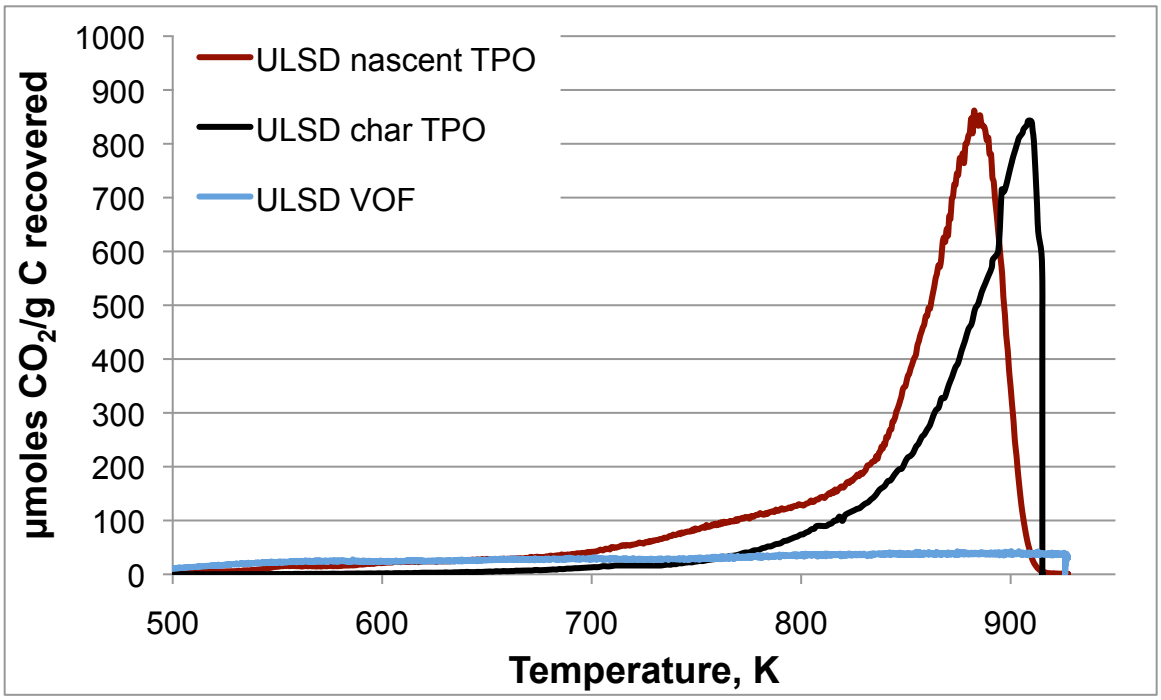

Figure 31 Comparison of TPD (volatiles, blue), nascent TPO (red) and fixed carbon TPO (black) for ULSD PM. This figure shows the relative impact of the fixed and volatile carbon on the oxidation of nascent ULSD particulate.

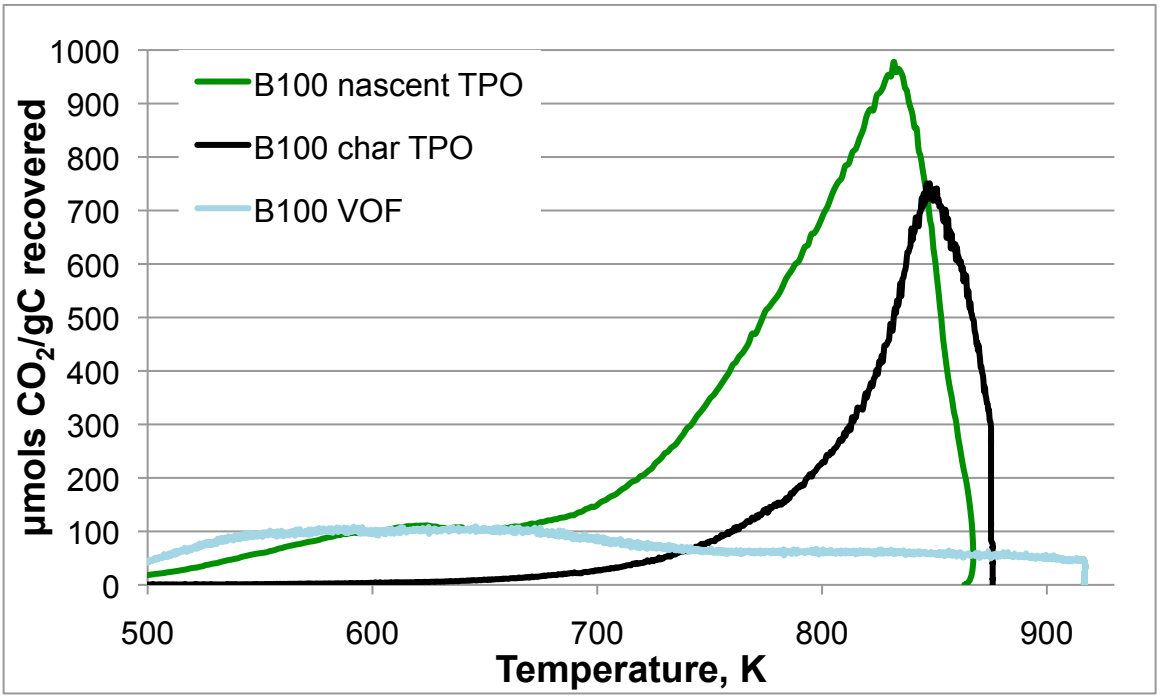

Figure 32 Comparison of TPD (volatiles, blue), nascent TPO and fixed carbon TPO for B100 PM. This figure shows the relative impact of the fixed and volatile carbon on the oxidation of nascent B100 particulate.

4.2.3 Determination of Elemental Carbon Reaction Kinetics

The ULSD and B100 PM fixed carbon samples were chosen as the focus of the work for kinetic parameter determination. Pulsed, isothermal, differential (less than 4% conversion per pulse) reactions were run in the microreactor in order to determine the Arrhenius parameters for the particulate samples. Based on their TPO profiles, ULSD particulate was studied between 723 and 873 K and B100 particulate was studied between 673 and 823 K.

The reactions were assumed to be first order in carbon and the O_2 concentration was held constant, therefore the rate equation

$$R = k[C]^1[O_2]^\beta \qquad \text{Equation 4-1}$$

becomes

$$R = k'[C] \qquad \text{Equation 4-2}$$

where *k'* is the effective rate constant equal to

$$k' = k[O_2]^{0.6} \qquad \text{Equation 4-3}$$

assuming the reaction order in oxygen to be 0.6, as reported by Yezerets [71]. Integrating the rate expression,

$$d[C]/dt = k'[C] \qquad \text{Equation 4-4}$$

gives

$$ln[C/C_o] = k'*t \qquad \text{Equation 4-5}$$

where $[C_o]$ is the initial concentration of carbon. Therefore, a linear plot of $\ln[C/C_o]$ against time for each isothermal experiment would confirm the first order assumption.

Figure 33 and Figure 34 show that for each isothermal, differentially pulsed experiment, the first order reaction plot was linear and k', the effective rate constant, can be determined from the slope of the line. Figure 35 shows the rate plots for ULSD and B100 as a function of temperature.

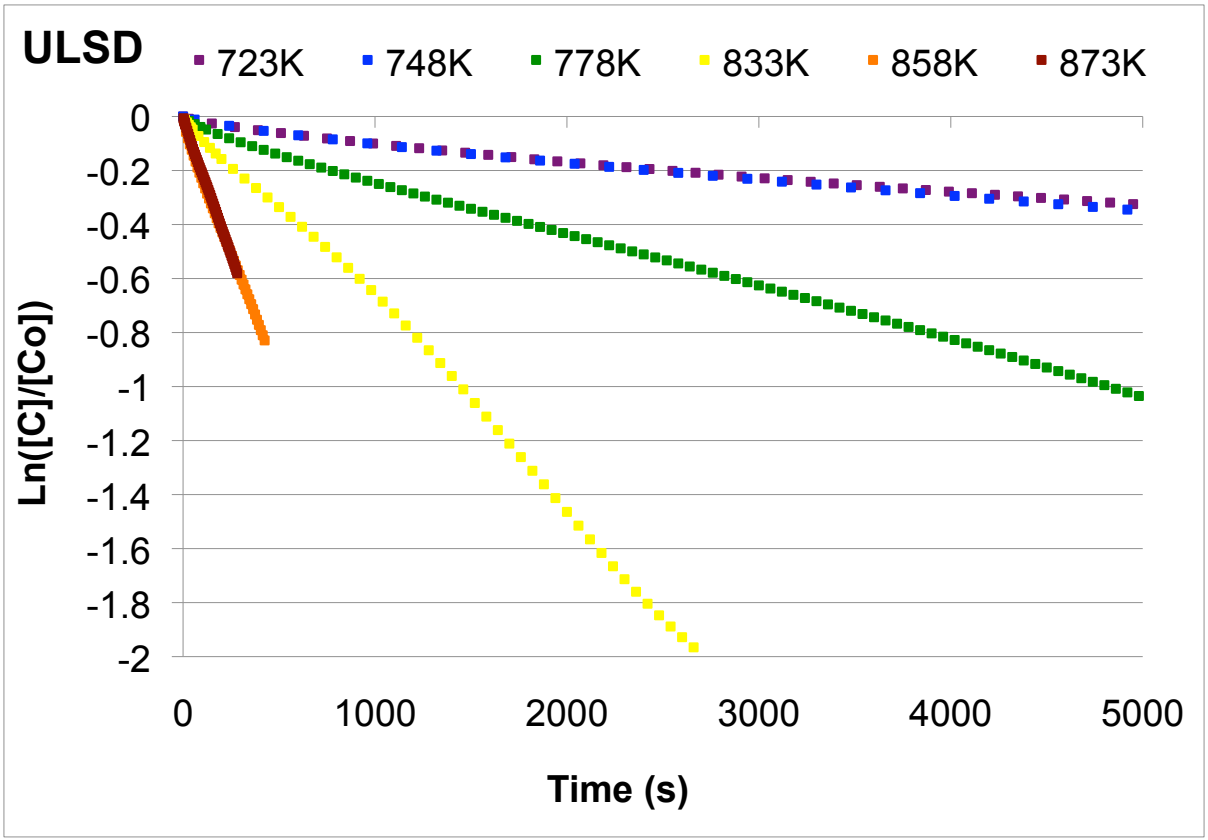

Figure 33 First order plots for ULSD particulate at 6 temperatures over the entire range of carbon conversion.

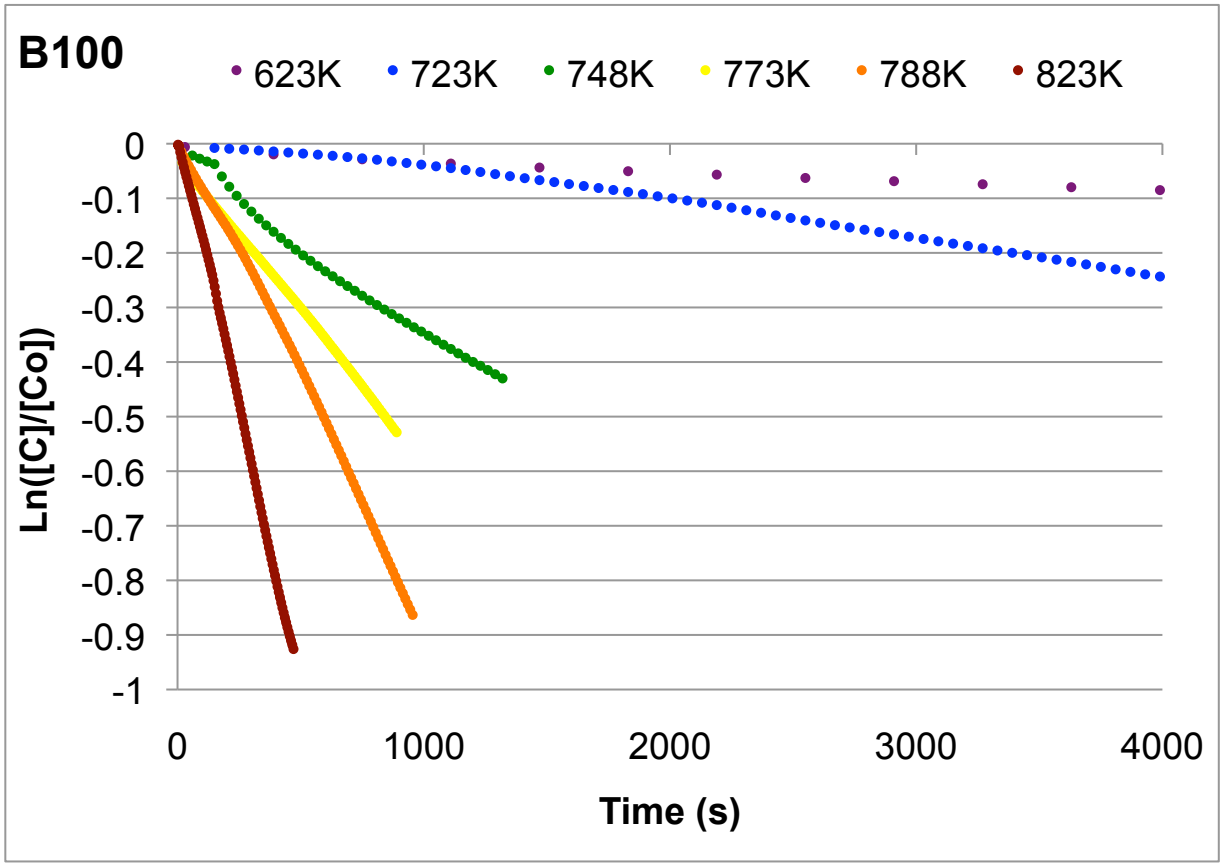

Figure 34 First order plots for B100 particulate at 6 temperatures over the entire range of carbon conversion.

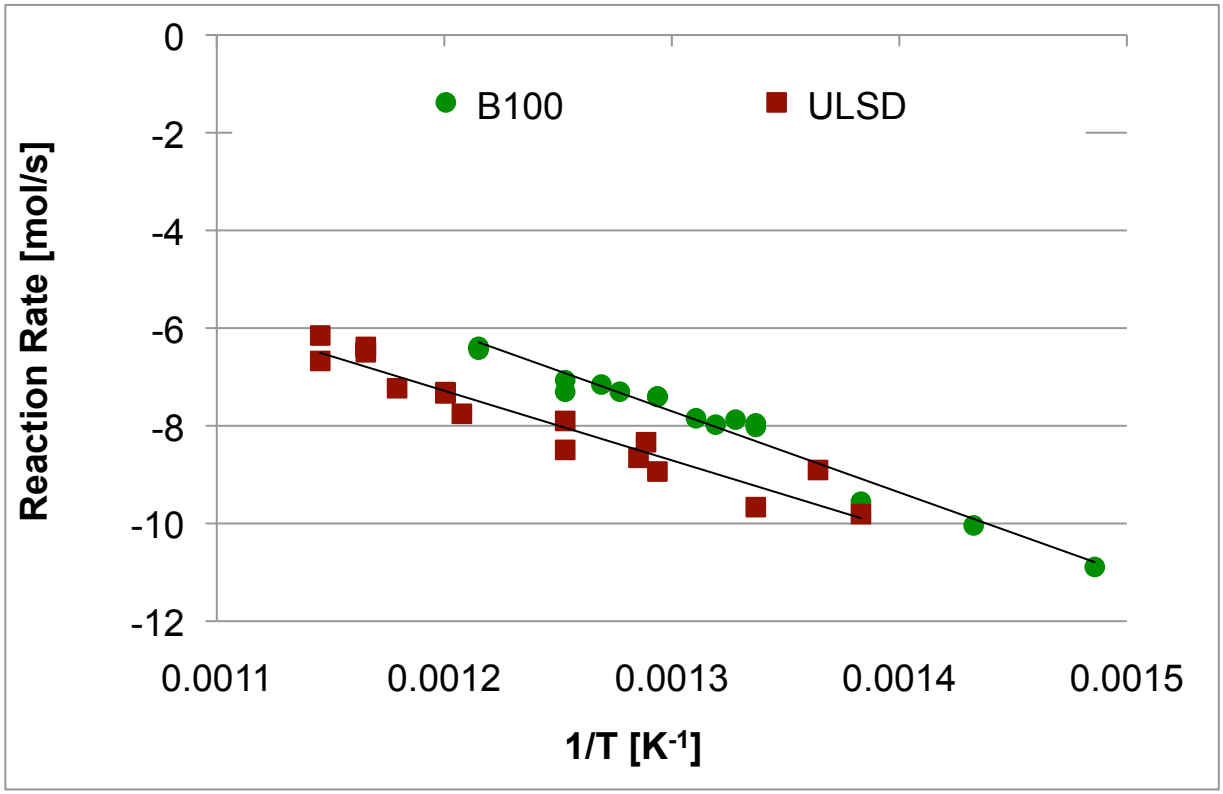

Figure 35 Rate plot for ULSD and B100 PM oxidation.

The temperature dependence of the reaction rate constants can be well described using the Arrhenius equation

$$k = A*exp(-E_A/RT) \qquad \text{Equation 4-6}$$

where A is the pre-exponential factor, E_A is the activation energy [J/mol], R is the universal gas constant [8.314 J/mol-K] and T is the temperature [K].

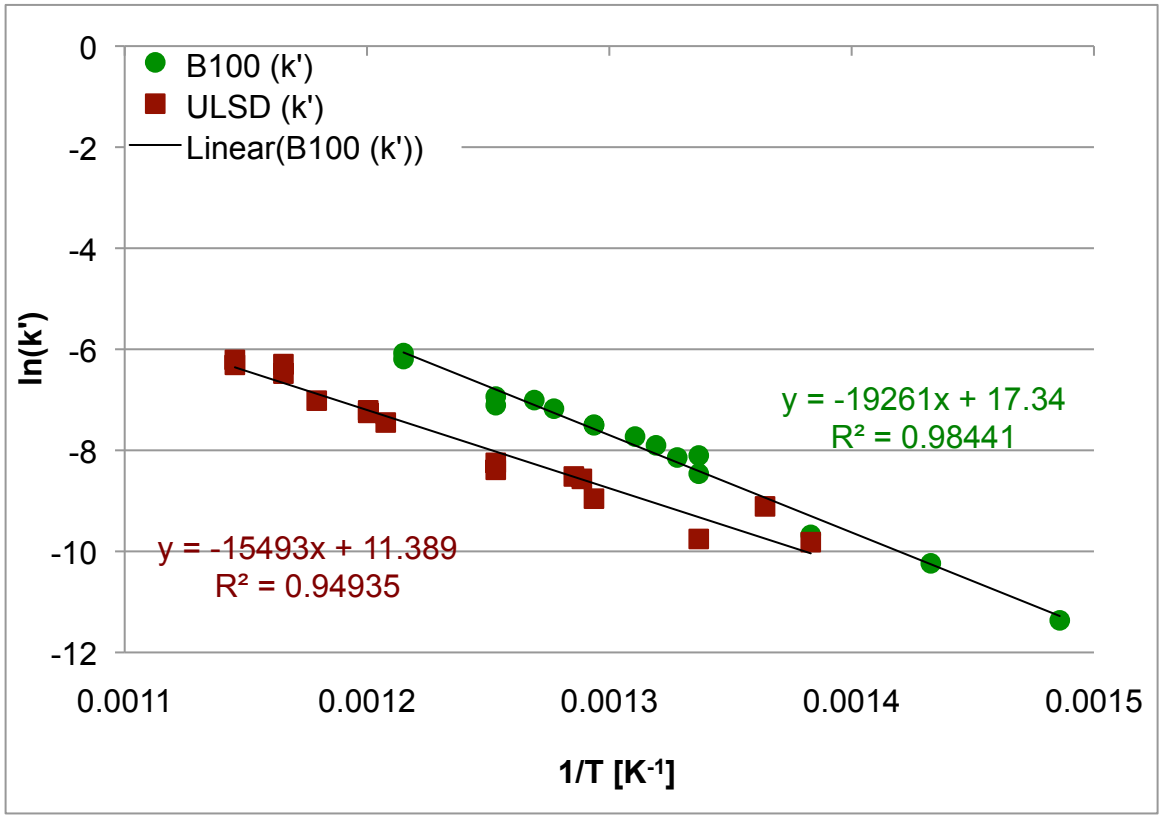

Figure 36 Arrhenius plot for ULSD and B100 over the entire range of burnout.

From the slopes of the Arrhenius plots, it can be determined that the activation energies of the ULSD and B100 PM are 128.8 (+/-6.5) kJ/mol and 160.1 (+/- 2.5) kJ/mol respectively. These activation energies are well within the range previously reported in the literature [70].

The difference in the activation energy for the two types of PM was interesting. We wondered if there was a physical reason for the difference and decided that for a heterogeneous reaction, it would be proper to consider the reaction rate in terms of the

surface area available for reaction. Therefore, the surface area with respect to extent of reaction, or burnout, was measured by BET.

4.2.4 BET Surface Area

Specific surface area was measured for nascent (n), devolatilized fixed carbon (c) and partially oxidized ULSD and B100 PM in the microreactor, using the 7-point flowing BET technique described in Chapter 3. Large gains in surface area were seen in both samples with devolatilization, as shown in Figure 37.

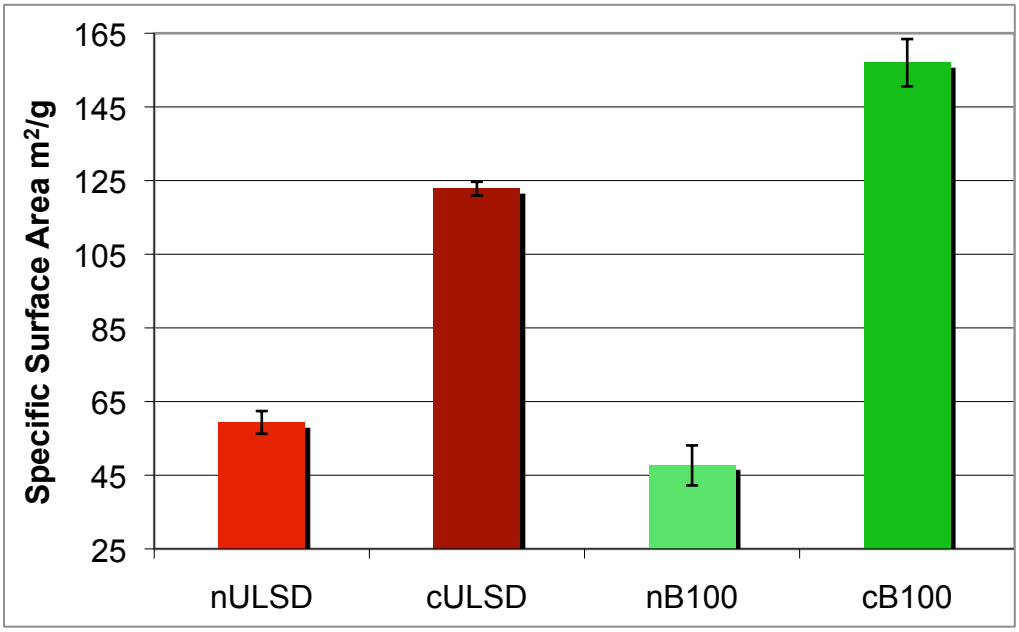

Figure 37 Specific surface area for nascent (n) and fixed carbon (c) samples.

Removing the volatiles allowed for large gains in the specific surface area for the ULSD (105% increase) and B100 (230% increase) particulates as compared to the

nascent samples. The relative difference in the specific surface area of the B100 and ULSD fixed carbon samples (B100 PM has 1.3x the surface area of ULSD PM) may correlate to the difference in apparent primary particle sizes, also a factor of 1.3x.

For a heterogeneous reaction, the surface area is a key parameter in the reaction, and may change as a function of the extent of reaction, therefore, the change in surface area with burnout was measured in Figure 38.

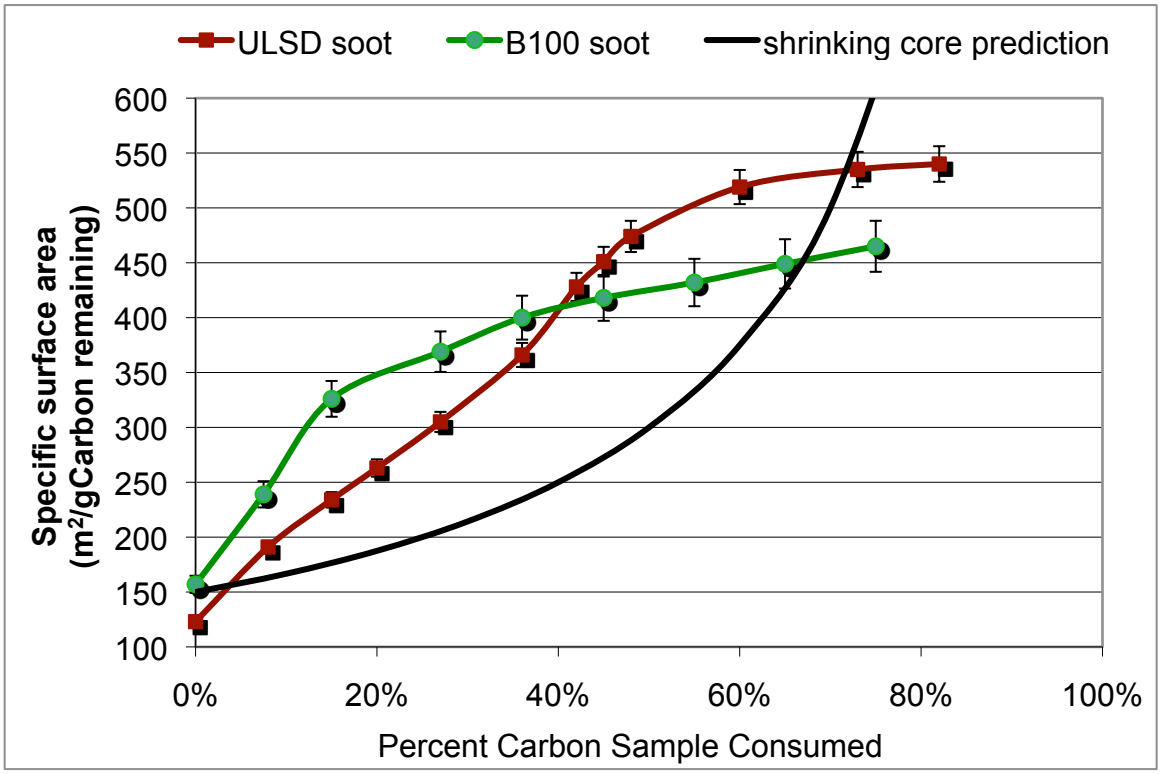

Figure 38 Specific surface area as a function of extent of reaction.

It appears that the initial stages of burnout increase the specific surface area of the particulate samples, perhaps by creating additional porosity in the samples, then

after approximately 40% burnout, the surface area begins to plateau. The shrinking core prediction:

$$SA = 3/r * V \qquad \text{Equation 4-7}$$

where SA is surface area in m^2, r is radius in m and V is volume in m^3, is plotted for comparison, and it is evident that neither the ULSD nor the B100 particulates follow a Zone I, or shrinking core, burnout trajectory. It is much more likely that the particles are experiencing Zone II burning, which includes both surface and pore oxidation, which seems reasonable given that the surface area for the PM samples is greater than that of surface-only burning.

Another way to look at the evolution of surface area with extent of reaction is to consider the total surface area (in m^2) for a sample (calculated for 1g of PM) as it burns out. This is plotted in Figure 39.

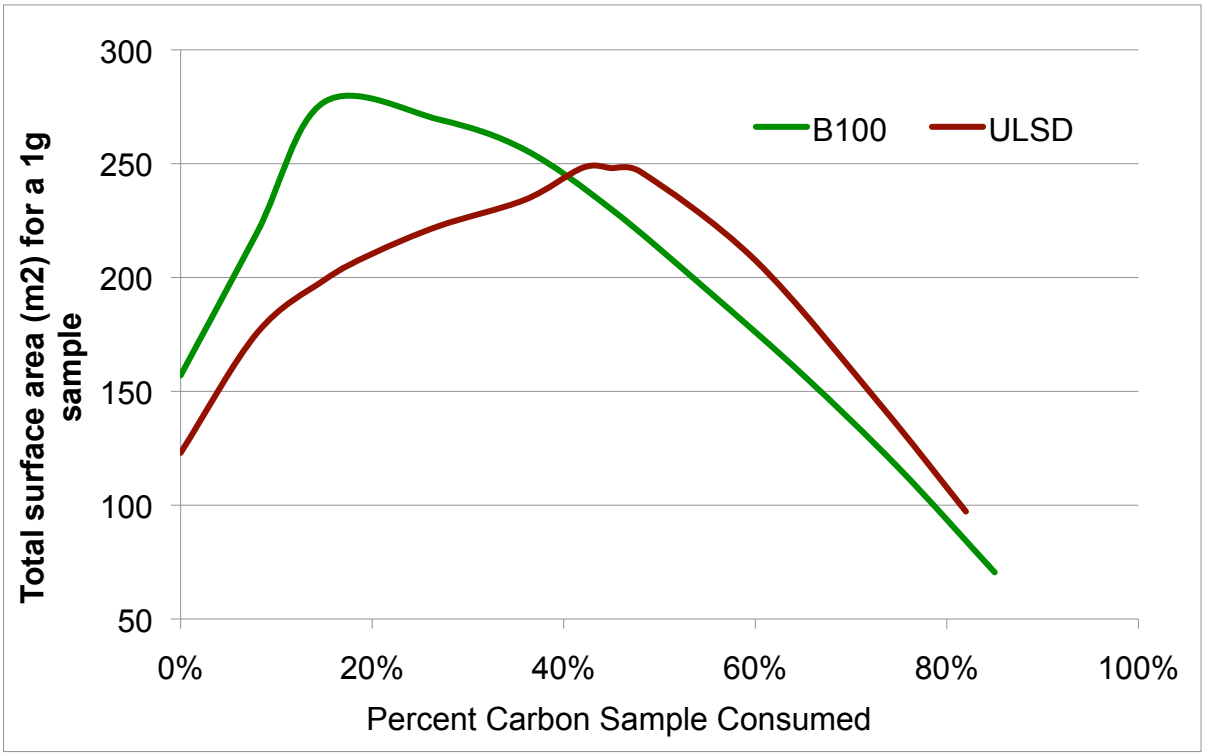

Figure 39 Calculated total surface area (m^2) for 1g samples of ULSD and B100 PM.

In this figure, it is clear that the B100 fixed carbon has substantially more surface area than the ULSD fixed carbon for the same extent of reaction, up to 40% carbon consumption. Past 40% conversion, the samples are quite similar, with ULSD PM having a slightly larger surface area. Polynomial fits of the surface area with extent of reaction curves are 3rd order for B100 and 2nd order for ULSD. To better understand the origin of the differences in surface area and sample reactivity, the elemental carbon skeleton was investigated by high-resolution transmission electron microscopy (HR-TEM).

4.2.5 Surface Area Normalizes Reaction Rates

In light of the surface area and reactivity differences between the samples, the reaction rates were normalized to the total surface area to normalize the samples, following the example of Smith [89] and Essenhigh [40]. The reaction rate was considered as

$$R = -d[C/A]/dt = k''[C] \qquad \text{Equation 4-8}$$

where k'' is the rate constant on an area basis [L/m^2-s]. The area-based rate constant is equivalent to the true rate constant based on

$$k'' = 1/A*k' = 1/A*k[O_2]^{\beta} \qquad \text{Equation 4-9}$$

using the Arrhenius relationship,

$$ln([C/C_o])-ln(A/A_o) = k''t \qquad \text{Equation 4-10}$$

where A is the total surface area at the present state of burnout and A_o is the total initial surface area. Figure 40 shows the surface area dependence of the reaction rate normalizes the oxidation behavior of the ULSD and B100 PM.

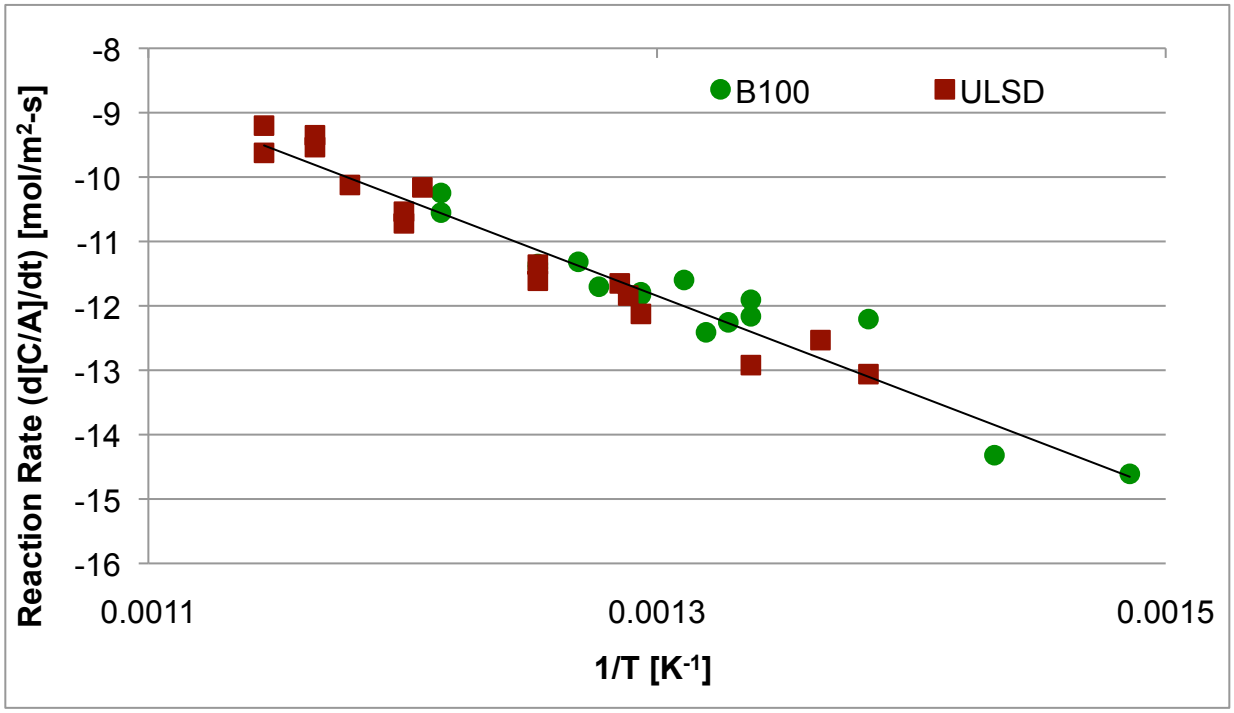

Figure 40 Surface area normalized reaction rates vs. 1/Temperature for ULSD and B100 PM.

The surface area normalized rates for fixed carbon oxidation were compared to data collected for coal [40, 89] char, another type of devolatilized fixed carbon in Figure 41, and was found to be in good agreement within the scatter of the data.

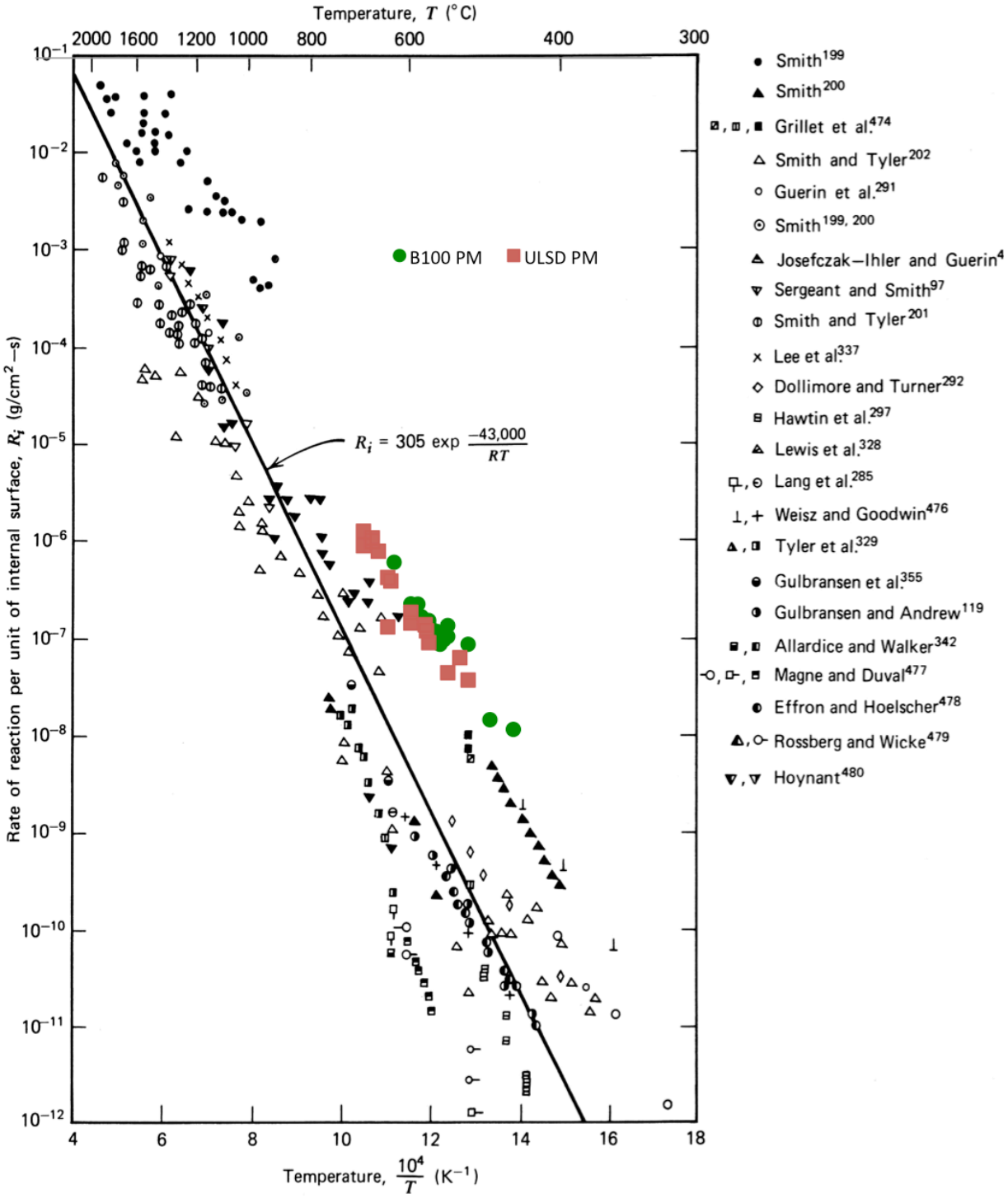

Figure 41 Reaction rate vs 10^4/T from [40], with fixed carbon data from ULSD and B100 overlaid.

With the surface area accounted for, the activation energy can be calculated from the plot of ln(k'') vs. 1/T, shown in Figure 42, from which it can be seen that the lines are parallel (have the same slope) and there is no longer a difference in the activation energy, now calculated to be 112.5 (+/- 5.8) kJ/mol for the fixed carbon.

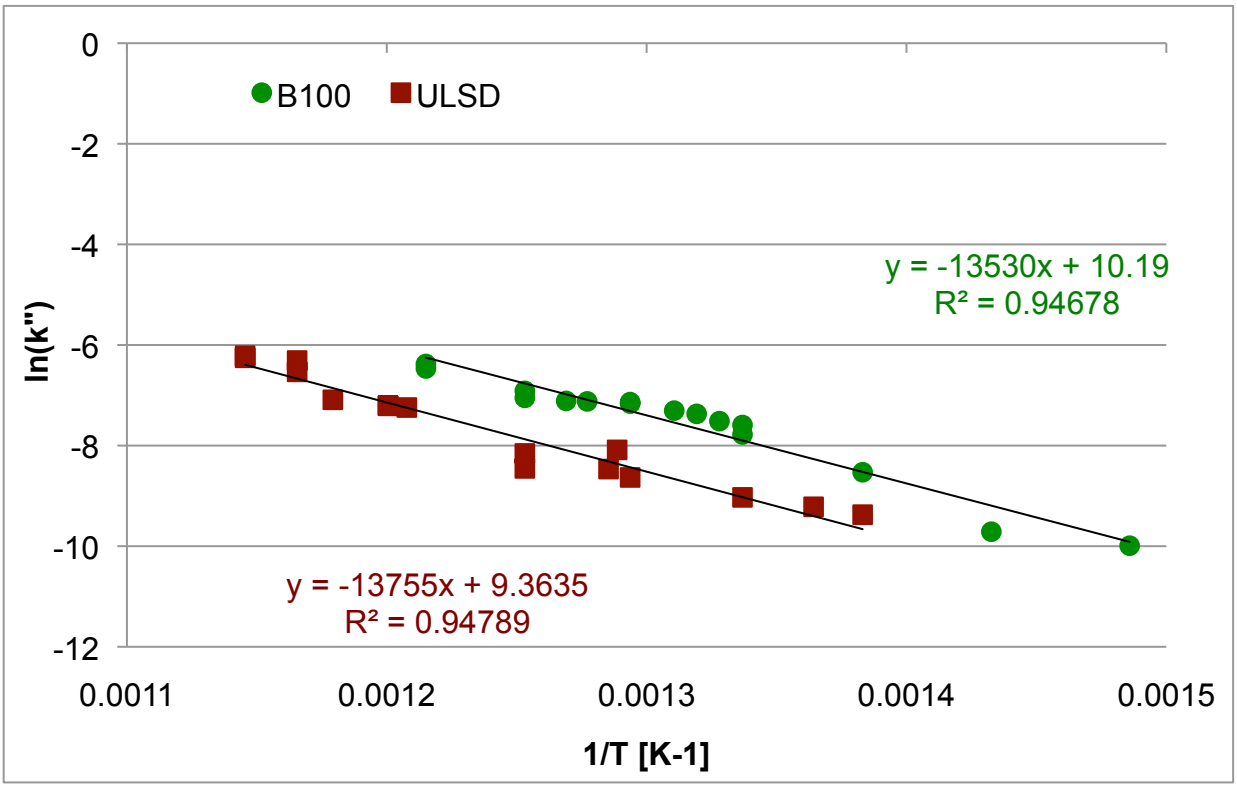

Figure 42 Arrhenius plot of ln(area-dependent rate constant) vs. 1/T.

The dependence of the reaction rate on surface area raised questions as to the source of the differences in the fixed carbon structure, or nanostructure of the particulate.

4.2.6 Investigation of the EC Nanostructure

Carbon nanostructure, the curvature and orientation of the molecular layers, has been related to oxidative reactivity; carbon that is graphitic in nature has planar, organized layers and has higher activation energy compared to carbon with curved or disorganized layers [23, 25, 88, 90]. Simple oxygenated fuels, such as ethanol, have been shown to produce distinctly different nanostructures with fullerenic character as compared to hydrocarbon fuels pyrolyzed under the same conditions [23, 91]. Vander Wal and Mueller investigated the effects of neat oxygenated fuels, and observed particulates with less graphitic structure and correspondingly higher reactivity as compared to conventional hydrocarbon particulates [91].

In this study, we had the opportunity to investigate the impact of oxygenated fuels at intermediate blend levels (shown in the Appendix), as well as neat B100 and compare them to ULSD particulate samples. Particulates were examined using HR-TEM to investigate the elemental carbon nanostructure, as described in Chapter 3. Briefly, carbon lamella, are the graphene segments that make up the particulate elemental carbon skeletal structure. In fringe analysis, the length of the segments is measured. Dr. Randy Vander Wal at the NASA-Glenn Research Center did microscopy and fringe analysis on the PM samples.

4.2.6.1 Unburnt Samples

Conventional ULSD fuel produced particulates, shown in Figure 43, with well-defined lamella, or layers of carbon, that were concentrically oriented. The

nanostructure lacked any evidence of fullerenic shells and is consistent with previously published data. . Primary particles are on the order of 33 μm in diameter.

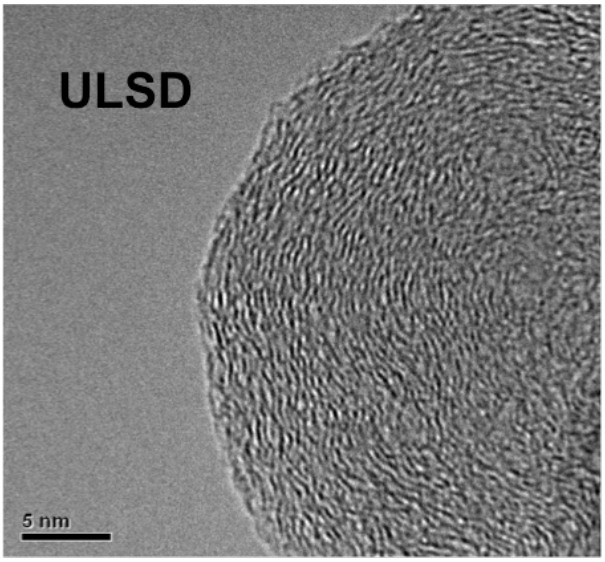

Figure 43 HR-TEM image of ULSD PM.

Particulates from neat B100, shown in Figure 44, lack any long-range order or fullerenic nanostructure. The lamella are very short, bordering on amorphous (as opposed to graphitic) in character, randomly distributed with no apparent stacking order, leading to more spacing between the lamella. Edge site carbons would likely be more accessible in such an open structure. Primary particles are on the order of 31 μm in diameter.

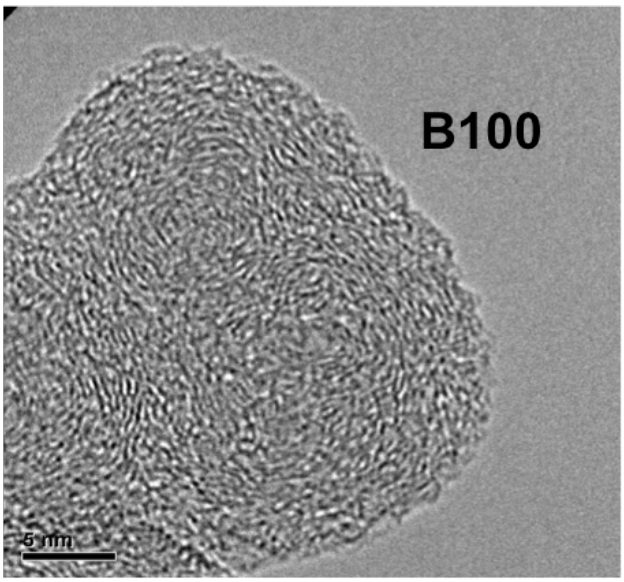

Figure 44 HR-TEM image of B100 PM.

The HR-TEM images show that the character of the particulate varies with biodiesel blend level. With a small amount of oxygenated fuel, we see disruption in the particulate nanostructure and evidence of fullerenes.

HR-TEM images are useful for qualitative comparisons between the particulate samples, however, to make statistical comparisons, quantitation by fringe analysis is required. Briefly, fringe analysis is performed by translating the TEM image into a skeletal drawing, as shown in Figures 3-4 and 3-5, which can then be analyzed by software. Lamella length is used to reflect the different ratio of edge to basal plane sites; the shorter the lamella, the more edge sites are accessible and the more reactive a sample is likely to be. The results of this comparison are shown in Figure 45.

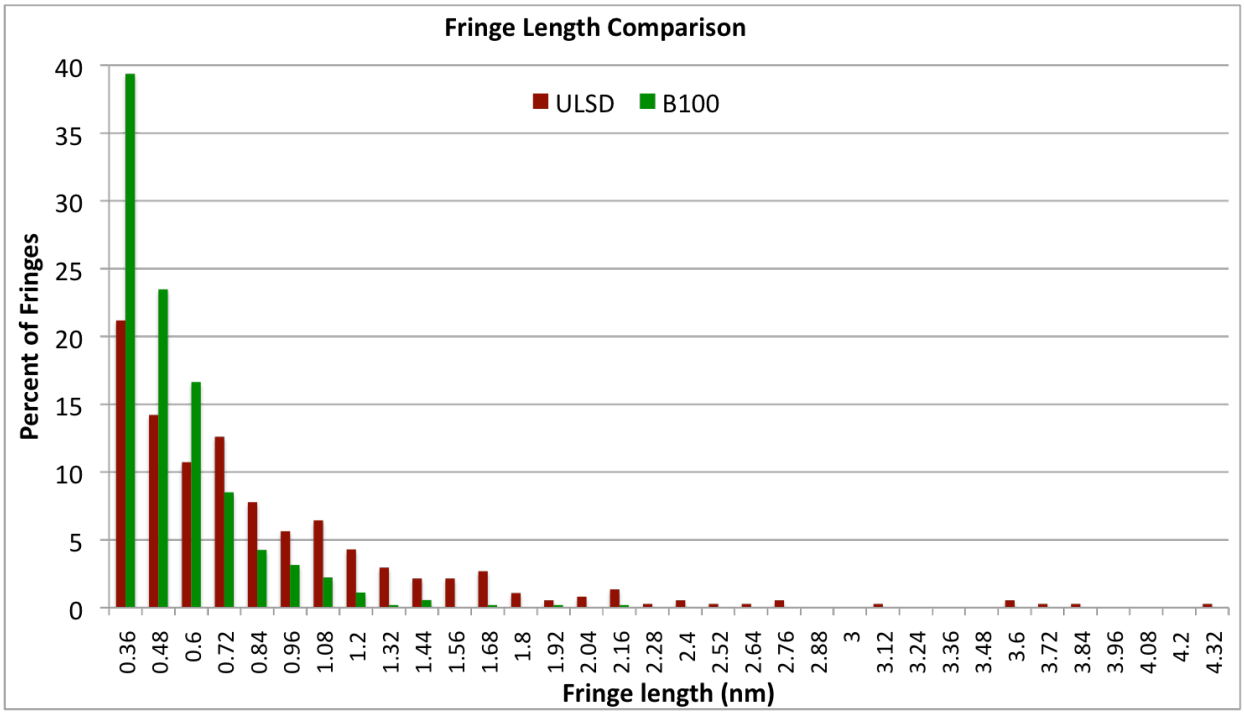

Figure 45 Fringe length comparison for ULSD and B100 PM.

The figure demonstrates that ULSD particulates have a wider range of lamella lengths that the B100 PM, from 0.36 to 4.32 nm. The B100 PM has a much higher (double) percentage of very short lamella and a range from 0.36 to 2.16nm, with the majority of the distribution between 0.36 and 0.6 nm. The shorter lamella in the B100 PM indicates that this sample would have more edge site carbons available for oxidation as compared to the ULSD PM.

The initial surface area differences between the samples can be related to the initial nanostructure; the more open nature of the B100 particulate and its larger edge to basal carbon ratio provides an explanation for the greater surface area. However, the surface area advantage of the B100 PM seems to be lost around 40% oxidation. We

were interested in how the nanostructure changes with oxidation might help to explain that.

4.2.6.2 Partially Oxidized Samples

ULSD and B100 PM samples were oxidized to approximately 50% burnout in the microreactor, then sent out for HR-TEM to evaluate the changes to the nanostructure. Figure 46 and Figure 47 are the HR-TEM images of the partially oxidized samples. The arrows point to areas of golf ball-like dimples, indicative of large pore formation.

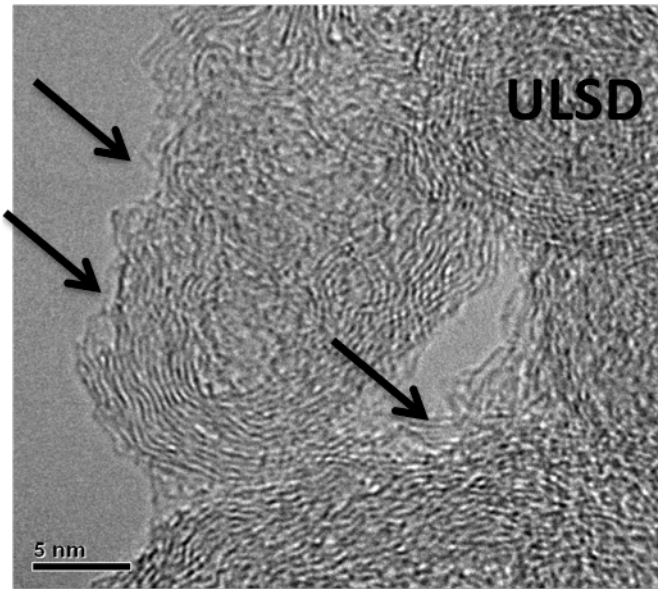

Figure 46 HR-TEM image of partially oxidized ULSD PM.

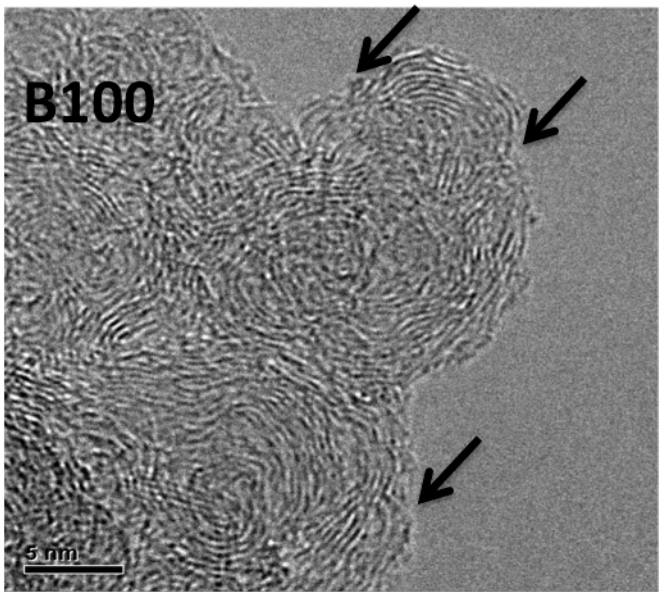

Figure 47 HR-TEM image of partially oxidized B100 PM.

Interestingly, the average primary particle diameters have only slightly changed as compared to the unburned samples, though the change in measured particulate diameter is statistically significant, meaning that the change is greater than the error bars on the averages. Specifically, ULSD particulates changed from 33 to 30 μm in diameter and B100 particulates changed from 31 to 29 μm in diameter. This observation validates that the particulates are not undergoing a shrinking core type burnout.

Fringe analysis of the partially oxidized samples shows that the lamella lengths of the two samples, which were initially very different (average 0.84 nm for ULSD vs. average 0.52 nm for B100) have become very similar at approximately average 0.2 nm, shown in Figure 45. This seems to support the similarity in surface area that develops as the particulate samples are oxidized past 40%.

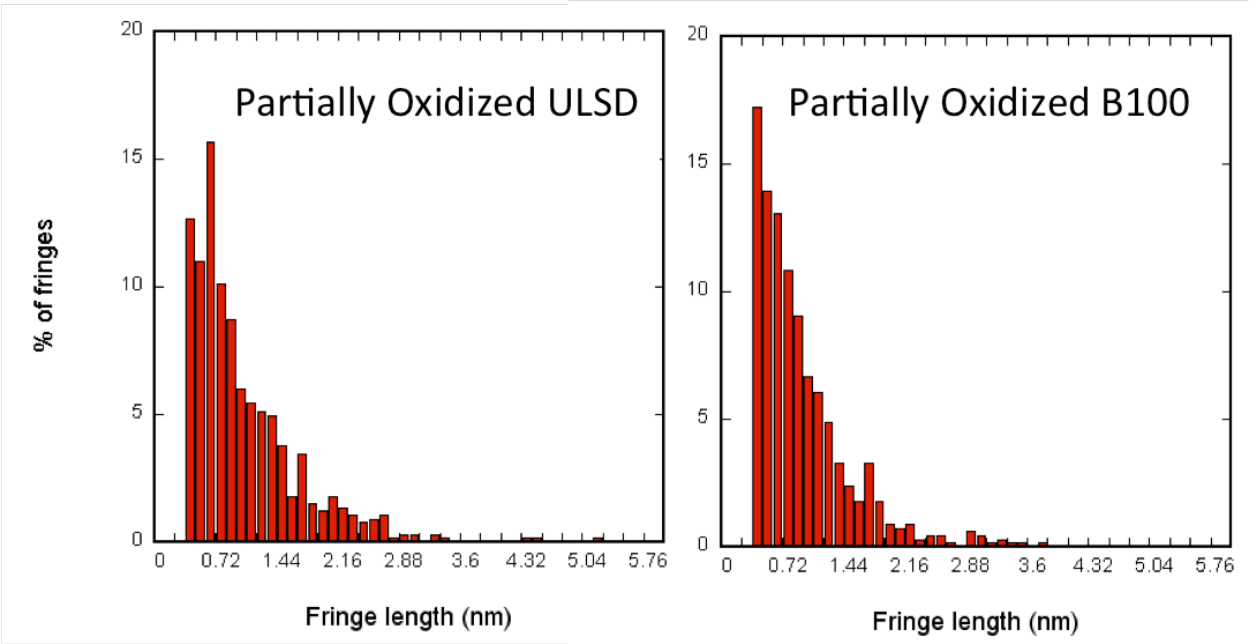

Figure 48 Fringe length comparison for partially oxidized (extent of reaction = 0.5) samples of ULSD and B100 particulates. The differences in the lamella length profiles of the nascent samples (shown in Figure 45) are no longer present in the samples that have been partially oxidized.

The nanostructure of the unburned and partially oxidized fixed carbon samples, along with the surface area measurements with extent of reaction, seems to explain the changes in the fixed carbon fraction of the particulate samples that are responsible for the differences in reactivity. However, although the fixed carbon fraction is the major component of the PM, the mobile fraction must also be considered for describing the reactivity of the nascent samples.

4.3 Chemical Speciation

4.3.1 Parent Fuels

Since the mobile fraction of diesel particulate comes from unburned and partially burned components of the fuel, the ULSD (Figure 49) and B100 (Figure 50) fuels were analyzed by GCMS for comparison of organic species present.

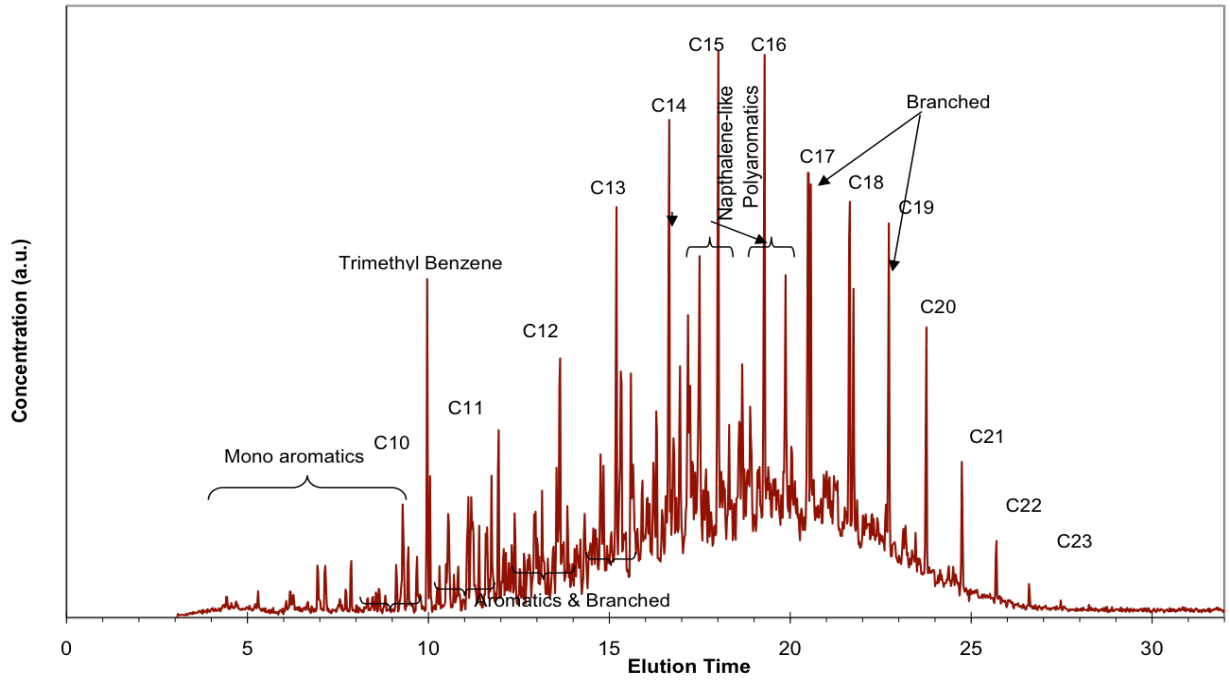

Figure 49 GCMS Trace of 2007 ULSD Certification Fuel. Large peaks are straight chain alkanes, baseline shift between 15 and 25 minutes is indicative of alkenes. Aromatics are labeled on the plot.

The ULSD fuel has a broad hydrocarbon envelope between C8 and C23, biased towards the lighter HCs. The large peaks represent straight chain alkanes and the

smaller peaks are representative of olefins. The fuel contains branches alkenes and aromatics, with a significant amount of naphthalene-like compounds.

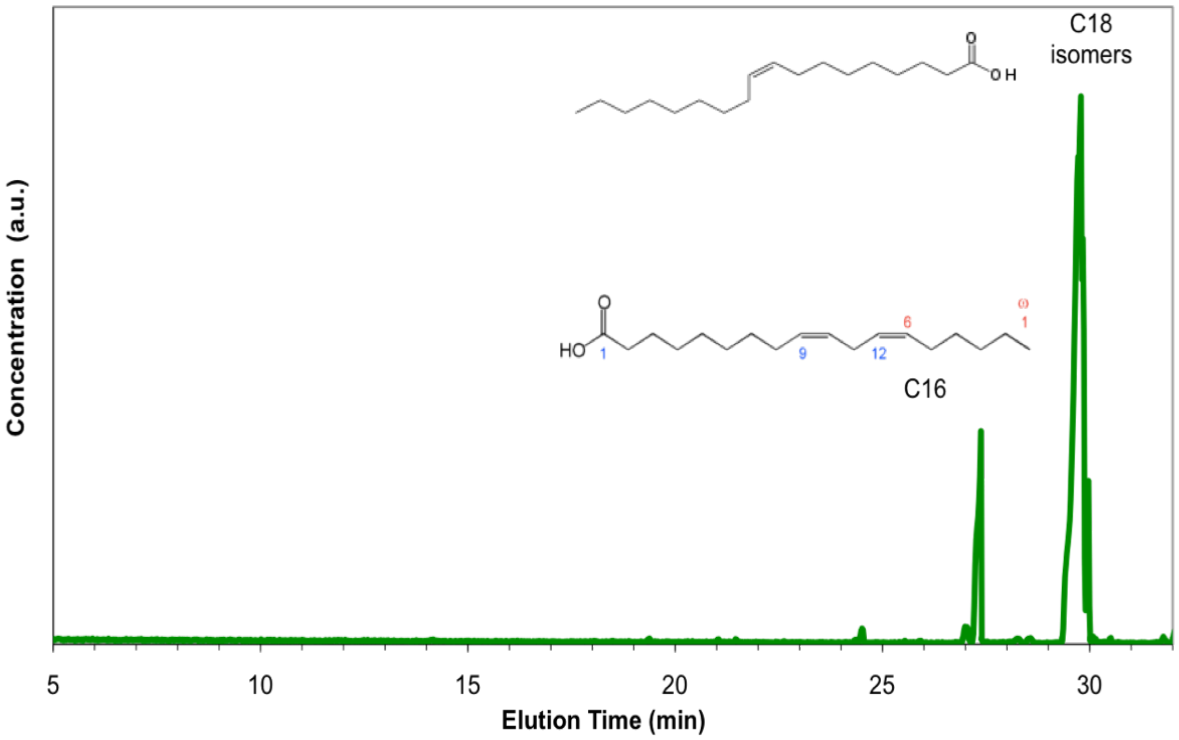

Figure 50 GCMS Trace of Soy Methyl Ester B100 Fuel.

In comparison to ULSD, the B100 fuel profile is very simple. The fuel is comprised of just three methyl esters that elute at C24 and C25 equivalents, one C16 and two C18 isomers. There is no discernable alkane, olefin or aromatic content in the fuel.

Soluble organic species in the particulate extracts were individually identified by GCMS quantification, then grouped into polynuclear aromatic (PAH), methyl-ester,

olefin and paraffin categories for comparison, as seen in the following figures. Additional discussion of the partitioning of the organic compounds to the gas or solid phase can be found in the Appendix. Generally, aromatics decreased with increasing biofuel blend level, olefins had very little presence in the solid phase particulates, appearing in less than 5% of the extract, and as expected, the paraffin fraction of the SOF decreased as the methyl ester fraction increased with biodiesel blend level.

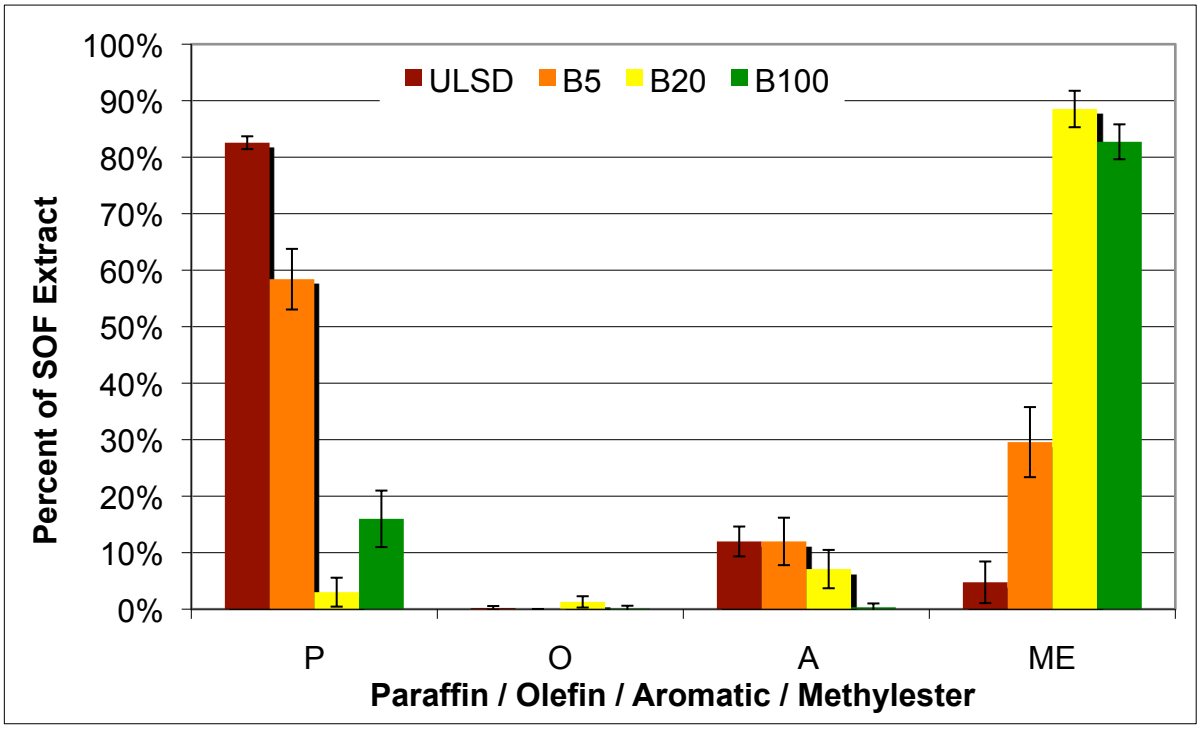

Figure 51 Speciation of SOF with biodiesel blend level.

Unexpectedly, the level of methyl ester in the SOF dramatically increased with only 5% volumetric addition of biofuel, indicating that the methyl esters survived combustion in a greater fraction than they appear in the fuel. We speculate that the

small level of methyl ester contamination seen in the ULSD samples is likely due to methyl esters previously deposited in the system. To minimize contamination, the dilution tunnel was run at elevated temperatures with increased dilution air overnight between samples, however, the methyl esters background never fully disappeared.

To determine the correlation between volatile species and oxidative advantage, the T10, temperature at which 10% of the sample has been oxidized, temperatures were compared for the nascent and devolatilized fixed carbon samples. Although a strong correlation for temperature reduction with percent VOF (as measured by TPD) was discovered, Figure 52, there was no apparent correlation with speciation, Figure 53. Therefore, it was determined that the amount of volatiles on the particulate matters, while the specific chemical nature of the volatiles did not. More detail on the chemical speciation of the organic fraction with biofuel blend level and sample collection location can be found in the Appendix.

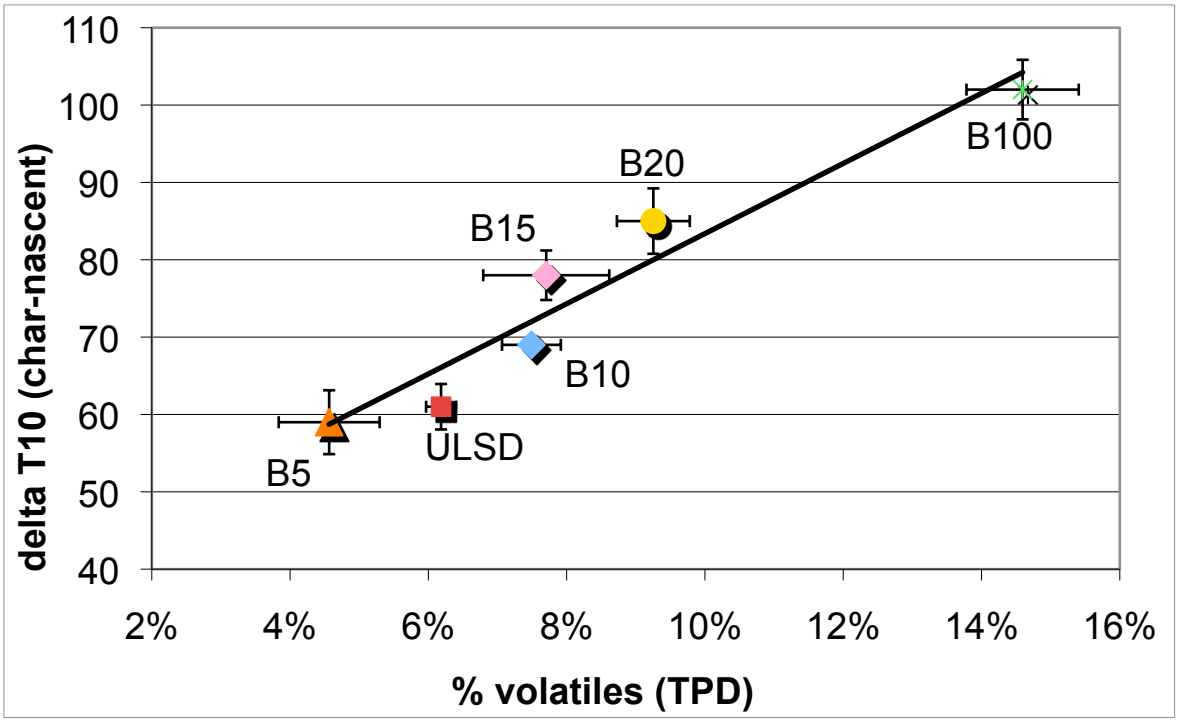

Figure 52 Change in T10 with Percent VOF.

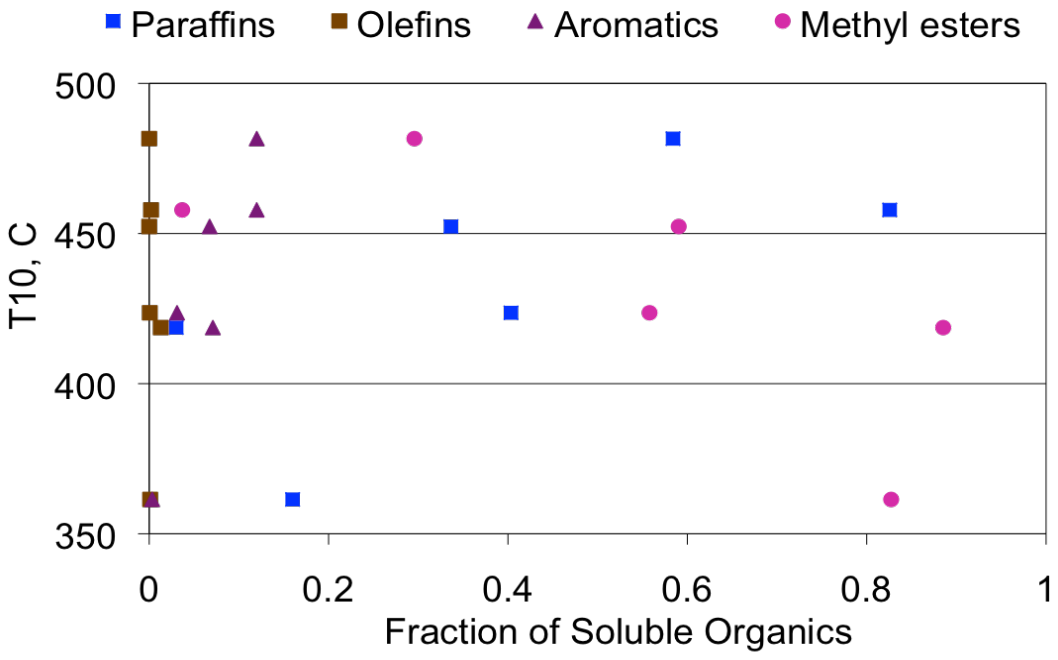

Figure 53 Comparison of T10 with Organic Species.

4.4 Discussion

The kinetic parameters determined for the ULSD and B100 particulate samples were compared to the physical and chemical characterization data in order to determine which factors have the greatest impact on the oxidation kinetics. The fixed carbon portion of the particulate was deemed to be the largest factor in describing the oxidation kinetics. In particular, it was found that the surface area available for reaction, which was found to be fuel source dependent, was an important factor in normalizing the oxidation rates of the ULSD and B100 particulate. In contrast, the mobile fraction of the particulate was found to have relatively little impact on the oxidation rate. Only the amount of volatiles present had any correlation to the shift in the oxidation profile that occurs between the nascent and devolatilized fixed carbon, independent of chemical species.

In the next chapter, a kinetic model for particulate oxidation is proposed that accounts for these findings.

5 Model Development & Validation

For many years, engine models have played an important role in the engine development process. As emissions standards became more stringent, engine manufacturers also came to rely upon models to predict exhaust gas compositions and DPF aftertreatment models to predict the emissions performance of the engine-aftertreatment system. Unfortunately, less attention was devoted to the key aspect underlying DPF models – regeneration, or oxidation kinetics. DPF models often empirically fit a simple regeneration model to match experimental data, instead of using fundamental kinetic models that describe particulate oxidation rates as a function of exhaust temperature. Improving upon the sub-model for particulate oxidation kinetics will increase the overall system model accuracy.

5.1 Previously Existing Kinetic Models for Particulate Oxidation

The literature is rich with Arrhenius-type kinetic models for carbon, coal and diesel particulate oxidation. However, few of them report similar fundamental parameters or reaction orders in carbon. In particular, non-catalytic activation energies for diesel particulate matter have been reported over a broad range: 36 kJ/mol [65], 72-76 kJ/mol [92], 92 kJ/mol [70], 106-126 kJ/mol [71], 137 kJ/mol [72], and 170 kJ/mol [66]. The last value approaches the activation energy of natural graphite which is 188 kJ/mol [67]. Kinetic parameters for biodiesel particulate have been reported in oxidation duration, rather than in terms of kJ/mol [93]. The reaction order for carbon in O_2 oxidation is often reported as ⅔, which likely comes from assuming a shrinking core

model [65, 68, 94], though there has been little done to substantiate this assumption. The reaction order for O_2 in the diesel particulate oxidation reaction has been widely reported to be between 0.5 [92] and 0.6 [70], which is used in this work.

Oxidation models for diesel particulate have thus far only been proposed for the fixed carbon portion. The modeling effort in this work includes the mobile or volatile carbon fraction as well.

5.2 Modeling of Oxidation Experiments

Heterogeneous reactions are a three-stage process: diffusion of gaseous reactants across a boundary layer, chemisorption of reactants onto the surface and desorption of reaction products, which contain atoms from the surface layer of the solid. In order to fully describe the reaction, three things must be considered: the mass balance, the energy balance and the reaction equation that connects them. Isothermal, differential experiments allowed us to isolate the kinetics from the reactor system, therefore it is not necessary to model the flow reactor in order to model the data. For the work reported here, the model system is defined as the diesel particulate matter including the fixed carbon and the volatile carbon considered as a collection of steady state points over the temperature ramp.

5.2.1 Oxidation Reaction Rate

In Chapter 4, we show that the impact of the volatiles on particulate oxidation is a linear shift in the oxidation profile. Following the work of Howard and Essenhigh [95], it was hypothesized that the volatile fraction is burning on the surface of the soot,

occurring simultaneously with the heterogeneous combustion. The basic mechanism for solid particle combustion with gas phase volatile combustion is: at low temperature, slow initial pyrolysis of volatiles with no loss of fixed carbon, then as the temperature increases, heterogeneous combustion begins the loss of fixed carbon and pyrolyzes remaining volatiles.

The reactions of the two carbon phases (volatile and fixed) must be considered jointly to describe the particulate oxidation. We propose an oxidation model that sums the contributions of the fixed carbon and volatile carbon reaction equations to define the overall system.

$$r_{particulate} = r_{fixed\ carbon} + r_{volatile\ carbon} \qquad \text{Equation 5-1}$$

5.2.2 Fixed Carbon Oxidation

This work empirically determined the temperature-dependent, fundamental Arrhenius parameters as the basis of the proposed kinetic model. First order plots, shown in Chapter 4, were linear for both ULSD and B100 particulate oxidation experiments, thereby validating the assumption of a pseudo-first order reaction in carbon. The reaction order in O_2 was assumed to be 0.6, as reported by Yezerets [69, 70]. Therefore the form of the rate equation is defined as

$$r = kA_C[O_2]^{0.6} \qquad \text{Equation 5-2}$$

where A_C is the total carbon surface area available for reaction, comprised of the specific surface area, $A_{specific}$, times the mass of carbon remaining

$$A_C = A_{specific} * C \qquad \text{Equation 5-3}$$

and k is the velocity constant of the reaction defined by the Arrhenius expression

$$k=\eta A*exp(-E_A/RT) \quad \text{Equation 5-4}$$

where η is the effectiveness factor, A is the pre-exponential term, E_A is the temperature dependent activation energy in kJ/mol, R is the universal gas constant in kJ/mol-K and T is the absolute gas temperature in K. For these experiments, the concentration of oxygen was kept constant and the rate equation can be simplified to

$$r = k'A_C \qquad \text{Equation 5-5}$$

where k' is the effective velocity constant and defined as

$$k' = k[O_2]^{0.6} \quad \text{Equation 5-6}$$

where the value of k' can be determined from the Arrhenius expression. Since the reaction rate was shown to have a strong dependence on the available surface area for reaction, the rate equation was proposed to be

$$r_{fixed\ carbon} = k''C*SA \quad \text{Equation 5-7}$$

where k'' is the surface area-dependent velocity constant which includes the oxygen term and SA is the surface area available for reaction. The available surface area is a fuel source dependent and likely operating point and engine type (HD vs LD) parameter, defined as a function of the extent of reaction. The surface area functions were determined experimentally in Chapter 4 as

$$SA = -505\xi^2+957\xi+123.5 \qquad (ULSD) \quad \text{Equation 5-8}$$

$$SA = 1353\xi^3-859\xi^2+1156\xi+157 \quad (B100) \quad \text{Equation 5-9}$$

where ξ is the extent of reaction, defined as

$$\xi = (moles\ carbon\ remaining)/(moles\ carbon\ initial) \quad \text{Equation 5-10}$$

the fraction of carbon remaining. The surface area dependent velocity constant, *k''*, is defined by the Arrhenius expression and the quantities η, A and E_A were measured experimentally in Chapter 4.

5.2.3 Volatile Carbon Pyrolysis Reaction Rate

Volatile evolution with temperature was measured in the TPD experiments discussed in Chapter 4. From an average fit of the plot of extent of reaction with temperature (Figure 27), the reaction rate of the volatile carbon is proposed to be first order. The rate is defined as

$$r_{volatile\ carbon} = k_{vol} * [C_{vol}] \quad \text{Equation 5-11}$$

where k_{vol} is the velocity constant of the reaction and $[C_{vol}]$ is the molar concentration of the volatiles. The velocity constant, k_{vol} is defined as a function of temperature

$$k_{vol} = 9e^{-6}(T^2) + 7.2e^{-3}(T) + 1.44 \quad \text{Equation 5-12}$$

where T is the absolute gas temperature in Kelvin.

5.2.4 Mass Balance and Energy Balances

The mass balance for the system describes the depletion of the particulate mass with time and includes diffusion resistance across the boundary layer as well as the change in mass due to reaction. The mass balance on a mole basis is

$$dN_c/dt = k_m([C_{O,g}]-[C_{O,s}]) + r_{particulate} \quad \text{Equation 5-13}$$

where N_c is the moles of carbon, k_m is the mass transfer coefficient, $[C_{O,g}]$ is the concentration of O_2 in the gas phase, and $[C_{O,s}]$ is the concentration of O_2 at the surface. The mass transfer coefficient was calculated using the limiting case Sherwood number of 2 for

$$Sh = k_m d_p Y_{O2}/D \qquad \text{Equation 5-14}$$

where d_p is the primary particle diameter, Y_{O2} is the mole fraction of O_2 in the gas phase, and D is the molar diffusivity for O_2 in Ar.

Using the pseudo-steady state assumption (PSSA),

$$k_m([C_{O,g}]-[C_{O,s}]) = r_{particulate} \qquad \text{Equation 5-15}$$

we determined that over the entire reaction, the concentration of O_2 at the surface was equal to the concentration in the gas phase, therefore the diffusion term is extraneous and the mass balance can be simplified to

$$dN_c/dt = r_{particulate} \qquad \text{Equation 5-16}$$

which implies that the change in particulate mass is solely related to the rate at which the particle is oxidized for the experiments in the microreactor.

The energy balance for the system relates the change in the internal energy of the system

$$dU/dt = Q_{convection} + Q_{conduction} + Q_{radiation} + Q_{reaction} \qquad \text{Equation 5-17}$$

to the heat transfer from convection, conduction, radiation and reaction. For a small particle, we can assume that the particle is at a constant temperature and therefore neglect the conduction term. The equation becomes

$$(mC_p)dT/dt = r_{particulate}(\Delta H_{f,CO2}) + h(A_{xfer})(T_p-T_g) + \varepsilon\sigma(T_p^4-T_g^4) \quad \text{Equation 5-18}$$

where m is the mass of carbon, C_p is the molar heat capacity, $\Delta H_{f,CO2}$ is the heat of formation of the CO_2 reaction product, h is the heat transfer coefficient, ε is the emissivity of carbon, σ is the Stefan-Boltzmann constant and T_p and T_g are the absolute temperatures of the particle and the gas. The heat transfer coefficient was calculated using the limiting case Nusselt number of 2 for

$$Nu = h*d_p/k_{Ar} \quad \text{Equation 5-19}$$

where k_{Ar} is the thermal conductivity of argon, the main component of the gas stream.

Using the PSSA, we can solve for the relative importance of the radiation and convection terms by

$$r_{particulate}(\Delta H_{f,CO2}) = h(SA)(T_p-T_g) + \varepsilon\sigma(T_p^4-T_g^4) \quad \text{Equation 5-20}$$

in the isothermal system. We found that the reaction did not generate sufficient heat to change the temperature of the particle more than 1K and therefore the particle temperature could be assumed to be equal to the gas temperature.

5.2.5 Validation

The model was tested for both ULSD and B100 particulate samples compared to TPD, fixed carbon TPO and nascent TPO experiments to evaluate the model predictions for the volatile carbon, fixed carbon and total carbon samples. Sample calculations and parameter values are shown in the Appendix.

The fixed carbon model is plotted for ULSD and B100 devolatilized particulates, or fixed carbon, TPO experiments. There is excellent agreement between the model prediction and the ULSD fixed carbon data, as shown in Figure 54. The model prediction for the B100 fixed carbon, Figure 55, was good, though there are two areas where the model slightly under-predicts the conversion. Attempts to improve the fit, discussed in the follow section ‘Sensitivity Analysis’, were unsuccessful.

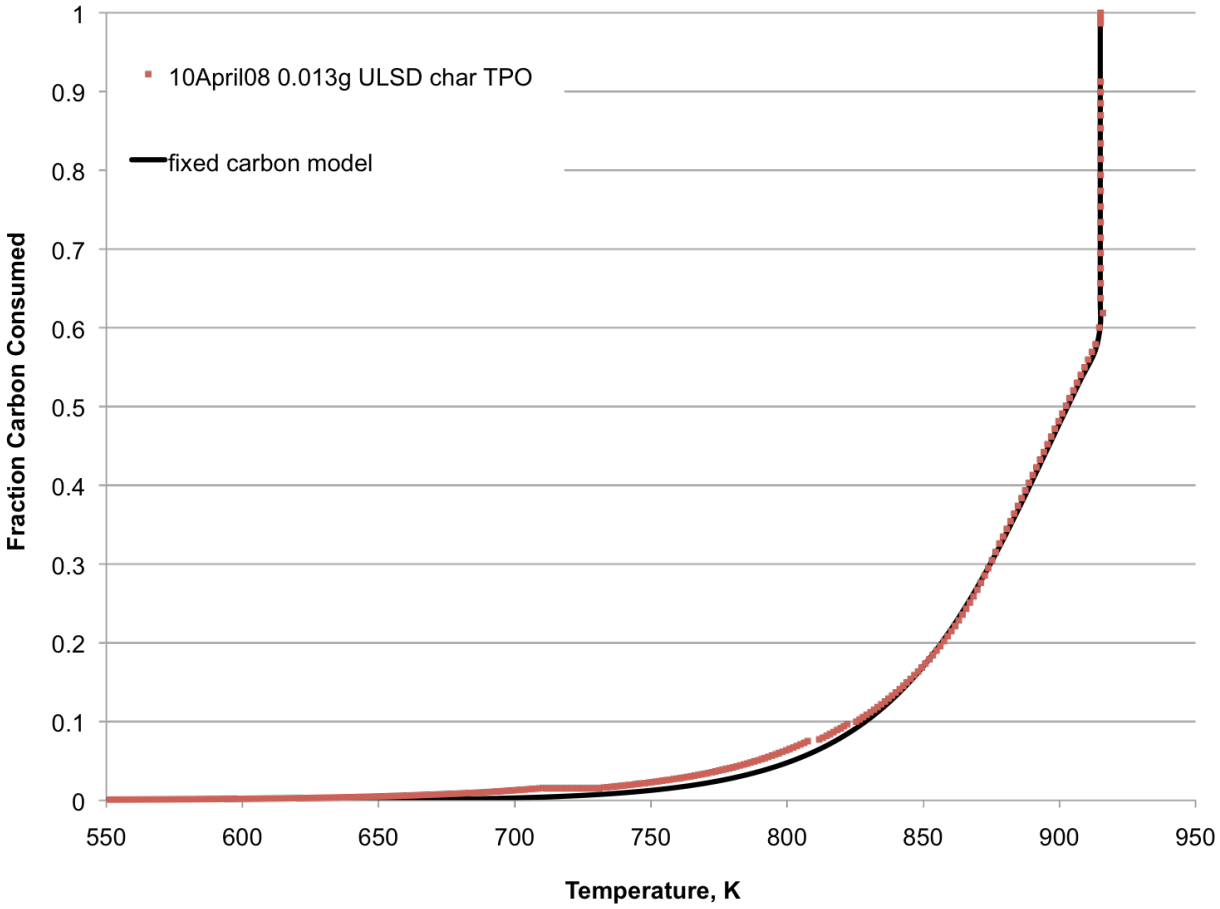

Figure 54 Fixed Carbon model prediction for ULSD fixed carbon plotted with ULSD fixed carbon TPO experimental data.

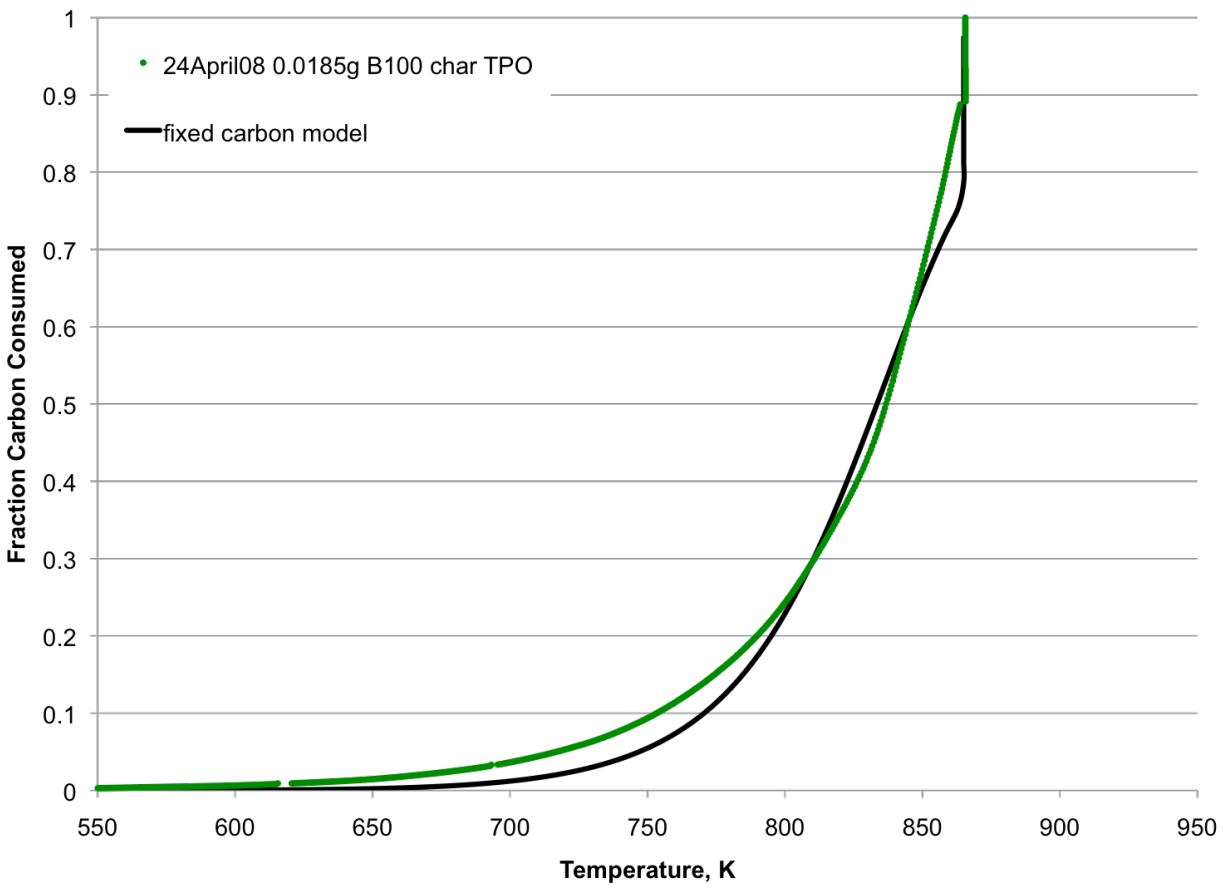

Figure 55 Fixed Carbon model prediction for B100 fixed carbon plotted with B100 fixed carbon TPO experimental data for comparison.

The volatile carbon model is plotted for ULSD and B100 volatiles from TPD experiments. There is good agreement between the model prediction and the ULSD volatile data, as shown in Figure 56. The model prediction for the B100 volatiles, shown in Figure 57, had good trend-wise agreement with the data, however, the model generally under-predicts the conversion. Since the volatiles comprise only a small

percent of the nascent particulate mass, trend-wise agreement is, in the author's opinion, deemed sufficient for modeling the nascent particulate data.

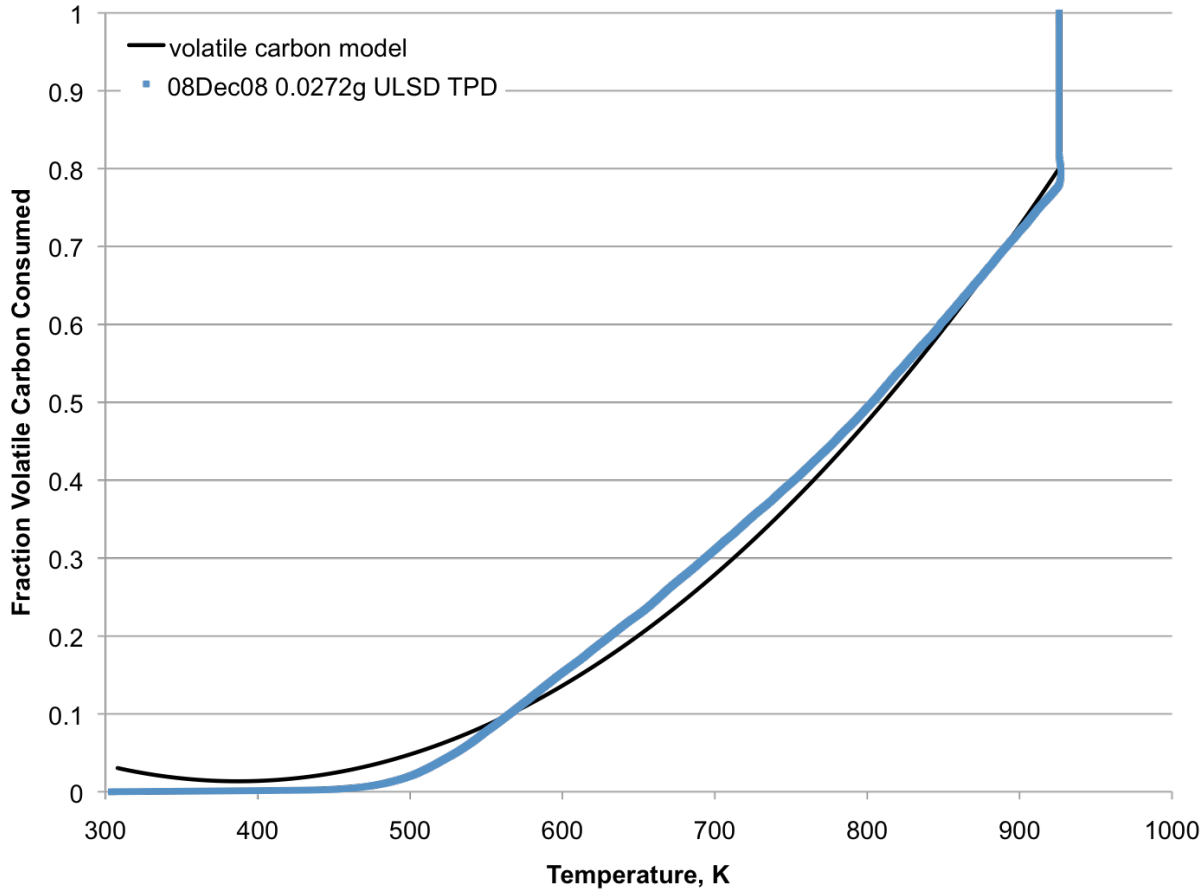

Figure 56 Volatile Carbon model prediction for ULSD volatiles plotted with ULSD TPD experimental data.

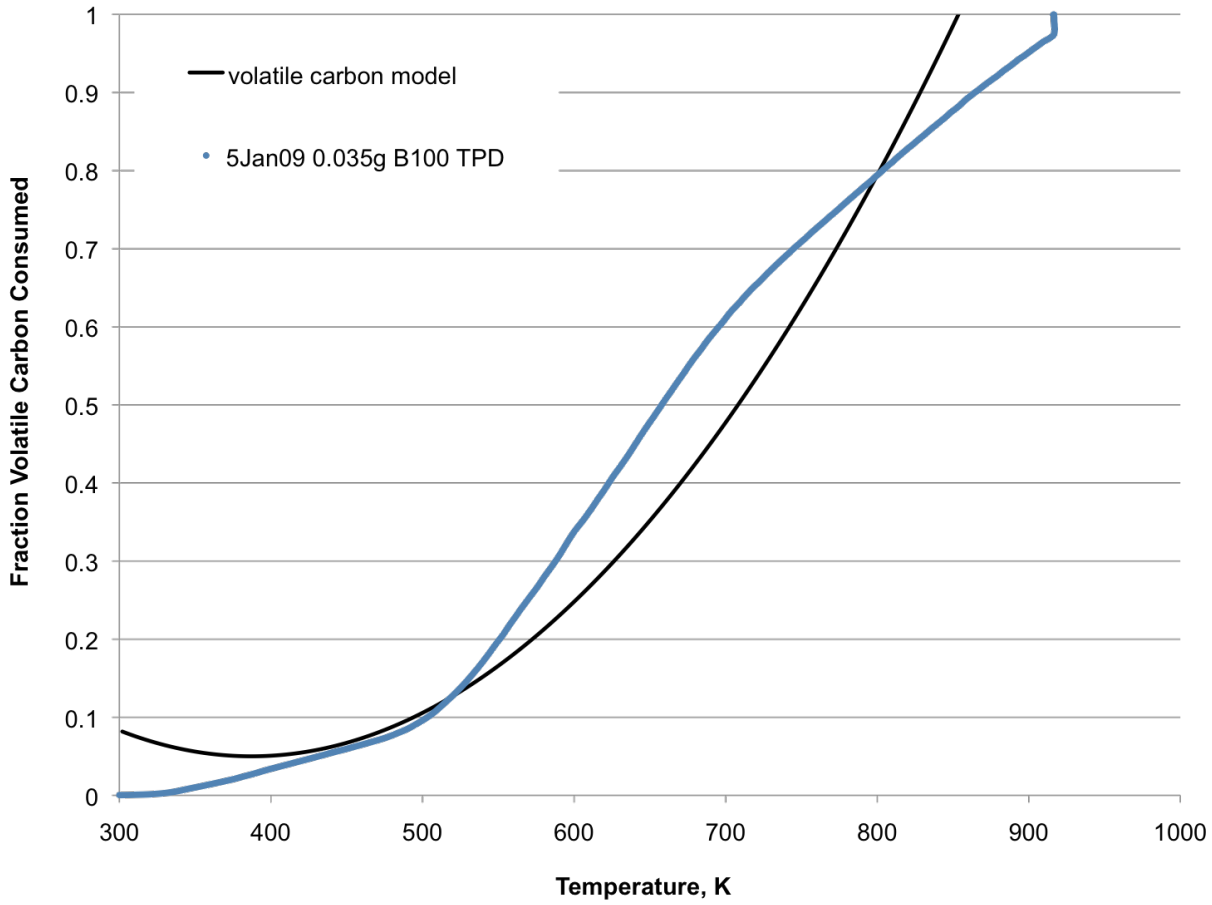

Figure 57 Volatile Carbon model prediction for B100 volatiles plotted with B100 TPD experimental data.

Finally, the simulation results for the combined fixed and volatile carbon models for both ULSD and B100 particulates are plotted in Figure 59 and Figure 59. The model shows very good agreement with data. The simulation for ULSD particulates has a small discrepancy past approximately 75% conversion, under-predicting the data. For B100 particulates, the simulation shows very good agreement with the data. It is interesting to note that the discrepancy in the curves occurs in the area where the

surface area function under-predicts the actual surface area (REF from CH4), the sensitivity of this parameter is discussed in the following section.

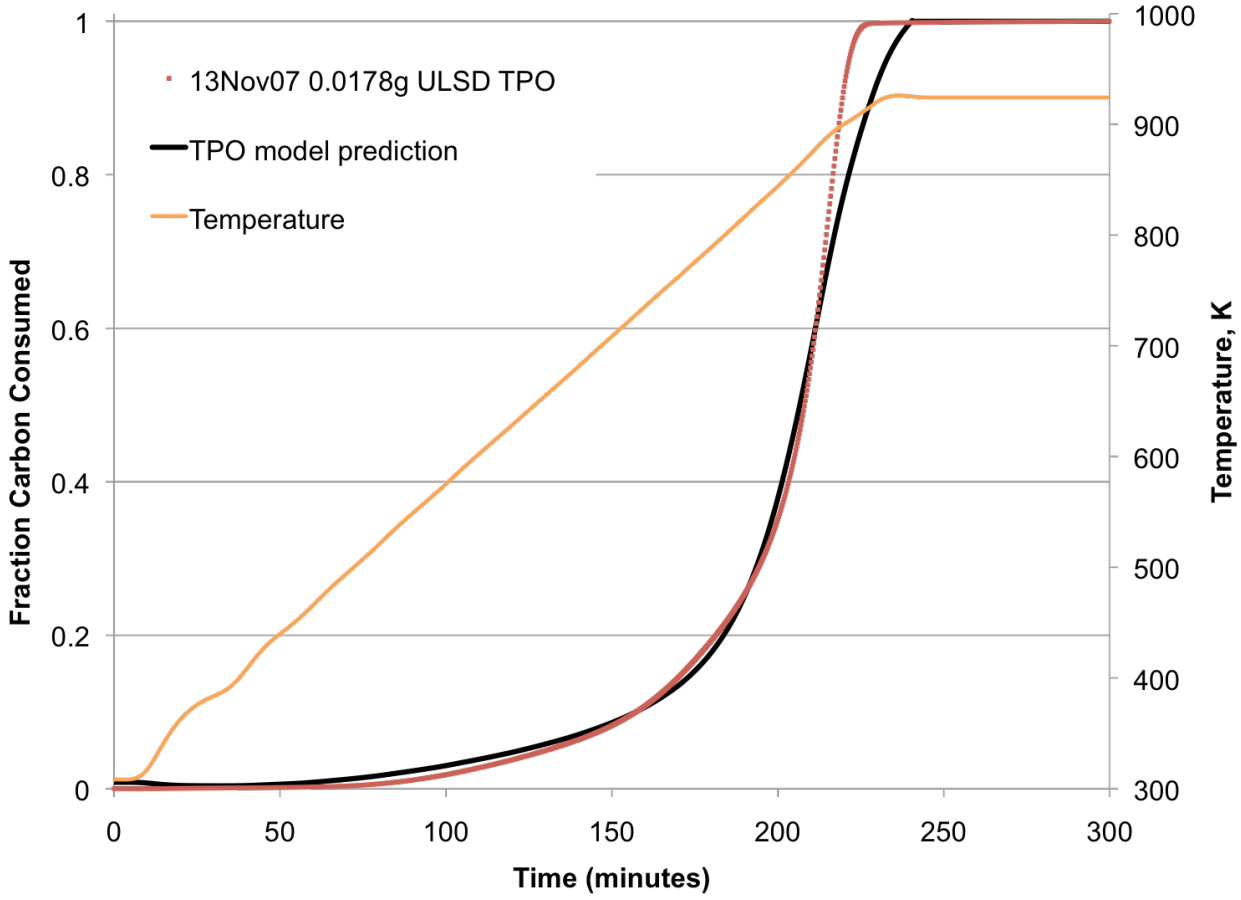

Figure 58 Simulation results for nascent ULSD TPO plotted against experimental data.

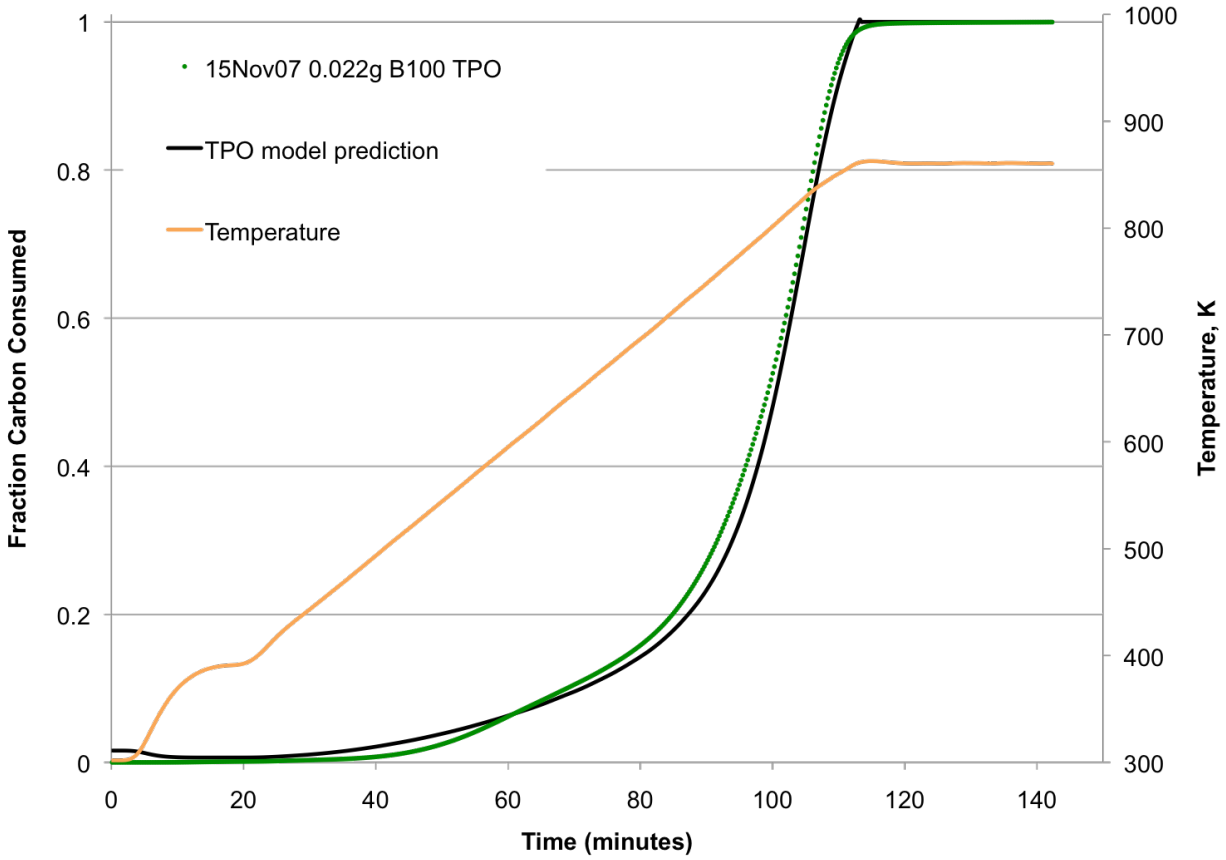

Figure 59 Simulation results for nascent B100 TPO plotted with experimental data.

5.2.6 Sensitivity Analysis

The model was tested for its sensitivity to its independent variables, the surface area prediction and time step in an attempt to better fit the experimental data. The model time step was halved from 7.5s to 3.75s and the surface area function for B100 particulate is examined. The model was not sensitive enough (as shown in the following figures) to the changes in either parameter for adjustments to be made.

The specific surface area plots are given parabolic curve fits in Chapter 4, however, two two-tiered fits (linear + linear and linear + log) were attempted to better describe the data. The specific surface area curve for B100 particulate matter is shown in Figure 60, with the curve fits shown for comparison. The resultant model simulations are shown in Figure 61. The parabolic and linear-log fits show no perceptible differences in their model results. This was expected since their ability to predict the surface area is not drastically different. However, the linear-linear fit does not due as good a job fitting the surface area and that shows up in the model as an over-prediction of the data.

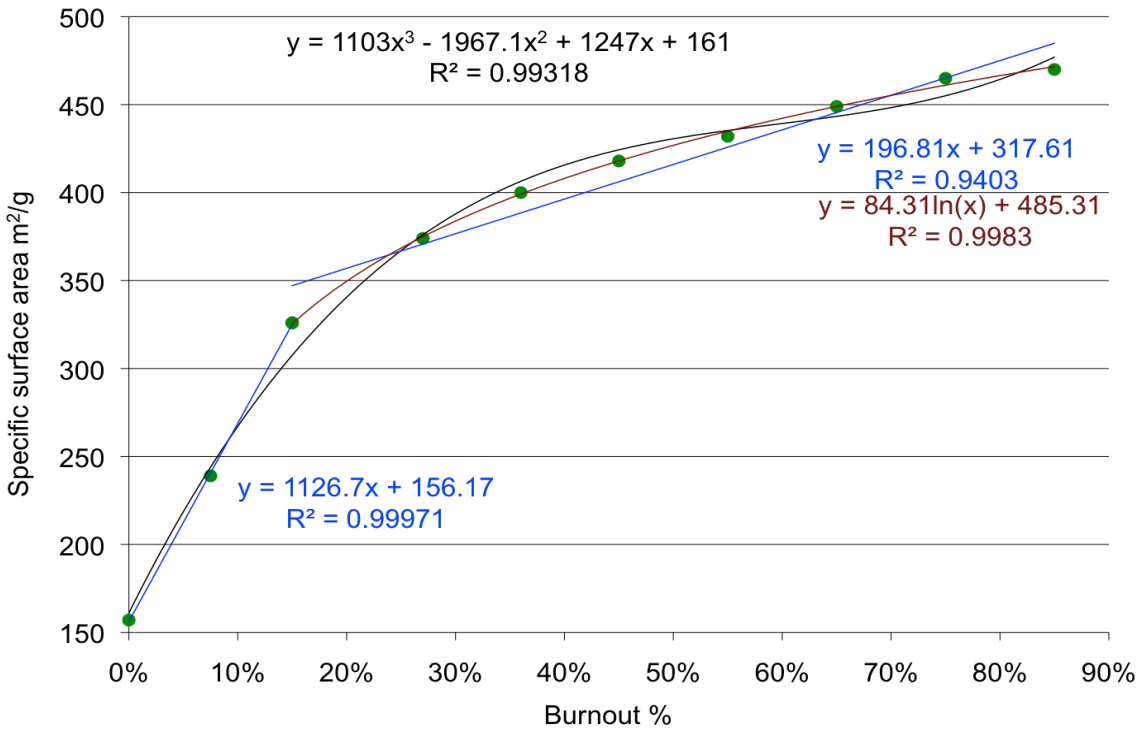

Figure 60 Specific surface area versus burnout for B100 particulate matter. A parabolic curve fit if shown in black, a two-tiered linear fit (0-15%, 15-85%) in blue and a log fit for 15-85% in red.

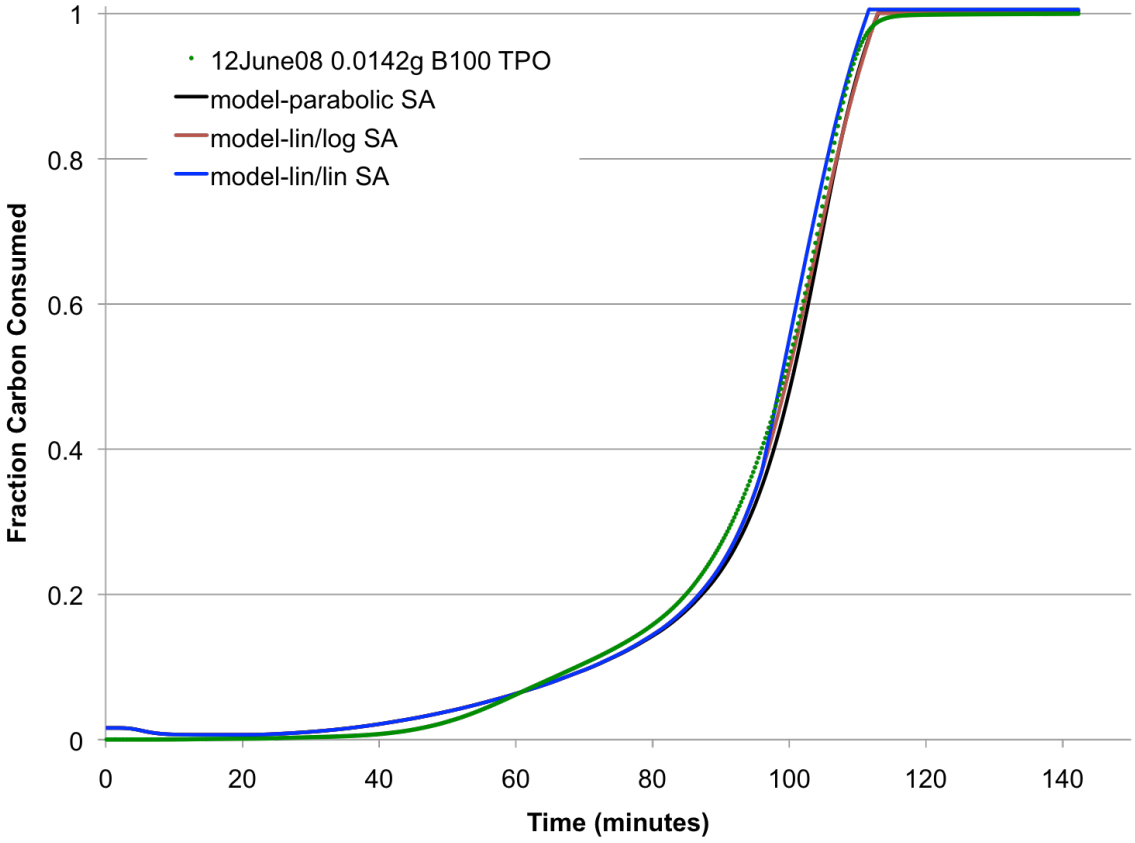

Figure 61 Model predictions of a nascent B100 TPO for three different surface area fits: parabolic (black), linear-log (red) and linear-linear (blue). Experimental data is shown in green for comparison.

The model was also evaluated for its sensitivity to the time-step. Additional time points were added, effectively halving the time-step from 7.5 to 3.75s shown in Figure 62. Reducing the time-step by half did not have an impact on the simulation results.

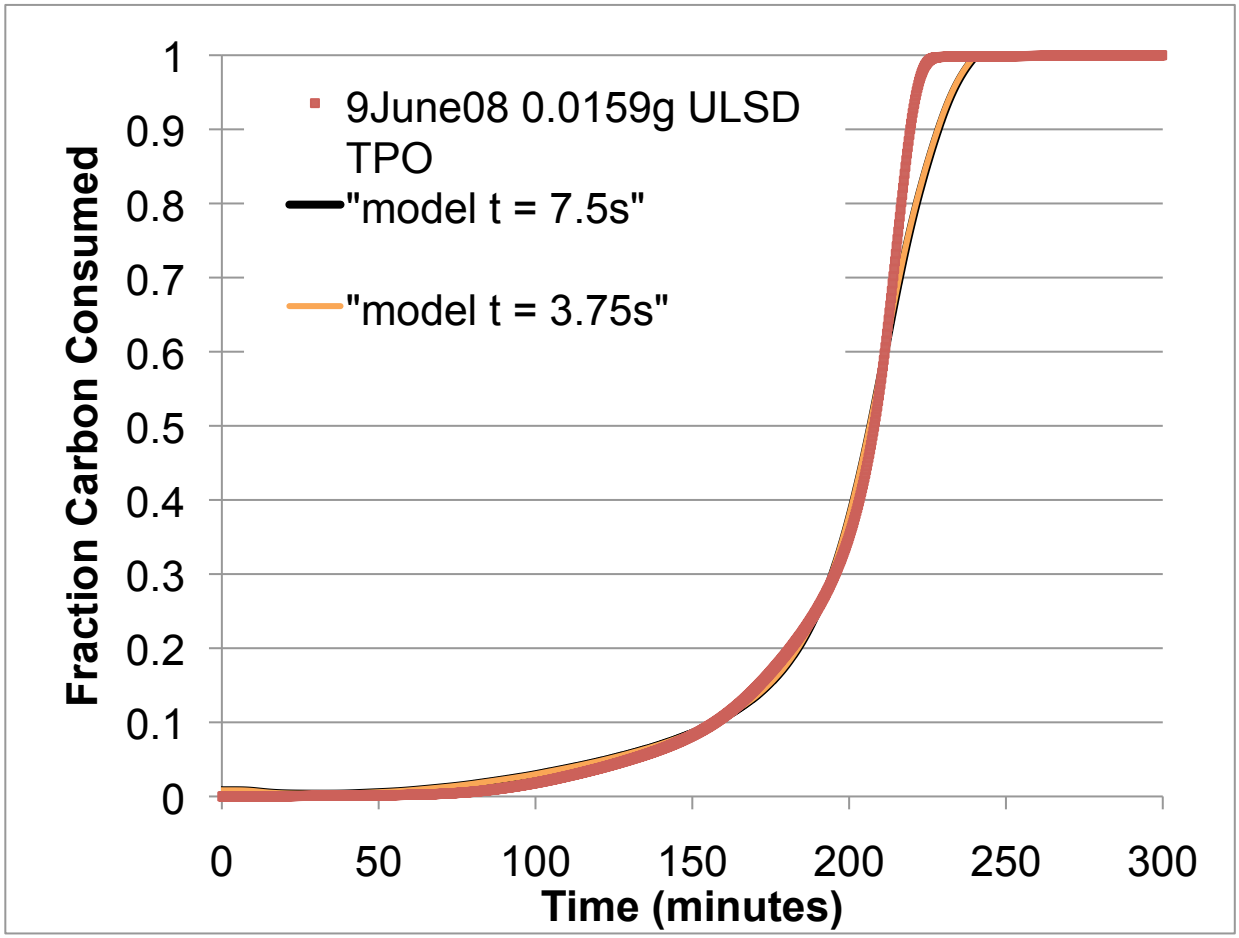

Figure 62 Simulations of a ULSD TPO with a 7.5s (black) and 3.75s (orange) time-step. Experimental data is plotted in red for comparison.

5.3 Summary

A surface area dependent kinetic model was proposed for diesel particulate oxidation independent of fuel type. The impact of the fuel source, in terms of oxidation, appears in the surface area evolution with burnout and is the parameter responsible for the shift seen in the nascent and fixed carbon oxidation curves. Therefore, in order to

predict the behavior of a diesel particulate sample, the surface area must first be known. Although the model required an empirical fit of surface area data, it is able to accurately describe the oxidation process in a more fundamental form that heretofore has been done previously.

6 Summary and Recommendations

6.1 Summary

The objective of this work was to investigate how the oxidation characteristics of diesel particulates are affected by blending soy-based biodiesel fuel with conventional diesel fuel. In addition to directly measuring oxidation characteristics, the DPF particulate produced by different biodiesel-conventional fuel blends was subjected to a range of physical and chemical measurements in order to better understand the mechanisms by which fuel-related changes to oxidation reactivity are brought about.

Diesel particulate matter samples were generated on a Mercedes Benz engine at 1500rpm, 2.6 bar for ULSD, B5, B20 and B100 fuels. Experiments on these samples have shown the following:

- Particulate matter from biofuel and blends oxidizes at lower temperature than particulates from conventional diesel fuel. Increasing biodiesel blending, with the notable exception of B5, lowers particulate oxidation light off and extinction temperatures.
- The presence of the adsorbed volatile hydrocarbons has a favorable impact on soot light off temperature. The amount of volatile content, not the speciation is the important factor behind this advantage.
- Surface area measurements show that the particles from B100 develop porosity much faster than ULSD during initial oxidation, but that by 40% burnout the samples have become quite similar in total surface area.

- HR-TEM imaging shows the soot nanostructure to be influenced by biofuel blend level. Increasing biofuel blending, again with the exception of B5, disrupts the graphitic stacking of the lamella, creating a more open structure. The average carbon lamella length is seen to decrease with higher biofuel content, which implies an increase in the ratio of edge to basal plane carbons.
- Evaluating the reaction rate on the basis of total surface area normalizes the kinetics of ULSD and B100 particulate oxidation. Physical characterization, particularly surface area, of a diesel particulate sample with burnout is the most important factor in determining its reactivity.
- A kinetic model was proposed for the oxidation of both fixed and volatile carbon. The fixed carbon model accounts for the available reactive surface area (with burnout) and uses a single activation energy, independent of fuel source. The model was successfully validated against experimental data. Use of this model in DPF models to predict regeneration may improve the accuracy of DPF control algorithms.

6.2 Recommendations for Future Work

The experimental results presented in this dissertation raise almost as many new questions as they provide answers. Listed here are experiments that I believe would be beneficial to understanding particulate oxidation further.

- Measure surface area with burnout for particulate samples from intermediate blends (B5, B20) generated at 1500rpm, 2.6 bar BMEP and evaluate the model for their nascent TPOs.
- Measure surface area with burnout for ULSD and B100 particulate samples generated at 2300rpm, 4.2 bar to see the impact of engine operating point (cylinder temperature and pressure) on the physical characteristics of particulate and evaluate the model for nascent TPOs of particulates.
- Evaluate kinetics for NO_2 oxidation by isothermal, differential experiments for ULSD and B100.
- Determine whether NO_x oxidation kinetics have the same surface area dependency as oxidation by O_2.
- Investigate the formation of particulates from B5 in order to understand the disadvantage of blending small amounts of oxygenated fuel.

7 References

1. Majewski, A. *DieselNet*. Available from: http://www.dieselnet.com/news.
2. Sluder, S., et al., *Implications of Particulate and Precursor Compounds Formed During High-Efficiency Clean Combustion in a Diesel Engine.* SAE, 2005. **2005-01-3844**: p. 1-11.
3. Konstandopolous, A.a.J., J., *Wall-Flow Diesel Particulate Filters - Their Pressure Drop and Collection Efficiency.* SAE, 1989. **SAE 890405**.
4. Konstandopolous, A., et al., *Fundamental Studies of Diesel Particulate Filters: Transient Loading, Regeneration and Aging.* SAE, 2000. **2000-01-1016**: p. 1-25.
5. Bissett, E., *Thermal Regeneration of Particle Filters with Large Conduction.* Mathematical Modeling, 1985. **6**: p. 1-18.
6. Song, J., et al., *Examination of the oxidation behavior of biodiesel soot.* Combustion and Flame, 2006. **146**(4): p. 589-604.
7. Nakatani, K., et al., *Simultaneous PM and NOx Reduction System for Diesel Engines.* SAE, 2002. **SAE 2002*01-0957**.
8. Konstandopolous, A., E. Skaperdas, and M. Masoudi, *Inertial Contributions to the Pressure Drop of Diesel Particulate Filters.* SAE, 2001. **2001-01-0909**: p. 1-12.
9. Huynh, C., et al., *A One-Dimensional Computational Model for Studying the Filtration and Regeneration Characteristics of a Catalyzed Wall-Flow Diesel Particulate Filter.* SAE, 2003. **SAE 2003-01-0841**.
10. Harris, S. and A. Weiner, *Chemical kinetics of soot particle growth.* Annual Review of Physical Chemistry, 1985. **36**(1): p. 31-52.
11. Dec, J., *Conceptual Model of DI Diesel Combustion Based on Laser-Sheet Imaging.* SAE, 1997. **970873**: p. 1-30.
12. Harris, S. and I. Kennedy, *The Coagulation of Soot Particles with van der Waals Forces.* Combust. Sci. and Tech., 1988. **59**: p. 443-454.
13. Clague, A., et al., *A comparison of diesel engine soot with carbon black.* Carbon, 1999. **37**(10): p. 1553-1565.

14. Frenklach, M. and H. Wang, *Soot Formation in Combustion, Mechanisms and Models*, in *Springer Sereies in Chemical Physics*, H. Bockhorn, Editor. 1994, Springer-Verlang: Berlin.
15. Dryer, F. and R. Sawyer, *Physical and Chemical Aspects of Combustion*. 1997, Gordon & Breach: New York. p. 107-253.
16. Naegeli, D., L. Dodge, and C. Moses, Combust. Sci. and Tech., 1983. **35**.
17. Knauer, M., Carrara, M., Rothe, D. and Niessner, R., *Changes in Structure and Reactivity of Soot during Oxidation and Gassification by Oxygen, Studied by Micro-Raman Spectroscopy and Temperature Programmed Oxidation.* Aerosol Sc. & Tech., 2009. **43**: p. 1-8.
18. Lee, K. and J. Zhu, *Evolution in Size and Morphology of Diesel Particulates along the Exhaust System.* SAE, 2004. **SAE 2004-01-1981**.
19. Song, J., *PhD Thesis.* The Pennsylvania State University, 2005: p. 1-80.
20. Boehman, A., J. Song, and M. Alam, *Impact of Biodiesel Blending on Diesel Soot and the Regeneration of Particulate Filters.* Energy & Fuels, 2005. **19**(2005): p. 1857-1864.
21. Stasio, S., *Electron Microscopy Evidence of Aggregation Under Three Different Size Scales for Soot Nanoparticles in Flames.* Carbon, 2001. **39**.
22. Lahaye, J. and G. Pardo, *Morphology and Internal Strucutre of Soot and Carbon Blacks*, in *Particulate Carbon Formation During Combustion*, Siegla, Editor. 1981, Plenum Press: New York. p. 33-55.
23. Vander Wal, R. and A. Tomasek, *Soot oxidation dependence upon initial nanostructure.* Combustion and Flame, 2003. **134**(1-2): p. 1-9.
24. Palmer, H. and C. Cullis, in *The Chemistry and Physics of Carbon*, P. Walker Jr, Editor. 1965, Dekker: New York. p. 265.
25. Vander Wal, R. and A. Tomasek, *Soot nanostructure: dependence upon synthesis conditions.* Combustion and Flame, 2004. **136**(1-2): p. 129-140.
26. Yezerets, A., et al. *Towards Fuel Efficient DPF Systems: Understanding the Soot Oxidation Process*. in *DEER*. 2005. Detroit, MI.

27. Braun, A., Shah,N., Huggins, F., Huffman, G., Wiricj, S., Jacobsen, C., Kelly, K. and Sarofim, A., *A study of diesel PM with X-ray microscopy.* Fuel, 2004. **83**(7): p. 997-1000.
28. Braun, A., et al., *Size-range analysis of diesel soot with ultra-small angle X-ray scattering.* Combustion and Flame, 2004. **137**(1-2): p. 63-72.
29. Su, D., et al., *Microstructure and oxidation behaviour of Euro IV diesel engine soot: a comparative study with synthetic model soot substances.* Catalysis Today, 2004. **90**(1-2): p. 127-132.
30. Marsh, H., *Kinetics and Catalysis of Carbon Gassification*, in *Introduction to Carbon Science*. 1989, Butterworths: London.
31. Smith, W.R.a.P., M.H., *The oxidation of graphitized carbon black.* Journal of Electrochemistry, 1956. **20**: p. 689-691.
32. Rosner, D.a.A., H., *Comparitive studies of the attack of pyrolytic and isotropic graphite by atomic and molecular oxygen at high temperature.* AIAA Journal, 1968. **6**(4): p. 650-654.
33. Hippo, E., Murdie, N. and Hyjazie,A., *The role of active sites in the inhibition of Gas-Carbon Reactions.* Carbon, 1989. **27**(5): p. 689-695.
34. Higgins, K., et al., *Size-selected nanoparticle chemistry: Kinetics of soot oxidation.* Journal of Physical Chemistry A, 2002. **106**(1): p. 96-103.
35. Sluder, C., et al., *Fuel Property Effects on Emissions from High Efficiency Clean Combustion in a Diesel Engine.* SAE, 2006. **SAE 2006-01-0080**.
36. Sluder, C., et al., *Exhaust Chemistry of Low-NOX, Low-PM Diesel Combustion.* SAE, 2004. **2004-01-0114**: p. 1-10.
37. Lewis, S., et al., *Partial Oxidation Products and Other Hydrocarbon Species in Diesel HCCI Exhaust.* SAE, 2005. **SAE 2005-01-3737**.
38. Kolodziej, C., *Comprehensive Characterization of Particulate Emissions from Advanced Diesel Combustion.* MS Thesis, 2007: p. 1-148.
39. Stratakis, G., G. Konstantas, and A. Stamatelos, *Experimental investigation of the role of soot volatile organic fraction in the regeneration of diesel filters.*

Proceedings of the Institution of Mechanical Engineers, Part D: Journal of Automobile Engineering, 2003. **217**(4): p. 307-317.

40. Essenhigh, R., *Fundamentals of Coal Combustion*, in *Chemistry of Coal Utilization*, M. Ellis, Editor. 1981, Wiley Interscience: New York. p. 1153-1311.
41. Smith, I., *The intrinsic reactivity of carbons to oxygen.* Fuel, 1978. **57**(7): p. 405-414.
42. Marsh, H., *How Oxygen Molecules Gasify Carbons.* Spec. Pub. Chem. Soc., 1978. **32**(133-174).
43. Essenhigh, R. and M. Misra, *Autocorrelations of kinetic parameters in coal and char reactions.* Energy & Fuels, 1990. **4**(2): p. 171-177.
44. Essenhigh, R., *Combustion Characteristics of Carbon: Influence of the Zone I - Zone II Transition on Burnout in Pulverized Coal Flames.* Energy & Fuels, 1999. **13**(955-960).
45. Smoot, L.D.a.S., P., *Coal Combustion and Gassification*. 1985, New York: Plenum Press.
46. Back, M., *The Kinetics of the Reaction of Carbon with Oxygen.* Canadian Journal of Chemistry, 1997. **75**: p. 249-257.
47. Walker, P., *Gas Reactions of Carbon*. 1959, New York: Academic Press.
48. Gray, D., Cogoli, J. and Essenhigh, R., *Problems in Pulverized Coal and Char Combustion.* Advances in Chemistry Series, 1976. **132**(72).
49. Essenhigh, R., R. Froberg, and J. Howard, *Combustion Behavior of Small Particles.* Ind. Eng. Chem. , 1965. **57**: p. 32-43.
50. Smoot, D., *International Research Centers' Activities in Coal Combustion.* Progress in Energy and Combustion Science, 1998. **24**: p. 409-501.
51. Essenhigh, R., *Structure-based Predictive Model for Char Combustion.* Report, 1998: p. 1-20.
52. Walker, P., *Carbon: An old but new material revisited.* Carbon, 1990. **28**(2/3): p. 262-279.
53. Hurt, R. and B. Haynes, *On the origin of power-law kinetics in carbon oxidation.* Proceedings of the Combustion Institute, 2005. **30**(2): p. 2161-2168.

54. Hurt, R. and J. Gibbins, *Residual carbon from pulverized coal fired boilers: 1. Size distribution and combustion reactivity.* Fuel, 1995. **74**(4): p. 471-480.
55. Smith, P. and L. Smoot, *One-Dimensional Model for Pulverized Coal Combustion and Gasification.* Combustion Sc. & Tech., 1980. **23**(1): p. 17-31.
56. Alvarez, T., et al., *influence of coal oxidation upon char gassification reactivity.* Fuel 1995. **74**(5): p. 729-735.
57. Essenhigh, R.a.M., A., *Influence of Pressure on the Combution Rate of Carbon.* Proceedings of the Combustion Institute, 1996. **26**: p. 3085-3094.
58. Zeng, D., *Effects of Pressure on Coal Pyrolysis at High Heating Rates and Char Combustion*, in *Chemical Engineering*. 2005, Brigham Young University: Provo.
59. Laurendeau, N., *Heterogeneous Kinetics of Coal Char Gassification and Combustion.* Progress in Energy and Combustion Science, 1978. **4**: p. 221-270.
60. Bird, R., Stewart, W. and Lightfoot, E., *Transport Phenomena*. 1960, New York: John Wiley & Sons Inc.
61. Vannice, M.A., *Kinetics of Catalytic Reactions*. 2005, New York: Springer Science + Business Media.
62. Thiele, E., *Relation between Catalytic Activity and Size of Particle.* Ind. Eng. Chem., 1939. **31**.
63. Essenhigh, H., et al. *Determination of Global Kinetics of Coal Volatiles Combustion*. in *International Combustion Symposium*. 1990.
64. Stanmore, B., J. Brilhac, and P. Gilot, *The Oxidation of Soot: A review of experiments, mechanisms and models.* Carbon, 2001. **39**(15): p. 2247-2268.
65. Ciambelli, P., *Catalytic Combustion of Carbon Particles.* Catalysis Today, 1996. **27**: p. 99-106.
66. Lahaye, J., *Influence of Cerium Oxide on the Formation and Oxidation of Soot.* Combustion and Flame, 1996. **104**: p. 199-207.
67. Zaghib, K., X. Song, and K. Kinoshita, *Thermal analysis of the oxidation of natural graphite: isothermal kinetic studies.* Thermochimica Acta, 2001. **371**(1-2): p. 57-64.
68. Neeft, J., *Kinetics of oxidation of diesel soot.* Fuel, 1997. **76**: p. 1129-1136.

69. Yezerets, A., N. Currier, and H. Eadler, *Experimental Determination of the Kinetics of Diesel Soot Oxidation by O2 - Modeling Consequences.* SAE, 2003. **2003-01-0833**: p. 1-10.
70. Yezerets, A., et al., *Quantitative Flow-Reactor Study of Diesel Soot Oxidation Processes.* SAE, 2002. **SAE 2002-01-1684**.
71. Yezerets, A., et al., *Investigation of the oxidation behavior of diesel particulate matter.* Catalysis Today, 2003. **88**(1-2): p. 17-25.
72. Yezerets, A., et al., *Differential kinetic analysis of diesel particulate matter (soot) oxidation by oxygen using a step–response technique.* Applied Catalysis B, Environmental, 2005. **61**(1-2): p. 120-129.
73. Stamatelos, A. and I. Kandylas, *Modeling Catalytic Regeneration of Diesel Particulate Filters, Taking into Account Adsorbed Hydrocarbon Oxidation.* Ind. Eng. Chem., 1999. **38**: p. 1866-1876.
74. Wagner, R., et al., *Simultaneous Low Engine-Out NOx and Particulate Matter with Highly Diluted Diesel Combustion.* SAE, 2003. **2003-01-0262**: p. 1-10.
75. Kittleson, D., Abdul-Khalek, I., Graskow, B., Brear, F. and Wei, Q., *Diesel Exhaust Particle Size: Measurement Issues and Trends.* SAE, 1998. **SAE 980525**.
76. Vander Wal, R., et al., *Analysis of HRTEM images for carbon nanostructure quantification.* Journal of Nanoparticle Research, 2004. **6**(6): p. 555-568.
77. Vander Wal, R., et al., *Soot Nanostructure: Physical and Chemical Characterization*, in *ORNL Fuels, Engines and Emissions Research Group Presentation*. 2007.
78. US-EPA, *Method 3546*, U.-E.P. Agency, Editor.
79. Storey, J., et al., *Analysis of Semivolatile Organic Compounds in Diesel Exhaust Using a Novel Sorption and Extraction Method.* SAE, 1999. **1999-01-3534**: p. 1-5.
80. Brunauer, S., P. Emmett, and E. Teller, *BET Theory.* J. Am. Chem. Soc., 1938. **60**(2): p. 309-319.
81. Al-Qurashi, K. and A. Boehman, *Impact of exhaust gas recirculation (EGR) on the oxidative reactivity of diesel engine soot.* Combustion and Flame, 2008. **155**(4): p. 675-695.

82. EPA, U., *A Comparative Analysis of Biodiesel Impacts on Exhaust Emissions*, in *420-P-02-001*, U.S.E.P. Agency, Editor. 2002.
83. Mccormick, R., et al., *Effects of Biodiesel Blends on Vehicle Emissions: Fiscal Year 2006 Annual Operating Plan Milestone 10.4.* Report, 2006: p. 1-69.
84. Han, M., et al., *Soybean and Coconut Biodiesel Fuel Effects on Combustion Characteristics in a Light-Duty Diesel Engine* SAE, 2008. **2008-01-0046**: p. 1-12.
85. Kousoulidou, M., et al., *Evaluation of Biodiesel Blends on the Performance and Emissions of a Common-Rail Light-Duty Engine and Vehicle* SAE 2009. **2009-01-0692**: p. 1-10.
86. Graboski, M., et al., *The Effect of Biodiesel Composition on Engine Emissions from a DDC Series 60 Diesel Engine: Final Report; Report 2 in a Series of 6.* Report, 2003: p. 1-91.
87. Williams, A., et al., *Effect of Biodiesel Blends on Diesel Particulate Filter Performance; SAE Paper No. 2006-01-3280.* SAE, 2006. **2006-01-3280**: p. 1-11.
88. Vander Wal, R., *Soot Nanostructure: Definition, Quantification and Implications.* SAE, 2005. **2005-01-0964**: p. 1-10.
89. Smith, I., *The Kinetics of Combustion of Pulverized Semi-Anthracite in the Temperature Range 1400-2200K.* Combustion and Flame, 1971. **17**: p. 421-428.
90. Vander Wal, R., et al., *HRTEM Study of diesel soot collected from diesel particulate filters.* Carbon, 2007. **45**(1): p. 70-77.
91. Vander Wal, R. and C. Mueller, *Initial Investigation of Effects of Fuel Oxygenation on Nanostructure of Soot from a Direct-Injection Diesel Engine.* Energy Fuels, 2006. **20**(6): p. 2364-2369.
92. Shangguan, W.F., Teraoka, Y., and Kagawa, S., *Kinetics of soot-O2-NO reactions over spinel-type CuFe2O4 catalyst.* Applied Catalysis B, Environmental, 1997. **12**: p. 237-247.
93. Mccormick, R., et al., *Biodiesel R&D at NREL.* National Biodiesel Conference, 2006: p. 1-24.

94. Kapteijn, F., R. Meijer, and J. Moulijn, *On Why do Different Carbons Show Different Gassification Rates: A Transient Isotopic CO2 Gassification Study.* Carbon, 1994. **32**(7): p. 1223-1231.
95. Howard, J. and H. Essenhigh, *Mechanism of Solid-Particle Combustion with Simultaneous Gas-Phase Volatiles Combustion.* Symposium on Combustion (Int), 1967: p. 399-408.
96. Kostaglou, M. and A. Konstandopolous, *Effect of Soot Layer Microstructure on Diesel Particulate Filter Regeneration.* AIChE, 2005. **51**(9): p. 2534-2546.
97. Koltsakis, G., et al., *Flow Maldistribution Effects on DPF Performance* SAE, 2009. **2009-01-1280**: p. 1-15.
98. (MECA), M.o.E.C.A. *Diesel Particulate Filter Maintenance: Current Practices and Experience.* 2005. Washington, DC.
99. Bunting, B., et al., *Phosphorous Poisoning and Phosphorous Exhaust Chemistry with Diesel Oxidation Catalysts.* SAE, 2005. **2005-01-1758**.
100. Bardaz, E., et al., *Effects of Lubricant Derived Chemistries on Performance of Catalyzed Diesel Particulate Filters.* SAE, 2005. **2005-012168**.
101. Sappok, A., D. Beauboef, and V. Wong, *A Novel Accelerated Aging System to Study Lubricant Additive Effects on Diesel Aftertreatment System Degradation.* SAE, 2008. **2008-01-1549**.
102. Karin, P., et al., *Microscopic Visualization of PM Trapping and Regeneration in Micro-Structural Pores of a DPF Wall.* SAE, 2009. **2009-01-1476**: p. 1-9.
103. Daido, S. and N. Takagi, *Visualization of the PM Deposition and Oxidation Behavior Inside a DPF Wall.* SAE, 2009. **2009-01-1473**.
104. Zanhuis, J., et al., *Nondestructive X-ray Inspection of Thermal Damage, Soot and Ash Distributions in Diesel Particulate Filters.* SAE, 2009. **2009-01-0289**: p. 1-8.
105. Ismail, B., et al., *Development of a non-destructive neutron radiography technique to measure the three-dimensional soot deposition profiles in diesel engine exhaust systems.* Journal of Aerosol Science, 2004. **35**(10): p. 1275-1288.

106.Calzada, E., B. Schillinger, and F. Grunauer, *Construction and Assembly of the Neutron Radiography and Tomography Facility ANTARES at FRM-II.* Nuclear Instruments & Methods in Physics Research A, 2005. **542**: p. 34-44.

107.Harvel, G., et al., *Measurement of Multi-Dimension Soot Distribution in Diesel Particulate Filters by a Dynamic Neutron Radiography* SAE, 2009. **2009-01-1263**: p. 1-8.

108.Manke, I., et al., *Investigation of soot sediments in particulate filters and engine components* Manuscript, 2009: p. 1-18.

109.Anderson, I., R. McGreevy, and H. Bilheux, *Neutron Scattering Applications and Techniques*. 2009: Springer Science.

110.Herman, G., *Reconstruction from Projections: The Fundamentals of Computerized Tomography*. 1980, New York: Academic Press.

111.X-rayLAB, *Octopus*.

112.Sappok, A., et al., *Characteristics and Effects of Ash Accumulation on Diesel Particulate Filter Performance: Rapidly Aged and Field Aged Results* SAE 2009. **2009-01-1086**: p. 1-17.

8 Appendices

8.1 Appendix 1: Acronyms & Glossary

B#	Biodiesel fuel at #% volumetric blend
BET	Brunnauer Emmet Teller Isotherm Measurement of surface area
BMEP	Brake Mean Effective Pressure
CI	Compression ignition (diesel engine)
Char	Devolatilized particulate matter or fixed carbon
DOC	Diesel Oxidation Catalyst
DPF	Diesel Particulate Filter
EC	Elemental carbon, also known as fixed carbon
EGR	Exhaust Gas Recirculation
FSN	Filter Smoke Number
HC	Hydrocarbon
HCCI	Heterogeneous Charge Compression Ignition
HD	Heavy Duty Engine
HECC	High Efficiency Clean Combustion
HFID	Heated Flame Ionization Detector
HR-TEM	High Resolution Transmission Electron Microscopy
Lamella	carbon graphene segment
LD	Light Duty Engine
Nascent	Particulate matter in its natural state, not devolatilized

NDIR	Nondispersive Infrared
OC	Organic carbon
PAH	Polyaromatic hydrocarbons
PM	Particulate matter, also known as diesel soot = EC+OC
SI	Spark ignition (gasoline engine)
SME	Soy methyl ester biodiesel
SOF	Soluble Organic Fraction of particulate matter
SOI	Start of Injection
THC	Total Hydrocarbon
TPD	Temperature Programmed Desorption
TPO	Temperature Programmed Oxidation
TWC	Three Way Catalyst
VOF	Volatile Organic Fraction of particulate matter
ULSD	Ultra Low Sulfur Diesel
ZrO_2	Yttrium stabilized Zirconium Oxide (beads)

8.2 Appendix 2: Additional Experiments

8.2.1 A2.1 Stepped Temperature Programmed Desorption

The ULSD sample was further investigated to determine if the volatiles came off in a single evolution, or over the course of the temperature ramp. A stepped TPD was performed, shown in where volatile evolution was allowed to drop to near baseline conditions before the next temperature step was taken.

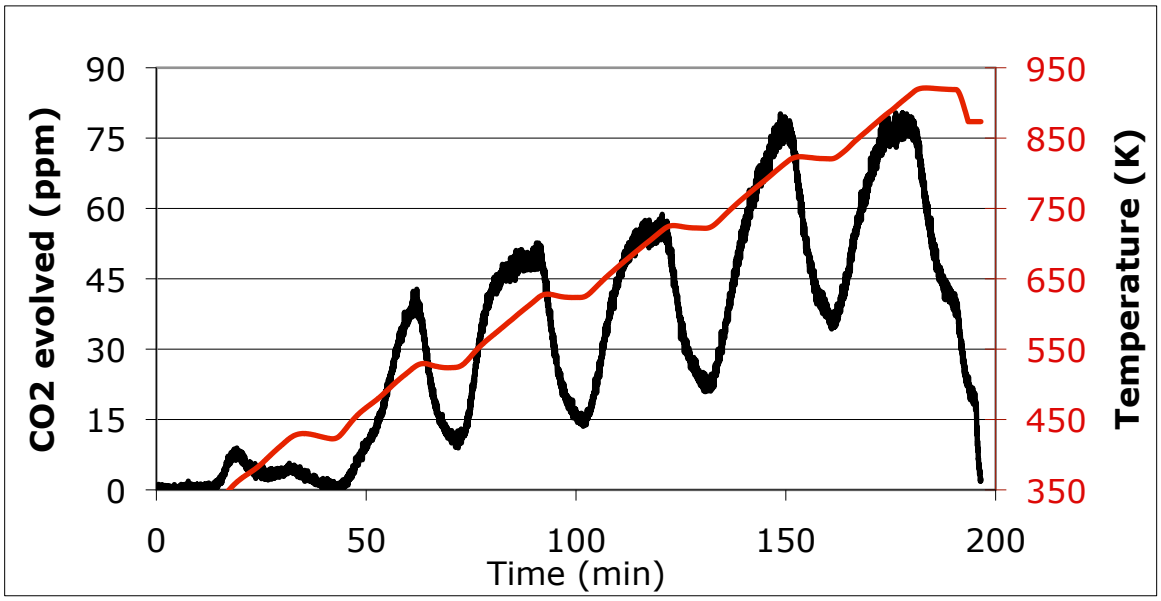

Figure A2-1 Stepped TPD of ULSD PM.

Comparing the boiling point ranges of the species from the SOF extract to the stepped TPD profiles might allow insight into which compounds and in what relative amount are likely coming off over the course of the TPD. It also may clarify if any of the elemental carbon is being pyrolyzed during the TPD. A similar experiment for B100 particulates would also be of interest.

8.2.2 A2.2 X-ray Photoacoustic Spectroscopy (XPS)

Nascent particulate samples were analyzed by XPS at the ORNL High Temperature Materials Laboratory and at USRA. Data from both sources was combined in the figure.

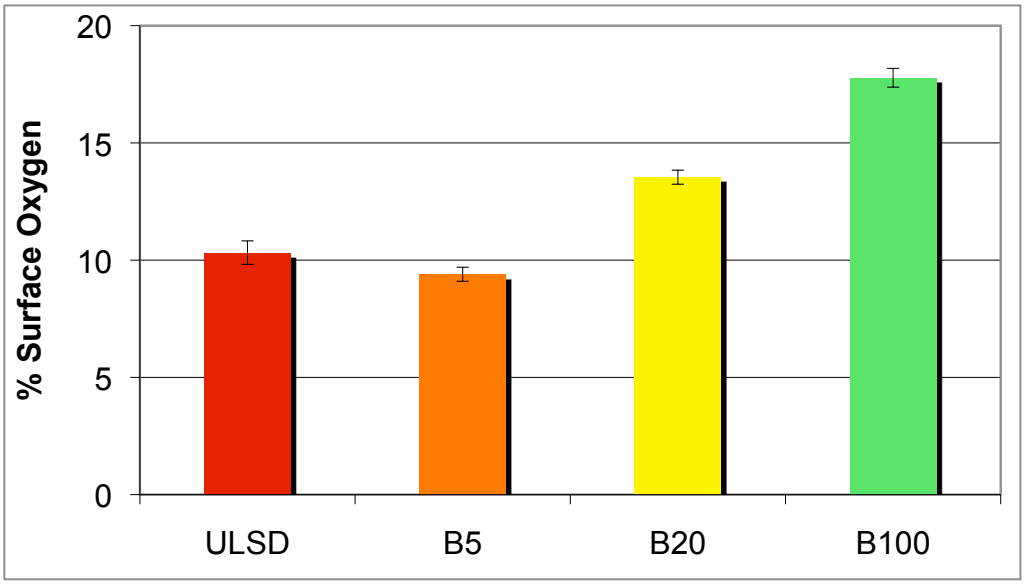

Figure A2-2 Percent surface oxygen by XPS.

With the notable exception of B5, there appears to be a trend of increasing bound oxygen on the surface of the particle with increased biofuel level.

A2.3 Oxygen Chemisorption Measurements

Oxygen chemisorption measurements were made on devolatilized samples, using the microreactor, in an effort to measure the active surface area of the particulates. Briefly, samples were heated to 473 K under inert, exposed to 20% O_2 in

inert for 10 hours at 473 K, then flushed with inert for 1 hour to remove loosely bound O_2, finally, samples were put through a temperature ramp from 473-923K at 10 K per minute to remove bound oxygen as CO_2. The figure shows the grams of O_2 chemisorbed per gram of carbon sample. The trend of increasing O_2 with increasing biodiesel level, with the exception of B5 is the same as was seen in the XPS data.

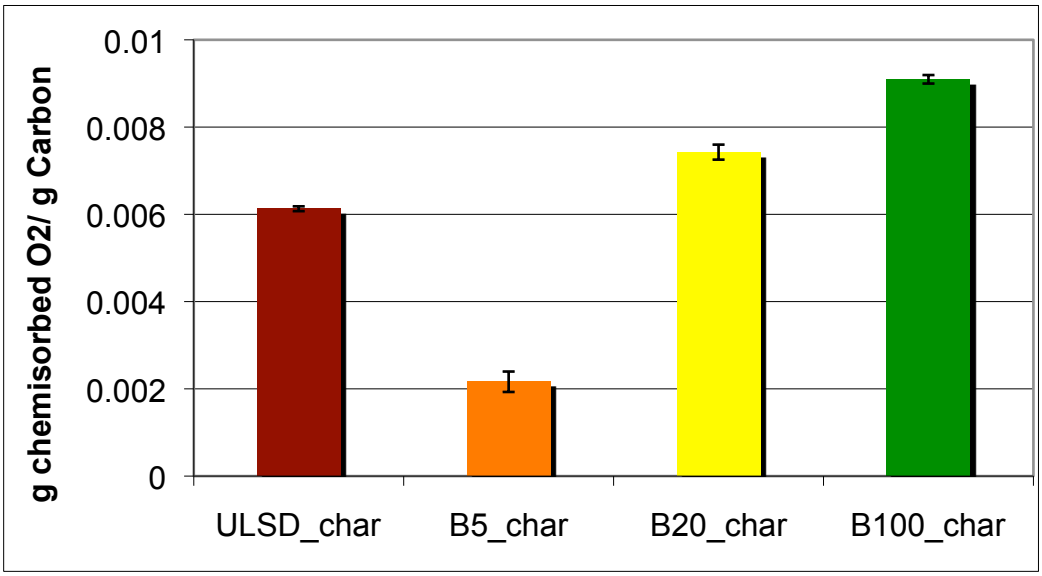

Figure A2-3 Oxygen chemisorption for PM fixed carbon samples.

8.2.3 A2.3 Nanostructure of biodiesel blends

Particulates from B5, seem to be much smaller and have evidence of fullerenic nanostructure, with large and small shells evident. There are also areas of high density, marked by groups of 2 to 3 stacked extended graphitic lamella. The remaining nanostructure is disorganized carbon, consisting of short, randomly oriented graphene segments. Primary particles are on the order of 20-25 μm in diameter.

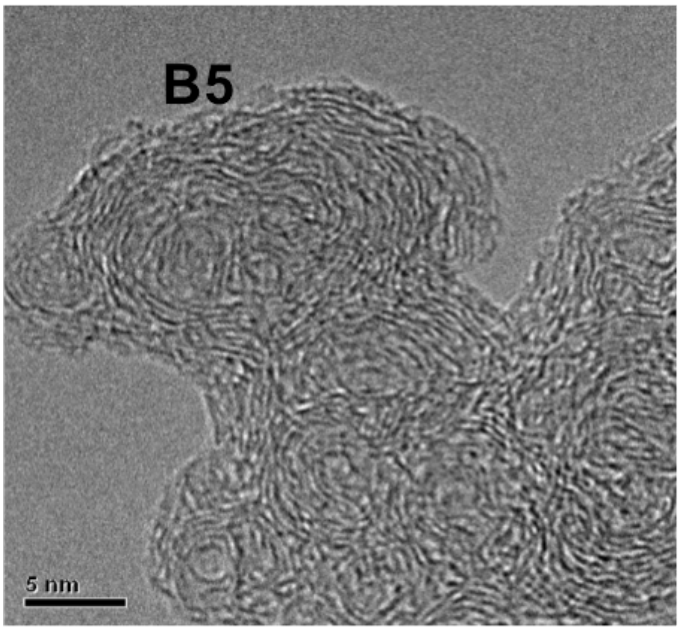

Figure A2-4 HR-TEM image of B5 PM.

Particulates from B20, have noticeably less fullerenic structures than B5 PM. Extended lamella are present, but with less frequency than in the B5 PM. The nanostructure has more tortuosity and less graphitic character than the B5 PM, however has not reverted to ULSD-like PM. The particle core consists of disorganized carbon. Primary particles are on the order of 25-30 μm in diameter.

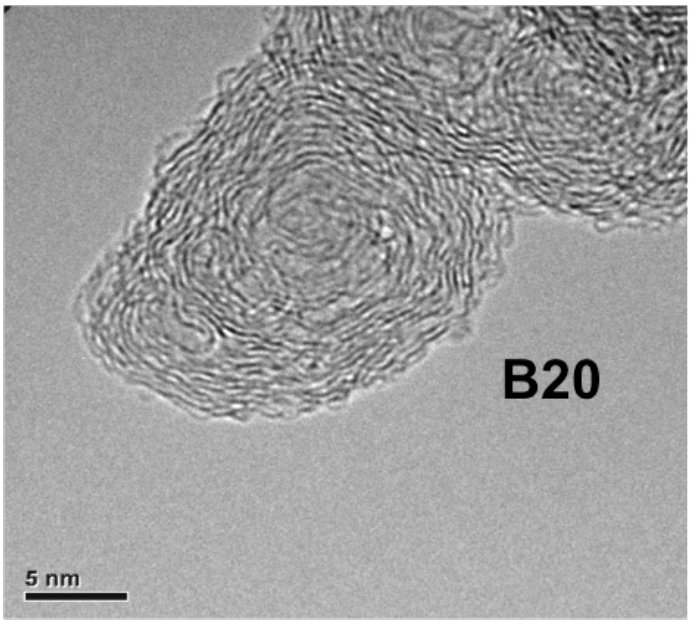

Figure A2-5 HR-TEM image of B20 PM.

8.2.4 A2.4 Speciation of SOF with Particulate Collection Location

Soluble organic species in the particulate extracts were individually identified by GCMS quantification, then grouped into polynuclear aromatic (PAH), methyl-ester and paraffin categories for comparison. Aromatics decreased with increasing biofuel blend level, and were noted to preferentially partition to the DPF particulate and gas phase. As expected, the paraffin fraction of the SOF decreased as the methyl ester fraction increased with biodiesel blend level, independent of sampling location. However, the level of methyl esters remained low in the gas phase until the as-fed fuel was pure biodiesel.

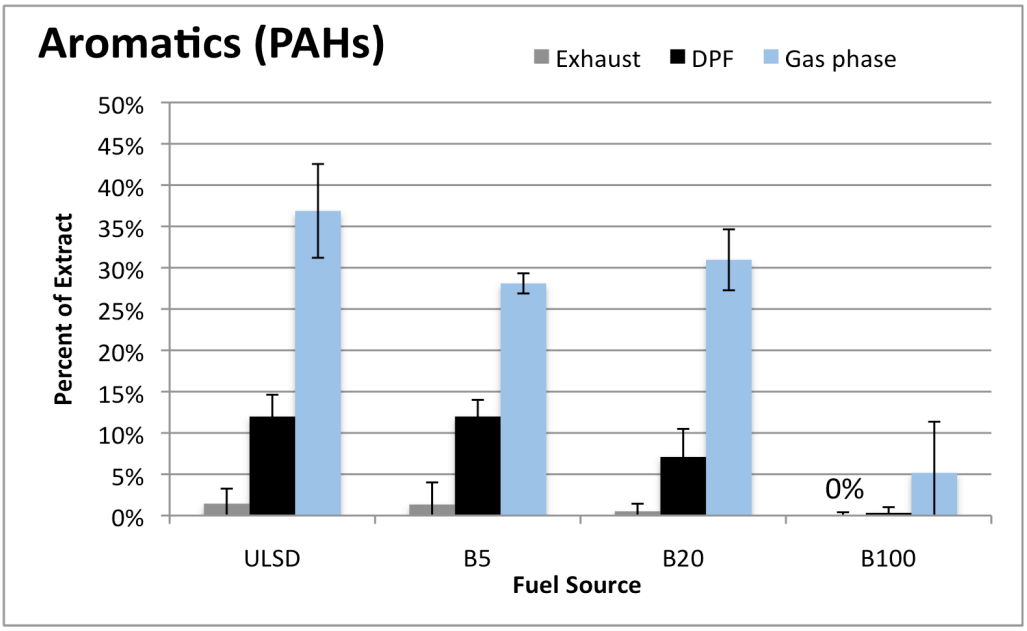

A. Aromatic fraction of extract with biodiesel blend level and sampling location.

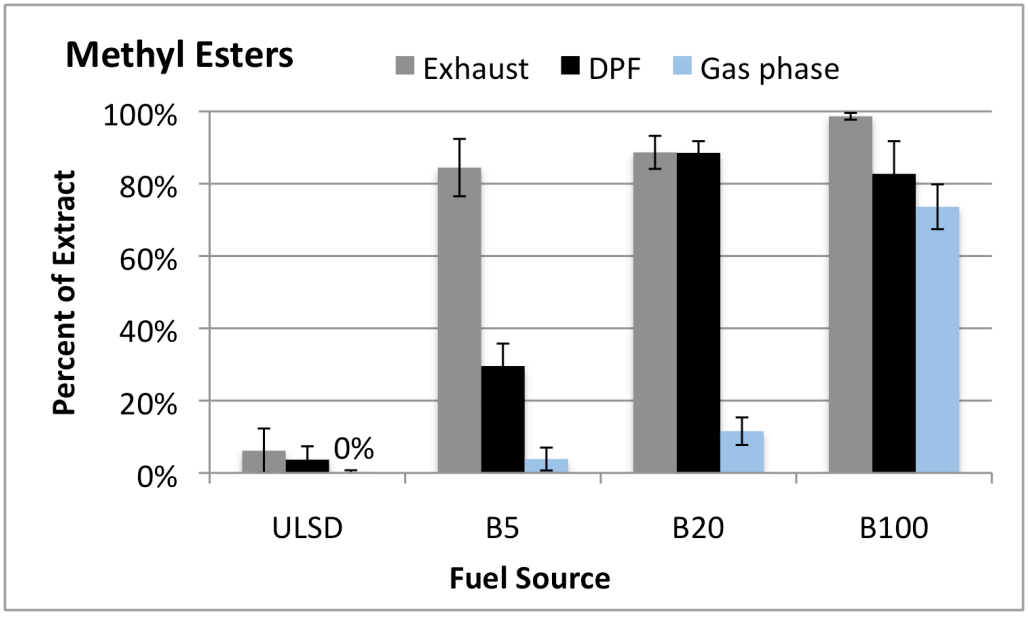

B. Methyl ester fraction of extract with biodiesel blend level and sampling location.

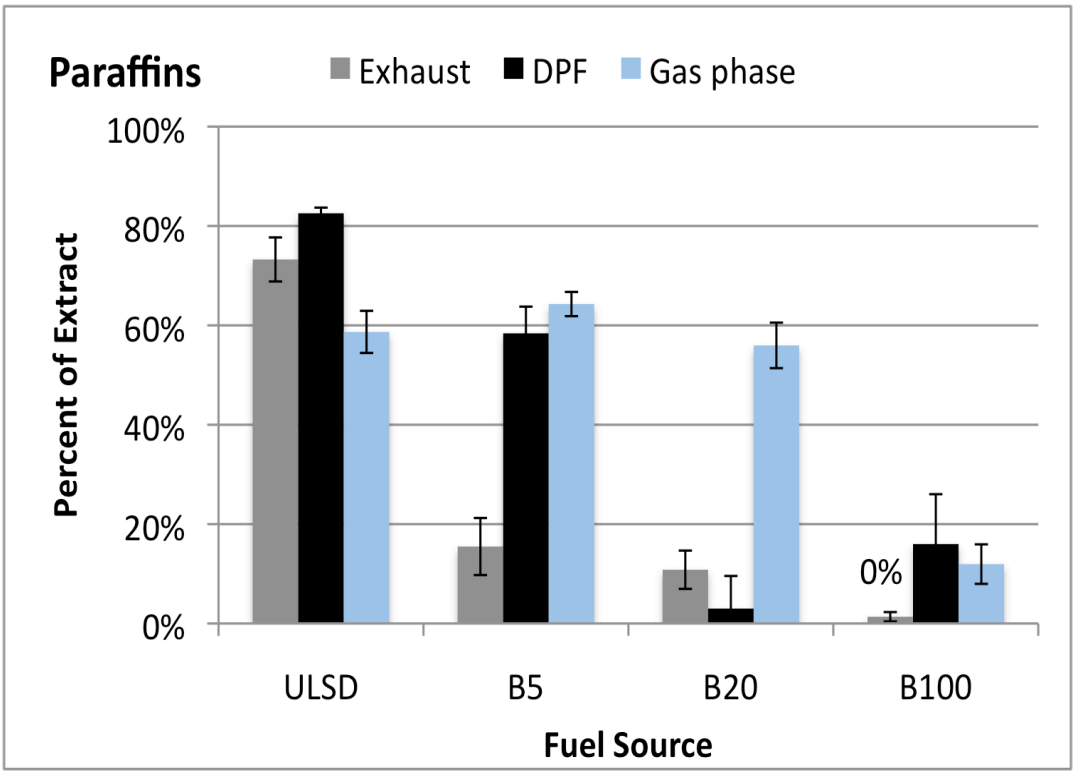

C. Paraffin fraction of extract with biodiesel blend level and sampling location.

A2-6 Partitioning of SOF extracts with biodiessel blend level.

Unexpectedly, the level of methyl ester in the SOF dramatically increased with only 5% volumetric addition of biofuel, indicating that the methyl esters survived combustion in a greater fraction than they appear in the fuel. We speculate that the small level of methyl ester contamination seen in the ULSD samples is likely due to methyl esters previously deposited in the system. The dilution tunnel was run at elevated temperatures with increased dilution air overnight between samples to minimize contamination.

Further examination of the paraffin fraction of the SOF revealed that the paraffin fraction, though equal for exhaust and DPF particulate, was speciated differently.

Exhaust particulate contained a higher percentage of light paraffins (defined as C19 or smaller), shown in **Error! Reference source not found.** and DPF particulate contained a higher percentage of heavy paraffins (C20 or greater), which would be more likely to deposit out onto the particulate at higher exhaust temperatures.

This difference in paraffinic content is likely noteworthy for particulate oxidation kinetics, where organic content is known to have a role [39]. Light paraffins are more likely to devolatilize from the particulate at lower temperatures, where as heavier paraffins will remain with the particulate solid. Also, the higher aromatic content in the DPF particulate organic fraction may have an impact on the initial light off temperature of the particulate. Therefore, assuming that the DPF organic content is the same as particulate from a traditional exhaust filter sample may lead to an underestimation of the oxidation of particulate in a DPF and perhaps runaway regeneration.

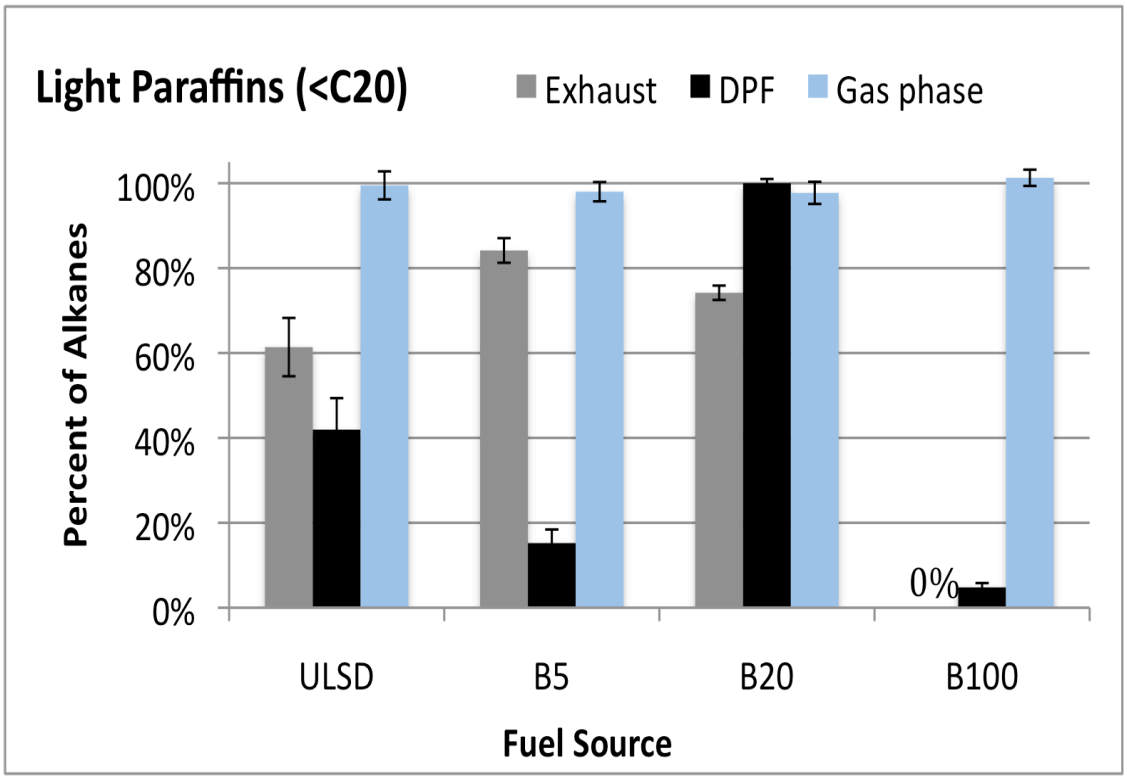

A. Fraction of paraffins C19 or smaller in the SOF extract with sampling location and biofuel blend level.

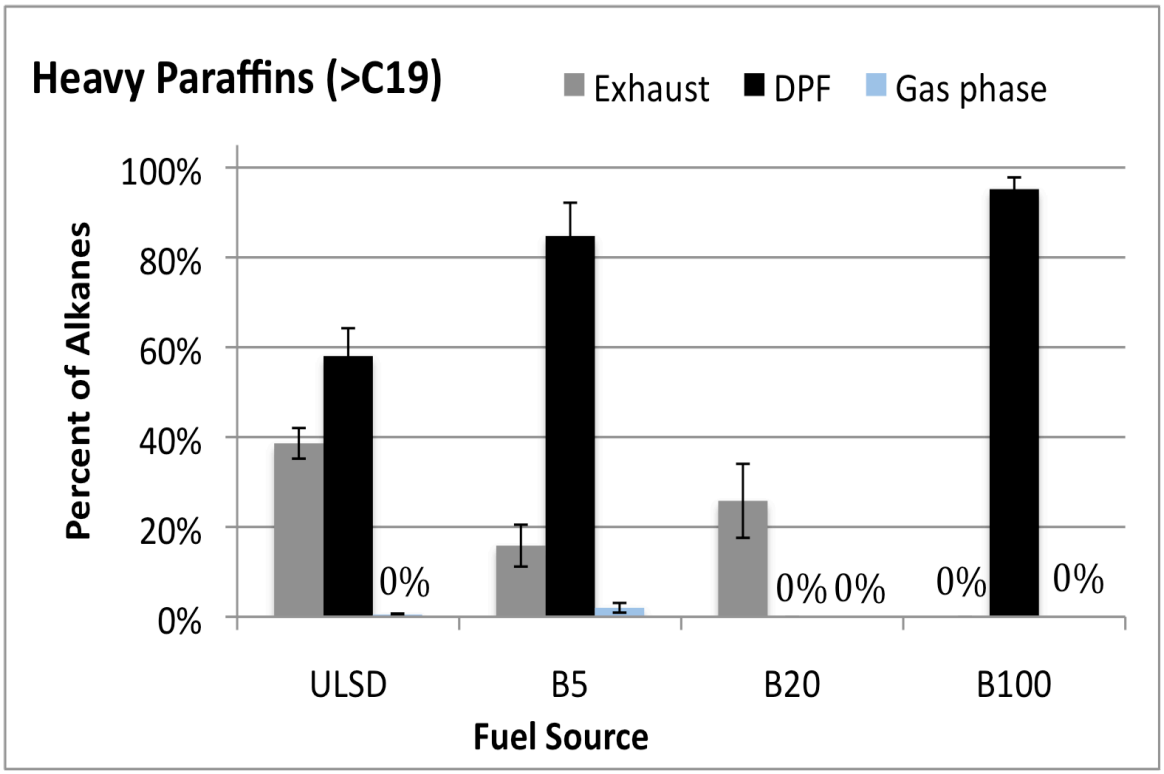

B. Fraction of paraffins C20 or larger in the SOF extract with sampling location and biofuel blend level.

A2-7 Light vs Heavy paraffin partitioning with sampling location.

In the above experiments, we found that fuel consumption and total exhaust hydrocarbons trended consistently higher and lower, respectively, with increasing biodiesel content. Increased fuel consumption is expected since the energy content of biodiesel is lower. Particulate and NOx emissions had more complicated trends with increasing biodiesel blending. Particulate emissions first increased and then decreased, and NOx first decreased and then increased.

As one might expect, the levels of methyl esters in particulate extracts and adsorbed exhaust gas increased with increasing biodiesel content in the fuel. Conversely, aromatic and paraffin levels (both light and heavy) declined in the particulates and exhaust gas with increasing biodiesel addition.

We found that DPF particulate appears to have higher fractions of heavy paraffins and aromatics compared to dilute exhaust particulate. This difference in paraffinic split may lead to different particulate oxidation characteristics, as light paraffins are more likely to devolatilized at low temperature, where as heavy paraffins will remain with the solid particulate particles. Thus it is important to recognize that dilute exhaust particulate samples may not give the most accurate estimates of particulate properties needed for DPF modeling.

8.2.5 The Effect of Inorganics

As a result of the TPO experiments, the presence of an inorganic fraction was noted in the B100 samples. A reddish powder was found to remain after the particulate sample had fully oxidized. 100 mg samples of ULSD, B5, B20 and B100 particulate were oxidized in a tube furnace in ceramic crucibles. The inorganic fraction remaining was investigated by XRD and found to be mainly inorganic metal oxides, including cordierite, the material that the DPF is made from.

Fuel Source of PM	ULSD	B5	B20	B100
Mass fraction inorganics in 100 mg PM	trace	trace	2.7%	5.1%

Table A2-1 Mass fraction inorganics in 100mg PM.

It was suggested that the impact of the biofuel on oxidation kinetics was not due to the fuel source, but rather the inorganic content as metal oxides are known to catalyze carbon oxidation [Essenhigh, 1981]. In order to examine the impact of the inorganic residue, 250mg of B100 particulate was oxidized by air in a tube furnace to generate 13.1mg inorganic residue. 0.0135g of ULSD particulate was mechanically mixed with 0.006g inorganic residue and prepared for TPO.

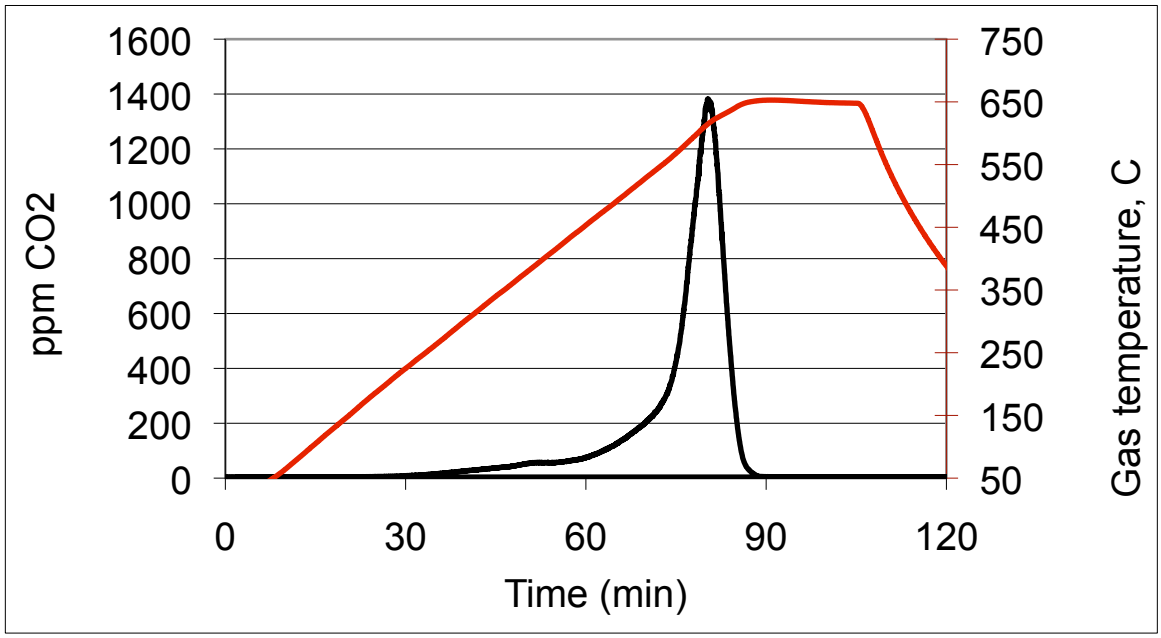

Figure A2-8 Carbon dioxide evolution with time and temperature for 30wt% inorganic residue in ULSD PM TPO.

The TPO results for a ULSD particulate sample with no residue, ULSD particulate sample with 30 wt% residue and B100 particulate sample (with nascent 5.1% residue) were compared in the following figure. No difference is seen between the conversion temperatures in ULSD particulate samples, regardless of the level of inorganic content.

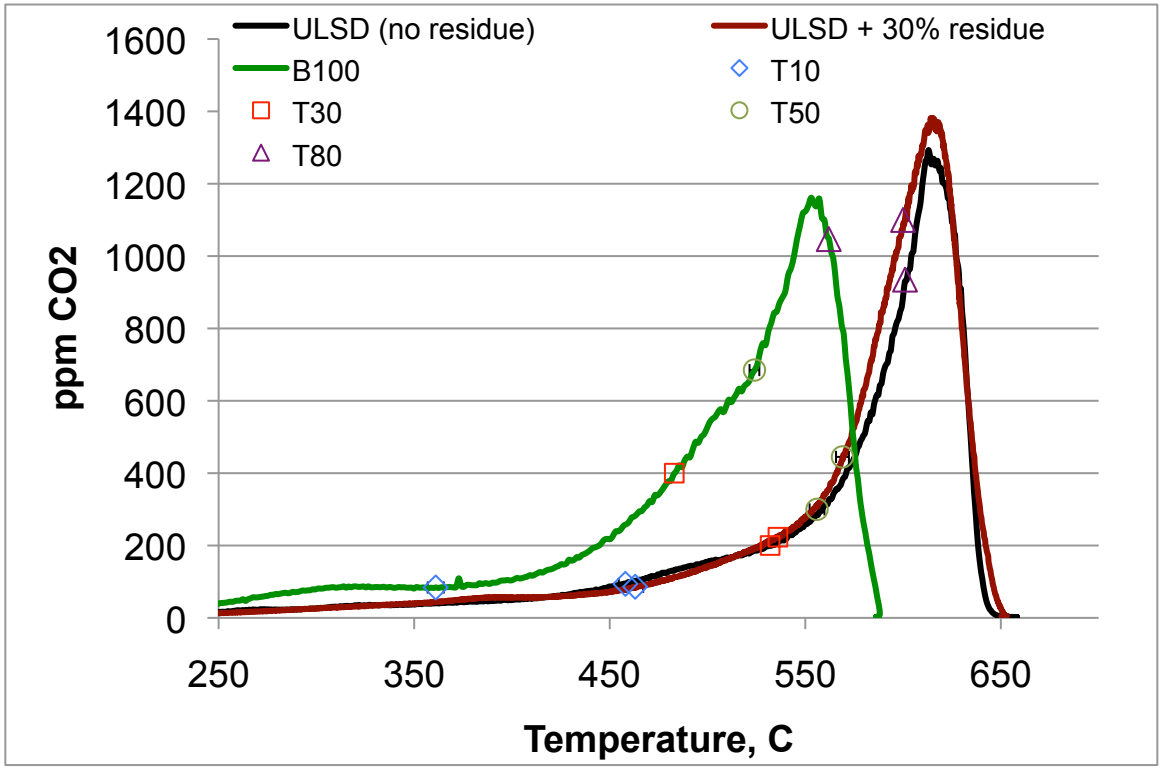

Figure A2-9 Comparison of TPO traces for ULSD particulate with and without inorganic residue and B100 particulate, which has 5.1% residue in its nascent state.

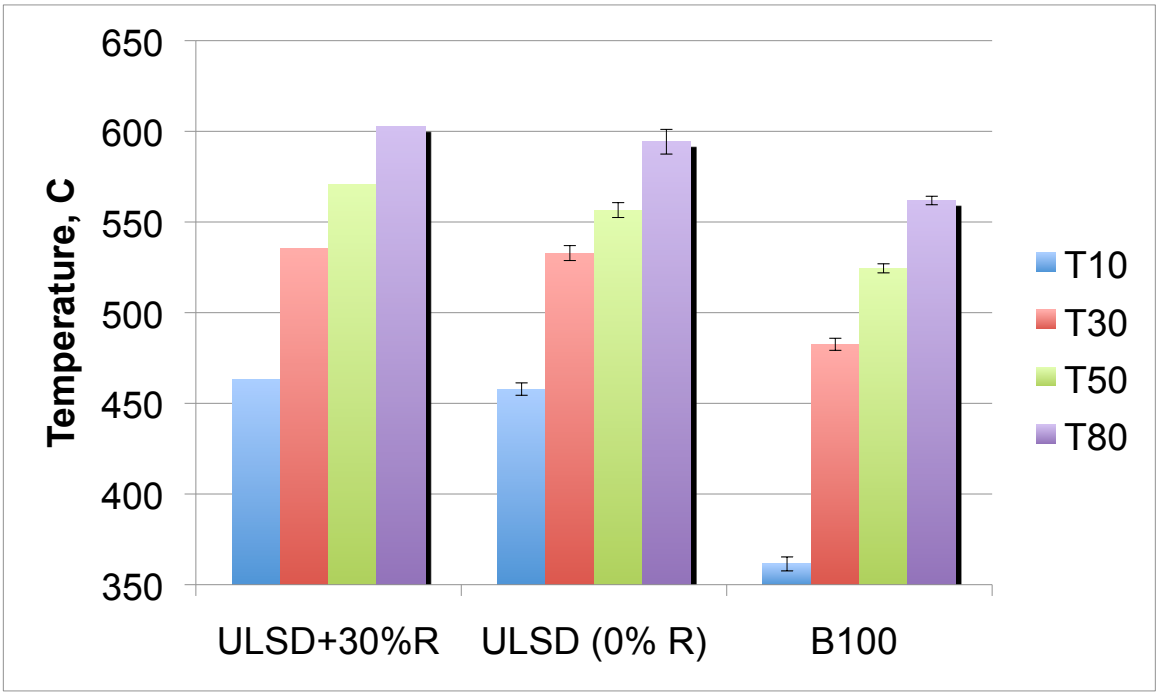

Figure A2-10 Comparison of 10% (T10), 30% (T30), 50% (T50) and 80% (T80) burnout temperatures for ULSD particulate with and without inorganic residue and B100 particulate (with nascent 5.1% residue)

The figures show that there is no difference seen in the oxidation behavior of the ULSD particulate with the addition of the inorganic residue. Therefore, it was concluded that the presence of the inorganic fraction was not responsible for the oxidative advantage of the biodiesel particulate.

8.2.6 DPF Degradation

The inorganic fraction found in the biodiesel particulate discussed in the previous section was determined (by XRD) to contain cordierite, the material of construction for

the DPFs. The DPFs used in the collection of the particulate samples were removed from their cans for further investigation.

Each filter had been employed for 24 hours of engine operation in order to collect the particulate samples investigated in this work. The filters were installed in the exhaust line in a typical under-body style, mimicking their placement on a vehicle. The particulate samples were removed from the DPFs by back-flushing with pressurized air.

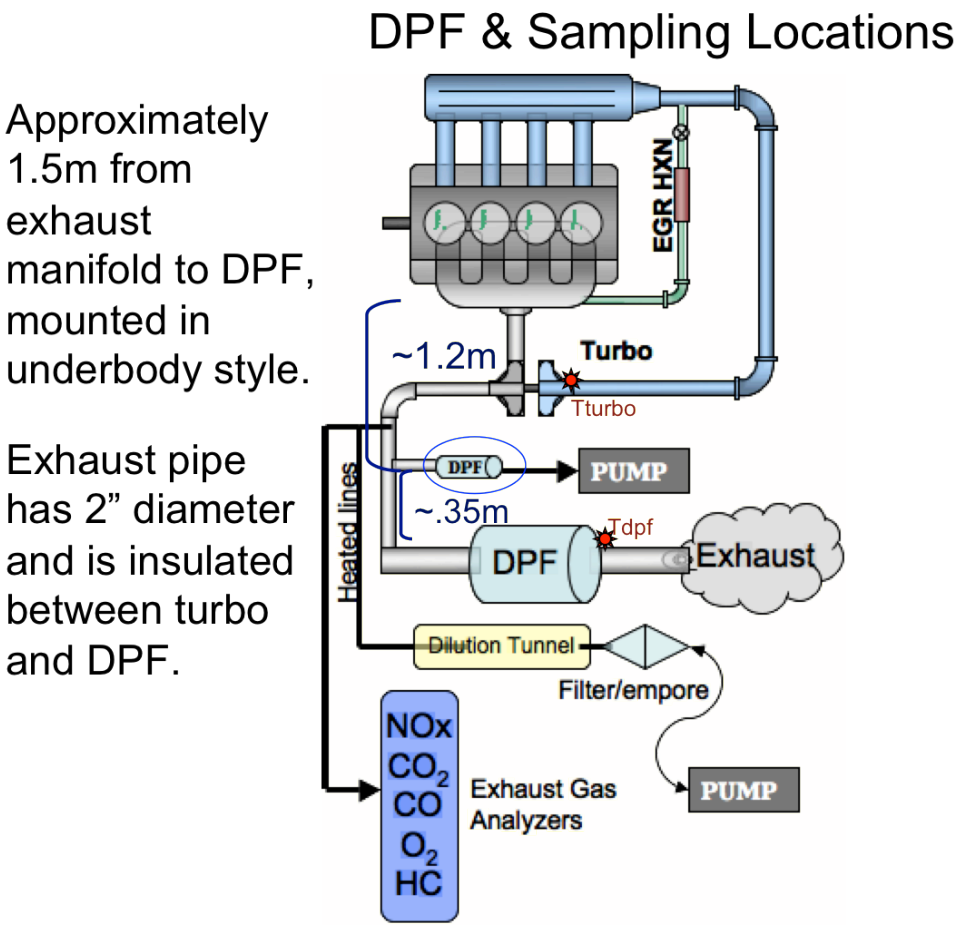

Figure A2-11 DPF position and sampling locations relative to the engine.

When the filters were uncanned, we were surprised to see erosion of the B100 and B20 substrates from the 1500 rpm condition.

Exposed Filters from 1999 Euro2 1.7L Mercedes Diesel

Fuel Type	ULSD	B20	B100	B100
speed(rpm)-IMEP(bar)-%load (factory calibration)	1500, 2.6, 25%	1500, 2.6, 25%	1500, 2.6, 25%	2300, 4.2,
total exposure time*	12h (07) + 12h (08)	12h (07) + 12h (08)	12h (07) + 12h (08)	5h (07) + 5h (08)
THCs (ppm)	197	171	170	140
NOx (ppm)	126	88	145	162
FSN	1.37	0.96	0.3	.58
Turbo out T (C)	238	240	247	315
DPF exit T (C)	210	207	210	290
miniDPF T (C)	207	205	206	285
Burn out residue in 100mg '07 soot (5.66" DPF)	0mg	2.5mg	5.7mg	N/A
extract pH (1"x3" DPFs)	6.5	3.7	3	N/A
Last run date	3/5/08	3/14/08	5/7/08	5/8/08
uncanned	6/08	6/08	5/14/08	6/08

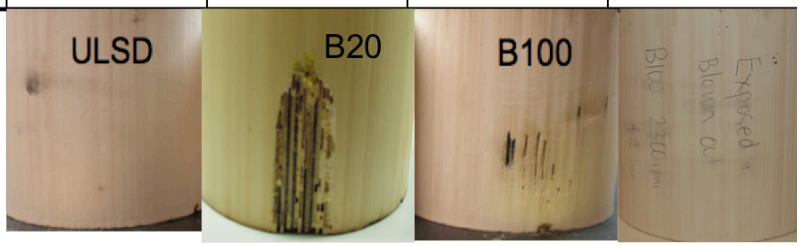

Figure A2-12 Summary of experiments for DPF exposures.

It is hypothesized that the damage to the filters is due to acidic condensate that is held against the filter material by the intumescent matting material. Cordierite is a know acid-sensitive material. The damage to the B20 filter was by far the most severe, and we hypothesize that is due to the extended storage time of the filter.

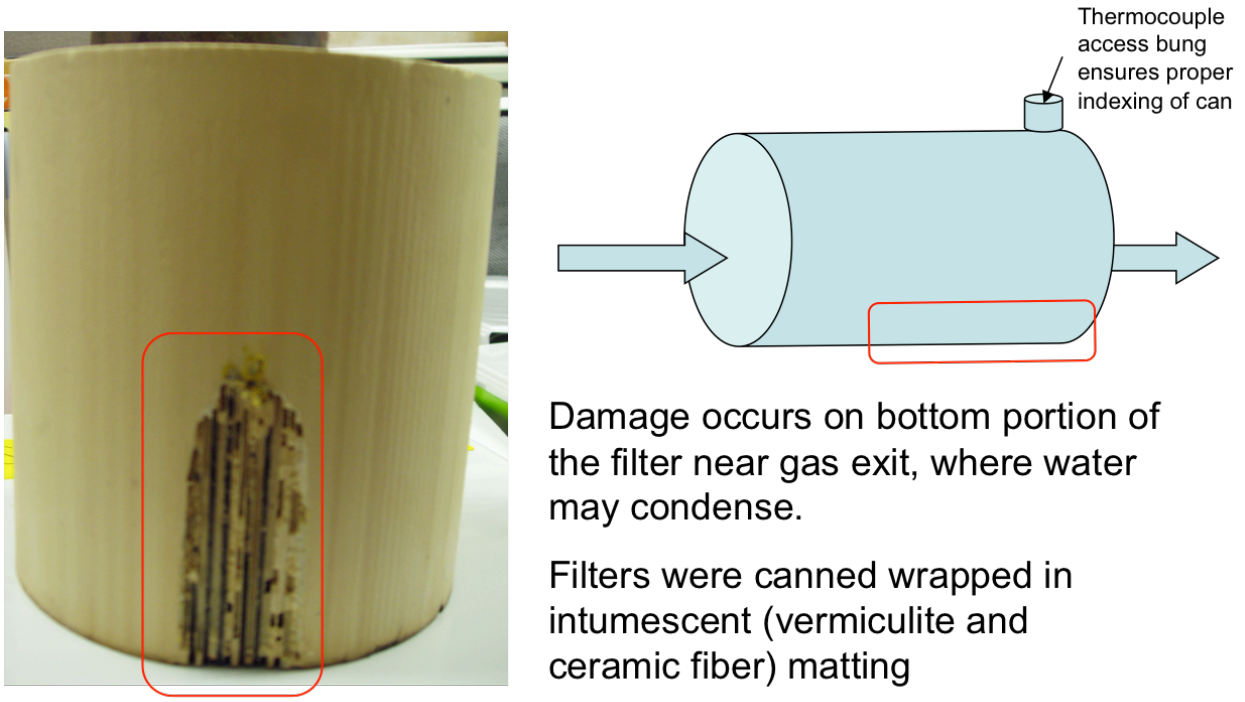

Figure A2-13 Close-up of DPF used with B20 fuel which was stored for several weeks before being uncanned.

Further investigation into the exact cause or mechanism of degradation is ongoing.

8.3 Appendix 3: Neutron Imaging of Diesel Particulate Filters

This work presents nondestructive neutron computed tomography (nCT) measurements of Diesel Particulate Filters (DPFs) as a method to measure ash and soot loading in the filters. Uncatalyzed and unwashcoated 200cpsi cordierite DPFs exposed to 100% biodiesel (B100) exhaust and conventional ultra low sulfur 2007 certification diesel (ULSD) exhaust at one speed-load point (1500 rpm, 2.6 bar BMEP) are compared to a brand new (never exposed) filter. Precise structural information about the substrate as well as an attempt to quantify soot and ash loading in the channel of the DPF illustrates the potential strength of the neutron imaging technique.

8.3.1 3.1 Introduction

Though many emissions regulations are currently deployed, diesel technology continues to be regulatory-driven as emissions standards become increasingly strict in 2010 and beyond. Diesel Particulate Filters (DPFs) have seen widespread use for removing particulate emissions from diesel exhaust. Soot and ash (non-regenerable materials from the lubricating oil) accumulation in the filter causes the exhaust flow to be restricted and an unfavorable backpressure to form on the engine, disrupting optimal engine performance, leading to a drop in fuel efficiency. To minimize the penalty on the engine, the DPF is periodically regenerated, burning out the stored soot. However, the ash remains, leading to plugging of the channels over time, negatively affecting engine and DPF performance and limiting the useful lifetime of the DPF [96, 97].

Determining the soot and ash loading in the channels of a DPF is critical to improving the performance, efficiency and longevity of the device. EPA regulations currently require manufacturers to warrant DPFs for no less than 150k miles (240k km) [98].

Past studies of soot loading and ash deposition in DPFs have been done with techniques that require the destruction of the substrate. Transmission electron microscopy (TEM) imaging of a soot- or ash-loaded DPF segment requires the soot cake first be immobilized with epoxy before the filter is cut into sections for imaging [99-103]. Nondestructive X- ray imaging has also been done, however with limited success, as the X-ray detector did not provide enough contrast or resolution to obtain sufficiently detailed images [104].

Previous thermal neutron imaging studies [105-108] have shown promise for the capability of neutron radiography to visualize soot distribution in DPFs. Considering the differences in volatile content on biodiesel soot and the increased ash loading due to biodiesel dilution of the lubricating oil, it was deemed interesting to attempt to compare soot loadings and ash content with fuel type.

8.3.2 Basic Principles of Neutron Imaging

Neutron imaging [109] is a nondestructive, noninvasive technique that is complementary to other imaging techniques such as X-ray or gamma imaging. Due to the interaction properties of neutrons with matter, some light nuclei such

as H and D greatly scatter neutrons whereas some heavier elements such as Cu and Pb do not strongly interact with neutrons and can therefore be easily penetrated. Figure A3-1 displays a simplistic set-up of a tomographic imaging facility with the source, the collimation system for the neutron beam, and the sample in front of the detector.

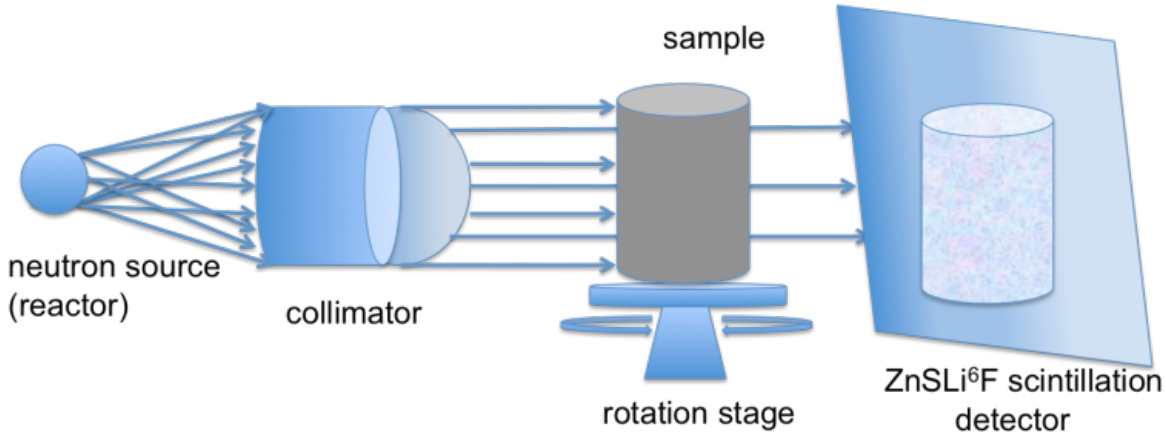

A3-1 Schematic representation of neutron imaging setup.

The attenuation of the beam is caused by absorption and scattering within a sample. The intensity of the transmitted neutron beam, as a function of wavelength λ, measured at the detector position is given by

$$I(\lambda) = I_0(\lambda) \cdot \exp(-\mu(\lambda) \cdot \Delta x) \qquad \text{Equation 8-1}$$

where I_0 and I are, respectively, the incident and transmitted beam intensities, μ is the attenuation coefficient and Δx is the thickness of the sample. The attenuation coefficient μ is given by

$$\mu(\lambda) = \sigma_t(\lambda) \cdot \frac{\rho N_A}{M} \qquad \text{Equation 8-2}$$

where $\sigma_t(\lambda)$ is the material's total (i.e., scattering and absorption) cross section for neutrons, ρ is its density, N_A is Avogadro's number, and M is the molar mass.

Several bare (unwashcoated, uncatalyzed) 5.66" × 6" (143.8 × 152.4 mm) NGK558 HoneyCeram cordierite DPFs were purchased from NGK Automotive Ceramics (Novi, MI) and matted and canned by CLEAIRE Advanced Emission Controls (San Leandro, CA).

Two fuels were considered in this study. Soy Gold, a trans-esterified soy methylester biodiesel (B100) was purchased from Ag Processing Inc. (Omaha, NE). 2007 Ultra Low Sulfur Diesel (ULSD) Certification Fuel purchased from Chevron Phillips Specialty Chemical Company (The Woodlands, TX).

Soot samples were generated in a 1999 1.7L Mercedes Benz direct-injection common rail diesel engine [35, 74] as shown in Error! Reference source not found. at 1500rpm, 2.6 bar BMEP.

The B100 DPF (separate filter used for each fuel) was mounted under-body configuration in the exhaust line and loaded on engine for 12 hours, before being removed and back flushed with pressurized air to remove the majority of the soot cake (which was collected for other experiments) from the filter, leaving only wall-loaded soot.

The ULSD DPF was run in the same manner as the B100 DPF, but then loaded again at 1500 rpm, 2.6 bar BMEP for 4 hours, so that it also has a soot cake. Approximately 9.2 g of soot was loaded into the filter, for a loading of 1.5 g/L.

The DPFs were then removed from their cans and shipped, along with a never-used filter, to the FRM-II ANTARES facility [12] (Muenchen, Germany) for neutron imaging analysis.

8.3.3 Experimental Setup & Facility

DPFs were imaged at the ANTARES neutron imaging facility of the Forschungs-Neutronenquelle Heinz Maier-Leibnitz (FRM II) at the Technische Universitaet Muenchen (TUM). The 20 MW FRM II nuclear reactor produces a flux of 8×10^{14} n/cm^2-s, delivering approximately 10^8 n/cm^2-s for a collimation ratio of 400 of thermal neutrons to the ANTARES imaging facility. The maximum collimation ratio is 800 (~ 2.6×10^7 n/cm^2-s). The detector is equipped with a ZnS/Li^{6}F scintillator, which converts neutrons into light. The light is reflected off a mirror and is then focused into an ANDOR CCD camera, as illustrated in Figure A3-2. The spatial resolution of the detector was 50 microns.

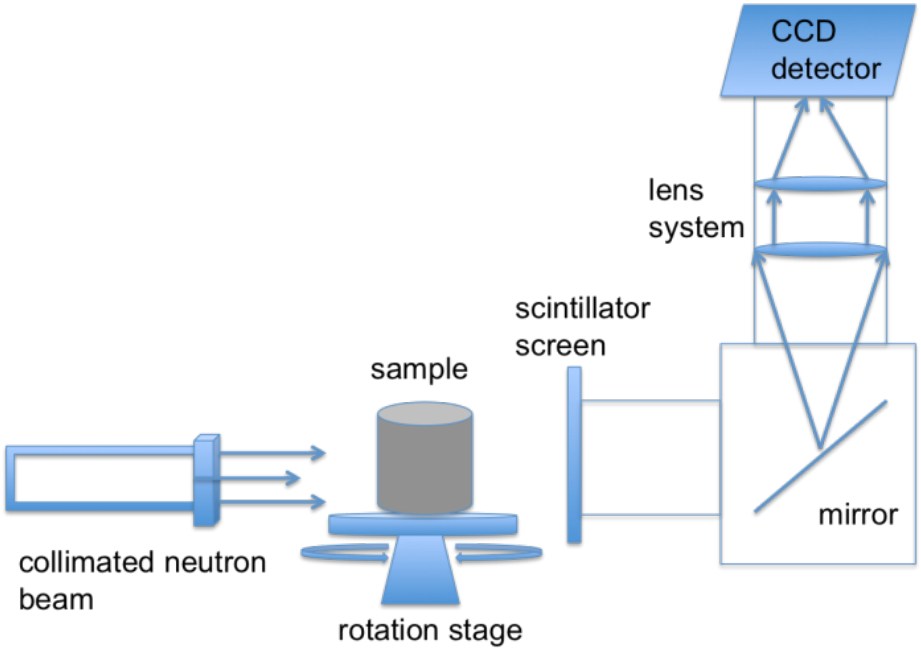

Figure A3-2 Diagram of the neutron detection system at ANTARES.

8.3.4 Neutron Computed Tomography

Neutron computed tomography (nCT) is a technique consisting of the acquisition of a series of 2D radiographs or projections of the same sample at different angles by rotating the sample relative to the source (illustrated in Figure A3-3) around a single axis of rotation. These radiographs consist of a 2D shadow image of a 3D object, an example of which is shown in Figure A3-3. Two coordinate systems are usually defined: the sample coordinate system (x, y) rotated by an angle θ with respect to the fixed detector system (s, t). Assuming the beam geometry is parallel, a projection $P_\theta(t)$ is defined as:

$$P_\theta(t) = \int \mu(x,y)ds \qquad \text{Equation 8-3}$$

and the set of all projections is called the Radon transform of the 2D neutron attenuation (absorption or scattering) function μ(x, y) of the sample.

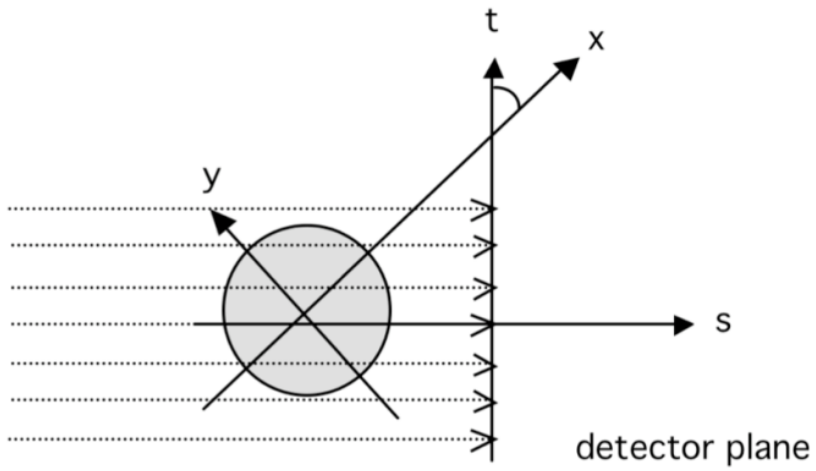

Figure A3-3 Projections acquired at the detector plane for different angles in a parallel beam geometry. Neutrons are coming from the left and are detected on a 2-D plane on axis t.

The projections $P_\theta(t)$ are called sinograms. Inverse Radon transformation is necessary before algorithms such as inverse Fourier transformation or filtered back projection can be used to virtually reconstruct the object from these 2D slices.

For example, the Fourier method implies the transformation of the projections into the Fourier space. In this space, the projections define a portion of the object. The full Fourier transform is obtained by interpolation between successive projections, after which a reverse Fourier transform is executed yielding the reconstruction of the object's 3D structure. A unique reconstruction from the object is achieved if the sampling frequency is twice as high as the highest frequency in the Fourier-transformed image,

as enunciated by Shannon's theorem. CT fundamentals are explained in [110]. Several software programs have been developed to automate this process including Octopus [111], used in this work.

8.3.5 Experimental Results

This section displays neutron computed tomography (nCT) reconstructions of cordierite DPFs exposed to 100% biodiesel (B100) and ultra low sulfur diesel (ULSD) at one speed-load point (1500 rpm, 2.6 bar BMEP) as compared to a brand new filter (New).

Figure A3-4 displays a normalized neutron radiograph of the filter run with B100 fuel. The channels and plug lengths are clearly identifiable and provide complementary information to previous X-ray measurements [104]. For each filter, 800 projections were measured with a rotation step of 0.45 degrees. These projections were first normalized then reconstructed using Octopus. Each computed tomography (CT) image represents a slice taken perpendicularly to the axis of rotation, i.e. to the channels. There are approximately 1800 slices per 154 mm tall filter.

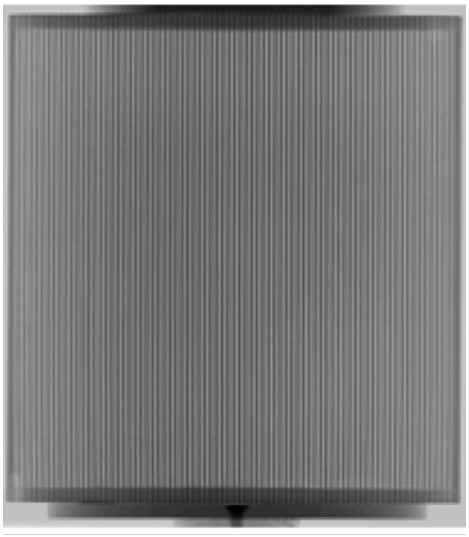

Figure A3-4 Representative radiograph of the B100 filter.

Figure A3-5 illustrates one CT slice of the ULSD filter, approximately half way through the height of the filter. Soot deposition can be seen on the walls.

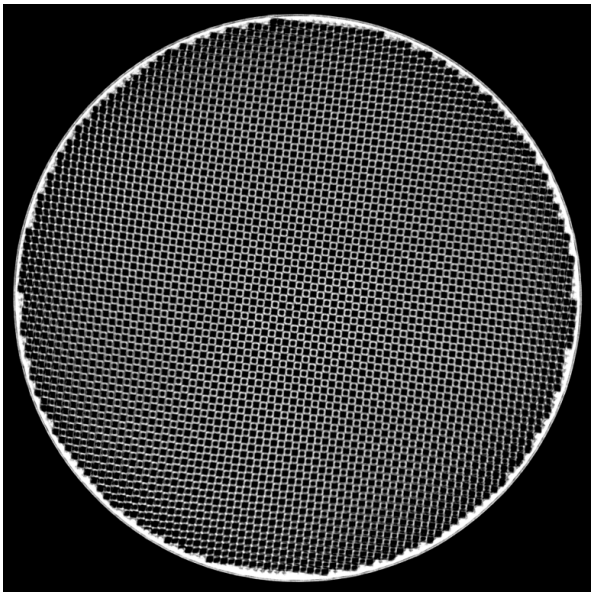

Figure A3-5 Computed tomography slice of the ULSD filter at half axial length.

Figure A3-6 shows zoomed-in nCT slices of the New, ULSD and B100 filters. Sections are at the radial center of the filter at approximately half of the axial length. The New filter has perfectly square channels, whereas in the ULSD and B100 filters, there is systematic alternation of rounded and squared channels. The rounded channels have soot deposited in them whereas the squared ones do not. This alternating pattern can be explained by the honeycomb structure of the DPF, which has alternately plugged channels, so that the gas enters through one channel, passes through the porous walls, trapping the soot, and exits through the neighboring channels. The soot deposits have H-rich (hydrocarbons mainly with a small amount moisture) material associated with them, and therefore have a higher contrast since neutrons are very sensitive to light atoms such as H. This illustrates the capability of neutrons in detecting small amounts of soot on the walls of the filter.

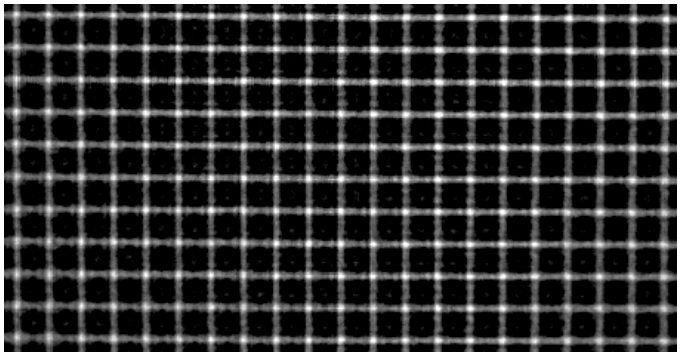

(A) New Filter

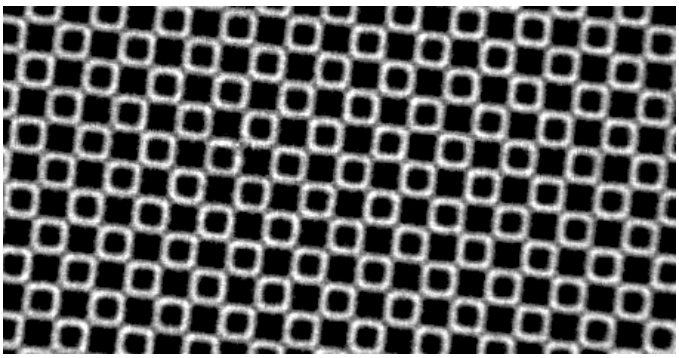

(B) ULSD Filter (zoom in of Figure 6)

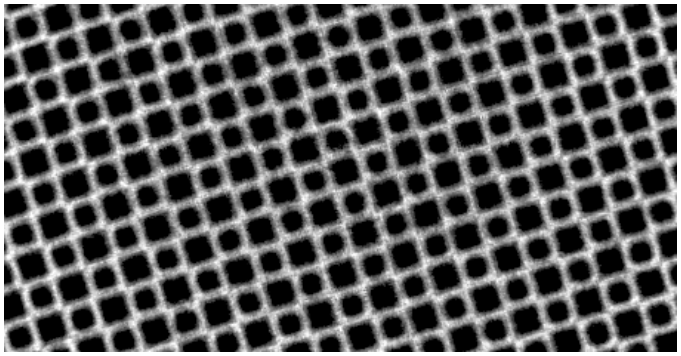

(C) B100 Filter.

Figure A3-6 Filter Sections.

Ash is mainly comprised of metal oxides and lubricant additives, including ppm levels of boron [112]. Neutrons are highly sensitive to boron, which we believe is responsible for the 'glowing particles' seen in Figure A3-7, a slice of the B100 filter at the outlet end, just before the plugs. These 'glowing particles' occur predominantly at the outlet end of the filters and have a much brighter intensity than soot. Additional experiments are being done to validate identification of the ash.

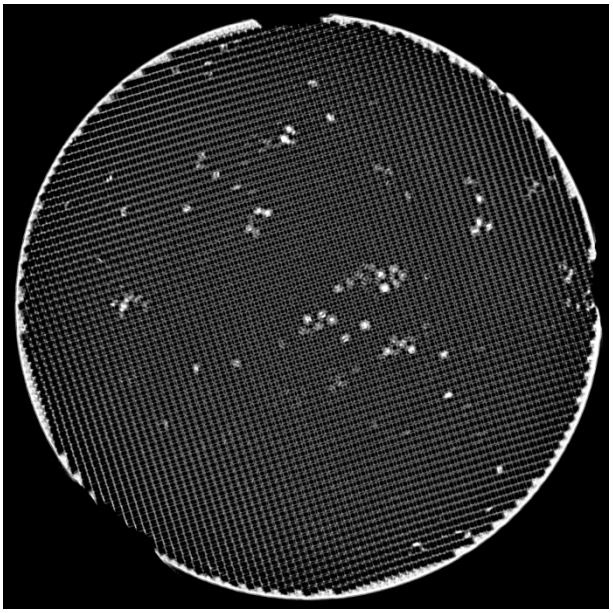

Figure A3-7 nCT Reconstruction of the B100 filter at the outlet, just before the plugs, showing ash deposits as bright spots.

These preliminary images show great promise in being able to detect small amounts of soot and/or ash deposition in DPFs.

8.3.6 Image Processing and Quantification of Soot Deposits

Various methods for processing the nCT images may be used to investigate the sample. Three-dimensional models can be created using visualization software (such as VGStudioMax, Amira, or VisIT), as shown in Figure A3-8.. This type of 3D model allows the sample to be interrogated from multiple angles and allows for the creation of a 'fly-through' movie of the sample, similar to a CAD program.

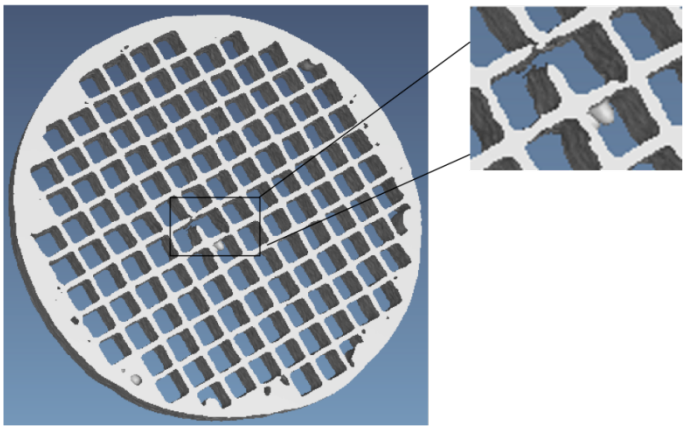

Figure A3-8 3-D Reconstruction of ~20 filter slices of a 1"×3" DPF using a trial version of VGStudioMax.

Quantification of filter wall thickness, used as an indicator of soot deposition, was accomplished using the Image Analysis Toolbox in Matlab. The nCT images were loaded into Matlab and rotated to achieve a square orientation. The ULSD images and B100 images had to be rotated by +6.87 degrees and -17 degrees counterclockwise respectively. The new filter was not rotated.

A 5×5 channel grid in the dead center of the filter was defined for analysis. Horizontal and vertical indices were defined for the filter as seen in Figure A3-9. Intensity profiles were then computed for each slice in the defined filter segment.

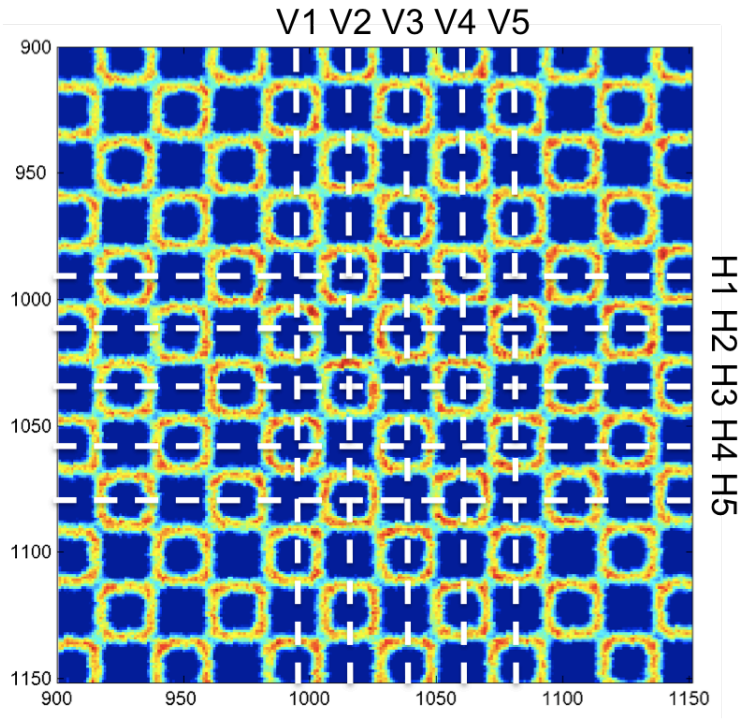

Figure A3-9 ULSD nCT slice with grid to define indices for intensity measurements. Units are pixels.

The apparent wall thickness was calculated by the peak width at a set threshold value (intensity = 1000), as seen in Figure A3-10. The true width is likely better represented by the width of the base of the peak, but due to artifacts in the data, thresholding was used until more sophisticated analysis routines are developed. Fifty wall thickness values per slice were calculated.

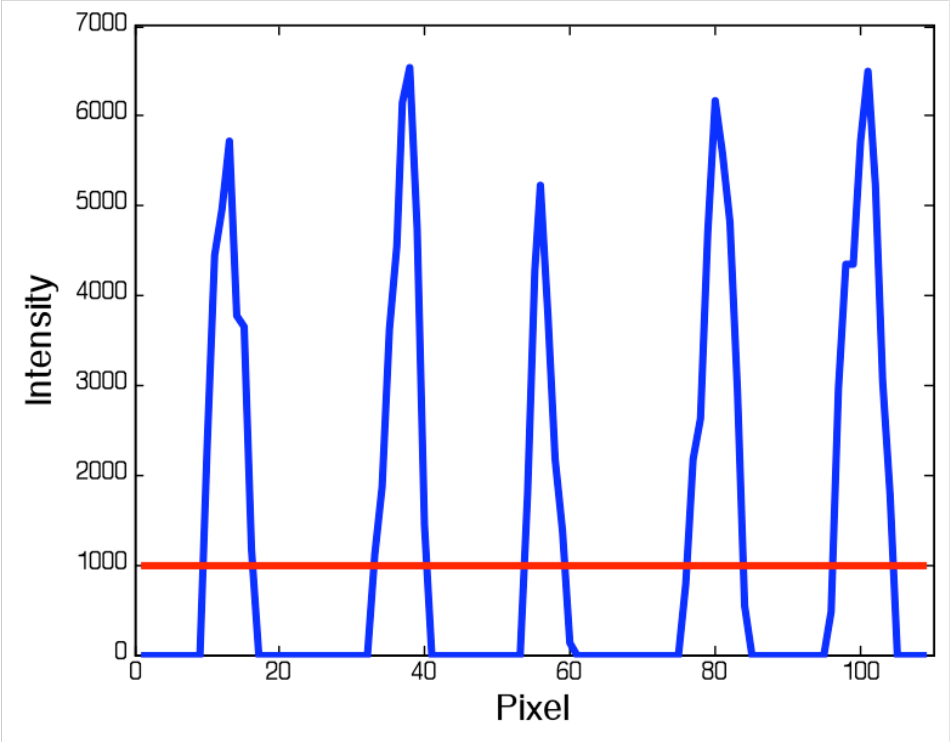

Figure A3-10 Example intensity profile for five walls.

The threshold value was chosen to avoid mistaking image artifacts as walls. This was primarily an issue for the New and B100 filters, which had some ghosting at the top and bottom of the reconstructed filter – which may be due to improper alignment of the sample in the neutron beamline and exacerbated by the reconstruction software. An example of the artifacts is shown in Figure A3-11. Due to these artifacts, which predominantly occurred in the bottom quarters of the B100 filter and the top third of the New filter, the full axial profile of the New and B100 filters could not be calculated with confidence.

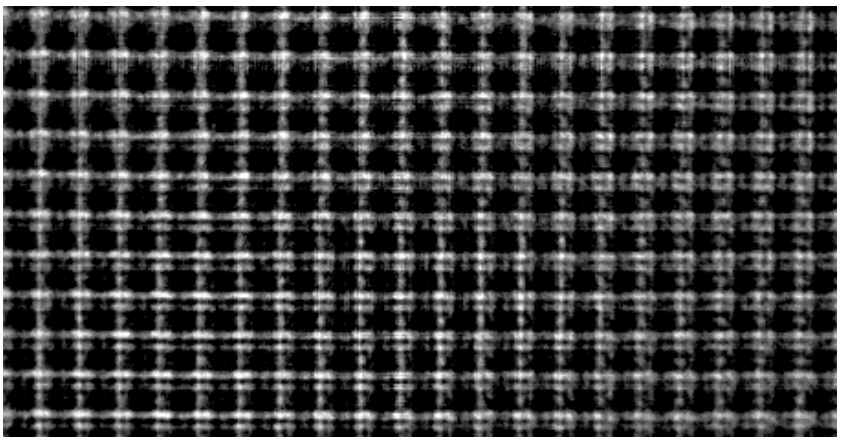

Figure A3-11 nCT of New filter, near the top. Image has artifacts introduced by sample alignment or reconstruction imperfections.

A Matlab script was used to process the images. The script excluded a slice if less than 50 wall widths, caused by improper threshold, were calculated. The top and bottom five widths were discarded and a mean apparent wall width for each slice (representative of an axial position in the filter) was calculated over 40 measurements. The measurements were then converted from pixels and slice numbers to spatial dimensions allowing calculation of the axial profile of the wall widths as shown in Figure A3-12. In the figure, gas flow is from left to right, with the DPF inlet being at 0mm.

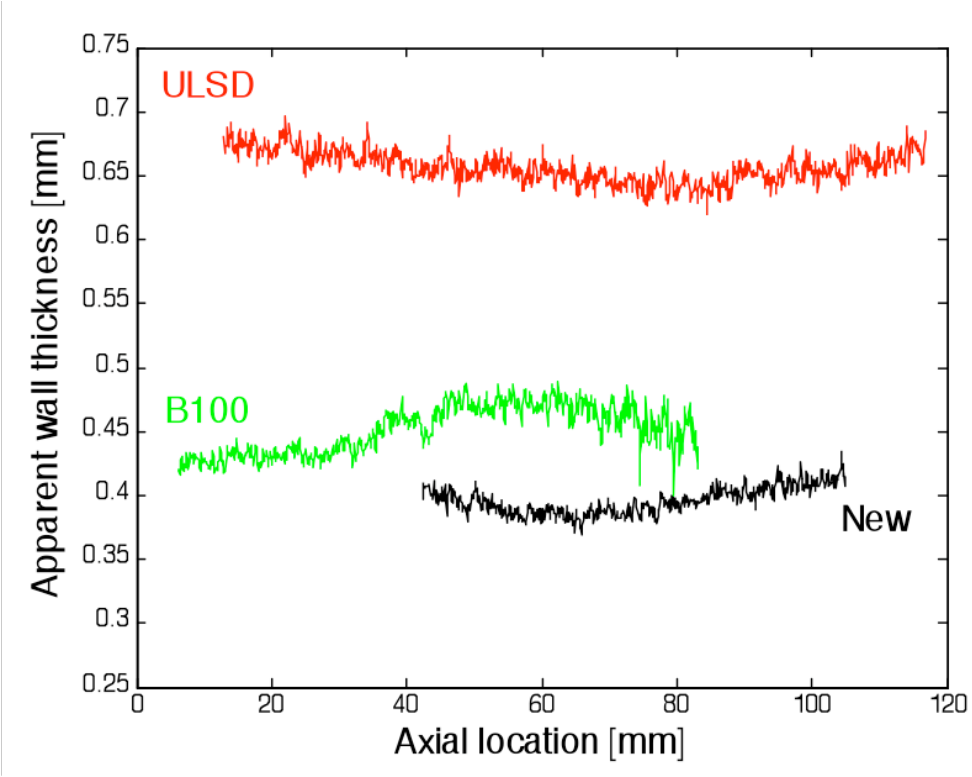

Figure A3-12 Axial apparent wall thickness profiles for ULSD, B100 and New filters.

From these profiles, the average wall thickness for the New filter was approximately 400 microns. The B100 filter, which had previously been soot loaded before soot was back flushed out of the filter, had an apparent wall thickness of approximately 435 microns in the first third of the filter, which grew to about 450 microns as the axial distance progresses towards the center of the filter. This may imply that the soot loading on the walls is thicker at the outlet end of the channels in this filter. The average apparent wall thickness in the ULSD filter is approximately 680 microns. In this

case, since the filter was soot-loaded, this likely means that the soot was evenly deposited in the axial direction, with a cake thickness of 280 microns.

8.3.7 Conclusions

Neutron imaging provides unprecedented detailed information on DPFs in a non-destructive fashion. Neutrons are sensitive to light atoms such as H and therefore can detect small amounts of H-rich material (i.e. trapped moisture or hydrocarbons in soot) or neutron absorbers, like boron in the ash, allowing small amount of residue deposition visible.

Neutron computed tomography can detect small amounts of soot and/or ash deposition in the walls of a filter. From these computed images, quantification of soot or ash loading can be done, and axial (and radial) soot deposition profiles can be mapped.

In this work, three DPFs — one run (then back flushed to remove the soot cake) with B100, one lightly loaded (1.8 g/L) with ULSD soot, and an unused, New filter — were imaged with neutrons and apparent wall thickness profiles were calculated. For the exhaust-exposed filters, wall thicknesses greater than the thickness of the New filter were assumed to be due to the soot loading, and soot cake thicknesses were calculated.

While these filter samples were not specifically planned to make soot-loading measurements, the images obtained in this work show the promise of using neutron imaging to measure axial soot profiles in a DPF and study ash loading. These two measurements are key to improving the performance of the DPF and reducing its fuel penalty.

8.4 Appendix 4: Sample Model Calculations and Parameter Values

Model Parameters:

Pre-exponential factor, A = 3050

Activation Energy, E_a = 112.5 kJ/mol

Effectiveness factor, η = 0.2623 for ULSD, 0.977 for B100

Model Calculations

```
% Units:
% temperature in K, length in cm, time in s, mass in g

% Inputs:
Mco = input('Partuculate sample mass in grams:  ');
fuel = input('Biodiesel content of fuel:  ');
% selects fuel source by %biodiesel content 0=ULSD, 100=B100

% Variables:
%   X = mass carbon remaining = Mc/Mco
%   ext = extent of reaction = 1-X
%   Tg = gas temperature in K
%   tempstep = 5 (ramps at 5 degrees/min)
%   Pg = pressure (set as 1 atm)
%   Yo2 = mole fraction of oxygen
%   time = simulation time, s
%   tstep = time step, s (1 minute)
%   SA = surface area, cm^2, a function of extent of reaction and fuel

% setup initial conditions
Mc = Mco;     % initialize Mass Carbon to sample mass
time = 0;     % set time = 0
tstep = 60;   % set the time step
tend = 7200;  % Tramp from 323-923K at 5k/min takes 120 min
Tg = 323;     % initialize T (K)
tempstep = 5; % set the temperature ramp in degrees/time step
Tref = 298;   % standard reference T,(K)
Pt = 1;       % set the total pressure at 1 atm
YO2 = 0.1;    % set the mole fraction of O2 (in Ar)
fCO2 = 1;     % set the fraction of products that is CO2 (-)
```

```
% define flow terms
flowrate = 175; % set the volumetric flowrate (cm^3/min)
tubeD = 0.8;    % set the reactor tube diameter (cm)
tubeAx = pi*(tubeD/2)^2;  % cross-sectional area of the reactor tube
porosity = 0.45; % porosity of a packed bed of spheres
velocity = flowrate/tubeAx/60/porosity; % gas velocity (cm/s)
dp = 8e-2;  % diameter of ZrO2 particle (cm)

% constants
Ru = 8.314; % Ideal gas constant (J/mole/K)
prexp = 3050; % pre-exponential from plot of all data
Ea = 112.5;   % activation energy (kJ/mol)
eta_u =
eta_b =
MWC = 12;     % molecular weight of carbon (g/mol)
MWCO2 = 44;   % molecular weight of CO2 (g/mol)
MWO2 = 32;    % molecular weight of O2 (g/mol)
epsilon = 0.95; % emissivity for amorphous carbon (-)
sigma = 5.67e-12; % Stephan-Boltzman constant (W/cm^2-K^4)

% gas properties
C_t= Pt./(Ru.*Tg); % Total gas molar concentration (mol/cm^3)
DO2o= 0.178; % O2 diffusivity at 273 K (cm^2/s)
rhoAr = 0.5558/1e3; % density of Ar (g/cm^3)
CpAr = 520.33/1e3; % specific heat of Ar (J/g-K)
kAr = 0.03861/1e2; % thermal conductivity of Ar (W/cm-K)
muAr = 0.0005079; % viscosity of Ar (g/cm-s)
rhoO2 = 0.4452/1e3; % density of O2 (g/cm^3)
C_O2g = YO2*C_t; % gas phase concentration of O2 (mol/cm^3)
CpCO2 = 834/1e3; % specific heat of CO2 (J/g-K)

deltaHfCO2 = -393.52e3; % standard heat of formation of CO2 (J/mol)

% run the temperature programmed oxidation.
for Tg = 323 : 5 : 923;    % from 0-120 minutes in 60s intervals
   X = Mc/Mco;         % define X, the fraction sample remaining
   ext = 1-X;          % define ext, the extent of reaction
   DO2=DO2o*(Tg./273).^1.75; % O2 diffusivity at Tg (cm^2/s)

% calculate dimensionless numbers
   Re = dp*velocity*rhoAr/muAr; % Reynolds number (-)
   Pr = CpAr*muAr/kAr;          % Prandtl number (-)
   Pe = Re*Pr;                  % Peclet number (-)
   Sc = muAr/(rhoAr*DO2);       % Schmidt number (-)
   Sh = 2+1.8*Re^(1/2)*Sc^(1/3); % Sherwood number (-)
   Nu = 2+0.6*Re^(1/2)*Pr^(1/3); % Nusselt number (-)

% calculate surface area for reaction as a function of extent of
% reaction and sample mass (convert to cm^2) for both fuel types.
```

```
   SAu = Mc*(-505.4*(ext^2)+957.1*(ext)+123.4)*1e4;
% ULSD SA in cm^2
   SAb = Mc*(1352.5*(ext^3)-859.2*(ext^2)+1156*(ext)+157.0)*1e4;
% B100 SA in cm^2

% use fuel selector term to set fuel dependent variables
   if fuel == 0
      SA = SAu;   % fuel = 0 is for ULSD fuel
           eta = eta_u
   elseif fuel == 100
      SA = SAb;   % fuel = 100 for B100 fuel
           eta = eta_b
   else
      fprintf('blend not allowed');
   end

% calculate mass & energy balances & reaction rate
   h = Nu*kAr/dp; % calculate heat transfer coefficient (W/cm^2-K)
   km = Sh*DO2/(dp*YO2); % calculate mass transfer coefficient (cm/s)

% Reaction rate for fixed carbon+ volatile carbon
         Rxn = prexp*exp(Ea/(Ru*Tg))*SA + 1.2e-4*Tg^2+9.6e-3*Tg+1.92 ;
% area corrected reaction rate in mol/s
         Mc = Mc-Rxn/MWC; % update mass carbon remaining

% Mass Balance (using SSA)
         C_O2s = -(Rxn/(SA*km) - C_O2g); % surface concentration of O2 in mol/cm^3
         O2concRatio = C_O2s/C_O2g;      % ratio of surface to bulk concentration of O2 (-)

% Energy Balance (using SSA)
         C_CO2s = Rxn*fCO2;
% set surface concentration of CO2 equal to stoich products mol/s
         C_COs = Rxn*(1-fCO2);
% set surface concentration of CO equal to stoich products mol/s
         Qrxn = Rxn*(fCO2*(deltaHfCO2+(C_CO2s/MWCO2*CpCO2*(Tg-Tref))));
end
```

An attempt was made to model B20 particulate oxidation, calculating surface area by weighted average of parent fuels.

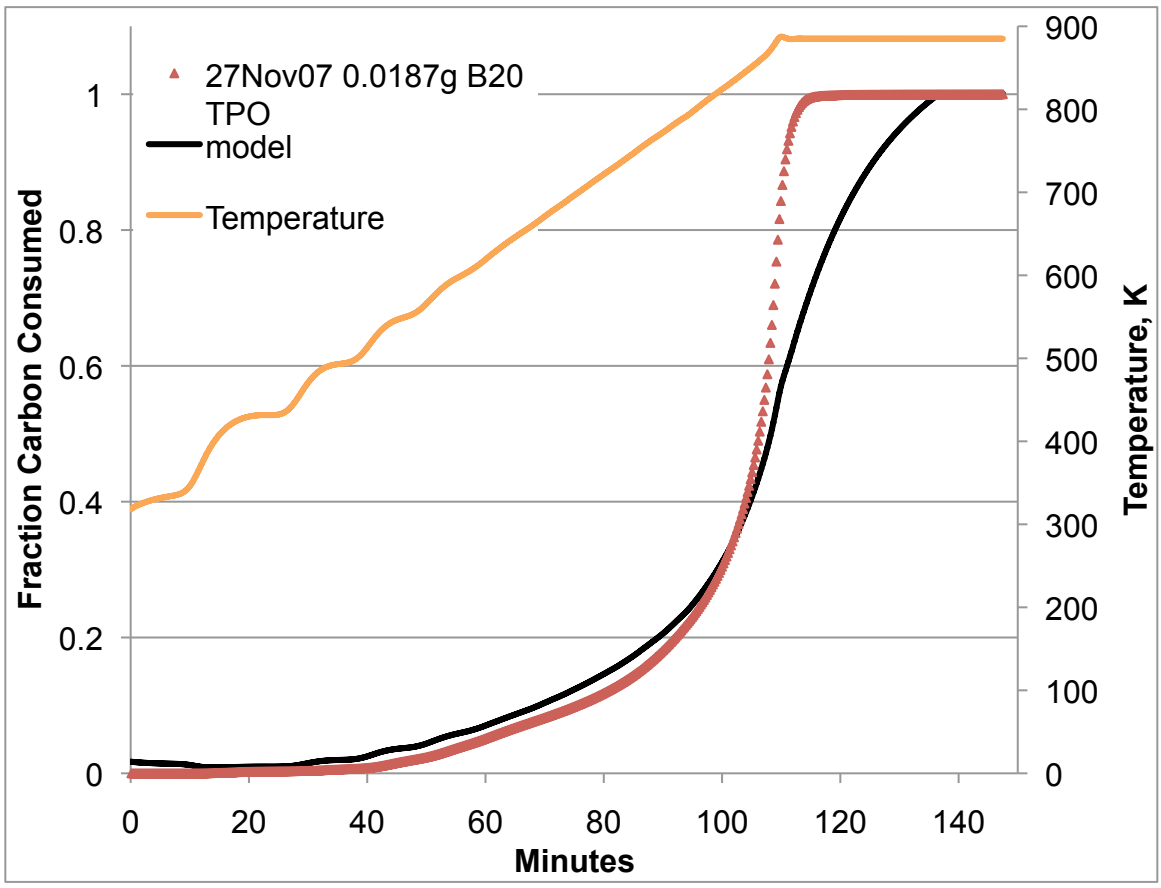

Figure A4-1 Model prediction for B20 TPO assuming that B20 soot has surface area equal to a weighted average of the parent fuels.

The model prediction captured the general trend, but under predicted the oxidation starting at approximately 40% burnout. Therefore, it is unlikely that the B20 surface area will be related to the surface area of the parent fuels in such a manner. Once the B20 surface area with burnout has been measured, the model should be able to predict the TPO.